

High-Resolution Images of Diffuse Neutral Clouds in the Milky Way. I. Observations, Imaging, and Basic Cloud Properties.

Y. Pidopryhora¹

School of Physical Sciences, University of Tasmania, Private Bag 37, Hobart, 7001,
Tasmania, Australia

`Yurii.Pidopryhora@utas.edu.au`

Felix J. Lockman²

National Radio Astronomy Observatory, Green Bank, WV 24944

`jlockman@nrao.edu`

J.M. Dickey

School of Physical Sciences, University of Tasmania, Private Bag 37, Hobart, 7001,
Tasmania, Australia

`John.Dickey@utas.edu.au`

M.P. Rupen^{2,3}

National Radio Astronomy Observatory, Socorro, NM 87801

`Michael.Rupen@nrc-cnrc.gc.ca`

Received _____; accepted _____

¹Current Address: Argelander-Institut für Astronomie, Auf dem Hügel 71, D-53121, Bonn, Germany

²The National Radio Astronomy Observatory is a facility of the National Science Foundation operated under a cooperative agreement by Associated Universities, Inc.

³Current Address: Dominion Radio Astronomy Observatory, National Research Council, PO Box 248, Penticton, BC, V2A 6J9 Canada

ABSTRACT

A set of diffuse interstellar clouds in the inner Galaxy within a few hundred pc of the Galactic plane has been observed at an angular resolution of $\approx 1''.0$ combining data from the NRAO Green Bank Telescope and the Very Large Array. At the distance of the clouds the linear resolution ranges from ~ 1.9 pc to ~ 2.8 pc. These clouds have been selected to be somewhat out of the Galactic plane and are thus not confused with unrelated emission, but in other respects they are a Galactic population. They are located near the tangent points in the inner Galaxy, and thus at a quantifiable distance: $2.3 \leq R \leq 6.0$ kpc from the Galactic Center, and $-1000 \leq z \leq +610$ pc from the Galactic plane. These are the first images of the diffuse neutral H I clouds that may constitute a considerable fraction of the ISM. Peak H I column densities range from $N_{\text{HI}} = 0.8 - 2.9 \times 10^{20} \text{ cm}^{-2}$. Cloud diameters vary between about 10 and 100 pc, and their H I mass spans the range from less than a hundred to a few thousands M_{\odot} . The clouds show no morphological consistency of any kind except that their shapes are highly irregular. One cloud may lie within the hot wind from the nucleus of the Galaxy, and some clouds show evidence of two distinct thermal phases as would be expected from equilibrium models of the interstellar medium.

Subject headings: ISM: structure – ISM: clouds – ISM: atoms – ISM: general – Galaxy: disk – radio lines: ISM

1. Introduction

The concept of a diffuse interstellar cloud is more than 50 years old, yet there are few observations that support the most basic aspects of the standard picture. The strongest evidence for discrete clouds is kinematic: there are usually distinct absorption lines at different velocities in spectra toward stars (e.g., Munch (1952); Hobbs (1978); Redfield & Linsky (2008)). But spectral features can be produced not only by spatial structures, i.e., clouds, but in a continuous turbulent medium as well (Lazarian & Pogosyan 2000). In contrast to the often well-defined clouds of molecular gas like the Infrared-dark Clouds (e.g., Rathborne et al. 2010), there is little support for the existence of discrete clouds in 21cm emission observations, which suggest instead that the atomic interstellar medium (ISM) consists of fragments of filaments and “blobby sheets”, many of which may be a consequence of turbulence (Kulkarni & Heiles 1987; Dickey & Lockman 1990; Miville-Deschênes et al. 2003; Heiles & Troland 2003; Kalberla & Kerp 2009). In most direction 21cm H I emission maps are highly confused, leading to considerable ambiguity in determining the morphology and boundaries of interstellar clouds, even assuming that they do exist. A mammoth study of Na I and Ca II absorption lines toward nearly 2000 stars within 800 pc of the Sun by Lallement et al. (2003) and Welsh et al. (2010) has revealed the three-dimensional structure of the local interstellar medium, “cell-like cavity structures” a fragmented “wall” of neutral gas, and what appears to be clouds “physically linked to the wall of denser gas”, but it is difficult to know how to generalize this result to the broader ISM.

The situation is quite different, however, in the lower halo of the inner Galaxy, where there is a population of discrete H I clouds whose velocities are consistent with circular rotation, but whose location several hundred pc from the plane separates them from unrelated emission (Lockman 2002, 2004)¹. Similar clouds can be seen at low Galactic

¹First detections of a few prominent representatives of this population date back to Prata

latitude when their random velocity is large enough to remove confusion (Stil et al. 2006); others are detected in the outer Galaxy (Strasser et al. 2007; Stanimirović et al. 2006; Dedes & Kalberla 2010). The clouds in the inner Galaxy are likely the product of H I supershells as their abundance and scale height are linked to the large-scale pattern of star formation in the disk (Ford et al. 2008, 2010).

While many aspects of these “disk-halo” clouds are poorly understood, they can be used as test particles sensitive to the physical conditions in their surroundings, and thus give information about interstellar processes not easily gotten from the highly blended spectra typical of most observations. The disk-halo clouds in the inner Galaxy are so abundant that a number of them lie near the terminal velocity in their direction, and thus near the tangent point, whose distance is determined from simple geometry. Their location, mass and size can be estimated with quantifiable errors.

There have been numerous theoretical studies of the expected properties of the diffuse ISM as a function of location in the Galaxy, distance from the Galactic plane, sources of heating, etc. Strong theoretical predictions have been made, especially about the existence of two thermal phases in pressure equilibrium (Field et al. 1969; Wolfire et al. 1995a,b; Koyama & Ostriker 2009). The disk-halo clouds offer the perfect laboratories for testing these predictions.

We selected a set of disk-halo clouds using observations with the Robert C. Byrd Green Bank Telescope (GBT) and measured them with the Very Large Array (VLA) in three different array configurations. The clouds were selected to cover a range of longitude and latitude and to be located near the tangent points of the inner Galaxy, and thus at a known

(1964), Simonson (1971), and Lockman (1984). A very detailed history and bibliography of both observational and theoretical early studies of interstellar clouds and H I halo can be found in Chapter 1 of Pidopryhora (2006).

distance.

This paper is the first in a series about these clouds. Here we discuss the observations and data reduction for the GBT and VLA D-array data only, taken at an angular resolution of $0'.9\text{--}1'.5$ providing a linear resolution of 1.9 to 2.8 pc. We concentrate on understanding all sources of uncertainty.

2. Selection of Targets

Targeted 21cm H I surveys of regions in the inner Galaxy made with the GBT provided a list of diffuse clouds that might be suitable for high-resolution imaging (Lockman 2002, 2004). From these we selected a set using the following criteria: 1) The clouds have LSR velocities at or beyond the terminal velocity in their direction ensuring that their distance could be determined (see §2.1); 2) the clouds cover a range of Galactic longitude and latitude ensuring that different environments were probed, though all are in the first quadrant of Galactic longitude; 3) the clouds are relatively isolated in position and velocity to minimize potential confusion; 4) their 21cm emission as observed with the GBT is bright enough to be detectable with the VLA in a few hours. An example of the GBT observations used to select the clouds is given in Figure 1. Table 1 gives the cloud designation, field centers, and the 21cm line peak brightness temperature, FWHM, and velocity as determined from the GBT observations.

2.1. Distance

The kinematics of the disk-halo cloud population studied here is dominated by the circular rotation of the Milky Way with a cloud-cloud velocity dispersion $\sigma_{cc} \approx 16 \text{ km s}^{-1}$ (Lockman 2002; Ford et al. 2008, 2010). Toward the inner Galaxy, the

maximum velocity permitted by Galactic rotation at $b = 0^\circ$ is called the terminal velocity, V_t , and arises from the tangent point where the distance from the Galactic center is $R_t = R_0 \sin \ell$. Here we use $R_0 = 8.5$ kpc, the IAU recommended value (Kerr & Lynden-Bell 1986). The terminal velocity can be measured from observations of species such as H I or CO or can be approximated with a rotation curve (e.g., Burton & Liszt (1993); Clemens (1985); McClure-Griffiths & Dickey (2007); Dickey (2013)). In the first quadrant of Galactic longitude $V_t > 0$ and an object with $V_{LSR} \gtrsim V_t$ must thus lie near the tangent point where its distance is known from geometry. In the current sample all clouds have velocities $V_{LSR} \gtrsim V_t$ so we calculate the tangent-point distance projected on the Galactic plane $d_p = R_0 \cos \ell$. A cloud's distance from the Galactic plane is then $z = d_p \tan b$ and the distance to the cloud center $d = (d_p^2 + z^2)^{\frac{1}{2}}$.

2.1.1. Distance Uncertainties

An estimate of the uncertainties in a cloud's distance can be derived from the change in distance that would correspond to a change in the cloud's V_{LSR} of σ_{cc} in that particular direction for an assumed rotation curve. As almost all of the clouds have $V_{LSR} > V_t$, in some cases by as much as $2\sigma_{cc}$, we conservatively estimate errors by the change in distance were the cloud to have a velocity $(V_t - \sigma_{cc})$ or $(V_{LSR} - \sigma_{cc})$, whichever produces the larger change in distance. Errors calculated this way using the rotation curves of Burton & Liszt (1993) and Dickey (2013) agree to within a few percent, and are given in Table 1. We note that the greater a cloud's velocity beyond V_t , the more likely that it lies near the tangent point (Ford et al. 2010). Thus for many of our clouds, especially G44.8 – 7.0 which lies nearly 30 km s^{-1} past V_t , our error estimates are probably overstated.

The final two columns of Table 1 give derived distances and errors as well as the distance of each cloud from the Galactic plane.

3. Observations and Basic Data Reduction

3.1. Green Bank Telescope Observations

The GBT was used to map H I emission around the disk-halo clouds to measure their overall properties, to determine whether they might be suitable for high-resolution imaging, and to provide the short spacing data for image reconstruction (see e. g., Stanimirović *et al.* (1999)). Maps were made over an area around each cloud of $1.5^\circ \times 1.5^\circ$ or $2^\circ \times 2^\circ$ depending on the extent of the cloud. Spectra were taken every 3.5 in Galactic longitude and latitude, somewhat finer than the Nyquist sampling interval for the GBT's 9.1 beam (FWHM). Observations were repeated several times over a period of a few months. In-band frequency switching gave a useable velocity coverage of 400 km s^{-1} around zero velocity (LSR) at a channel spacing of 0.16 km s^{-1} .

3.2. Very Large Array Observations

A sample of 20 H I disk-halo clouds was observed in 21 cm line emission spectroscopy with the Very Large Array (VLA) in D configuration during 2003 and 2004. The spectra had 256 frequency channels separated by 0.64 km s^{-1} in equivalent Doppler velocity centered on the peak velocity of each cloud (Pidopryhora *et al.* 2004; Lockman & Pidopryhora 2005; Pidopryhora 2006). Fifteen of the clouds were observed in single pointings, and 5 as mosaics. Two of these were also observed in C configuration with the identical spectroscopic setup (Pidopryhora *et al.* (2012)) and two more (G21.2 + 2.2 and G35.6 + 3.9) were observed in B configuration at both H I and OH frequencies in an attempt to detect absorption against bright background continuum sources. Here we present results on just the ten clouds observed only in D configuration with single pointings, deferring discussion of the others to a later paper. Parameters of the VLA observations are given in Table 2. An example of the *uv*-coverage for one of the clouds is given in Fig. 2.

3.3. Green Bank Telescope Data Reduction

The spectra were calibrated and corrected for stray radiation as described in Boothroyd et al. (2011), and a second-order polynomial was fit to emission-free regions of each spectrum to correct for residual instrumental effects. For each cloud the data were assembled into a cube on a $105''$ grid. There was occasional narrow-band interference that was stable in frequency, so spectra were interpolated over the affected channels. The final GBT data cubes had a brightness temperature noise ≈ 0.1 K in a 0.16 km s^{-1} channel.

Each GBT image cube was converted to the same coordinate system as the VLA, cropped to fit the exact VLA field size and interpolated to the matching grid and sequence of spectral channels with the Miriad (Sault et al. 1995) task REGRID. The GBT data were taken while the telescope was moving and thus have an effective resolution of $\approx 9'.6 \times 9'.1$, with the major axis along Galactic longitude, the scanning direction. In the VLA's equatorial coordinate system this resulted in slightly different beam position angles for each field. In order to smooth out gridding artifacts each GBT image was also convolved with a circular beam function of $200''$, approximately $1/3$ of the original beam size, so the final GBT angular resolution is approximately $10'$ FWHM.

3.4. Very Large Array Data Reduction

After calibration and study of preliminary dirty images of each VLA field, the continuum was subtracted in the uv domain using AIPS UVLIN task based on selected line-free channels. Naturally-weighted dirty images of continuum-free data were then cleaned channel by channel with AIPS SDCLN with no cleaning mask applied. The residual flux threshold was set to 0.7 mJy/beam for all clouds, corresponding to $0.2\text{--}0.3 \sigma$. In the final step the correction for the VLA primary beam was applied to the clean image cubes with the AIPS task PBCOR. The imaging synthesized beam size was different for each field

as described below; their values are given in Table 3.

4. Further Data Processing, Noise Levels and Errors

4.1. Combining the Interferometric and Single-Dish Data

For several reasons we have chosen to use Miriad’s IMMERGE to combine the interferometric and single-dish data: 1) it uses a well understood algorithm that is easy to control; 2) it runs quickly and is easily applied to large image cubes; 3) we have developed a calibration technique described below that ensures accuracy of the results.

Another approach was also tried for two clouds not of the set described in this paper (Pidopryhora *et al.* 2012): using a maximum entropy (MEM) algorithm (AIPS VTESS task) with the GBT image used as the default, but it was found to be less efficient. For a detailed review of all possible methods see Stanimirović (1999).

Miriad’s task IMMERGE uses a linear method sometimes known as ‘feathering’ to combine interferometric and single-dish data (Sault & Killeen 2008; Stanimirović 1999). Essentially this is just merging clean interferometric and single-dish images after Fourier-transforming them into the uv domain, the result covering the whole combined spatial frequency range. For this procedure to be meaningful the Fourier images of interferometric and single-dish data should match within the overlapping ranges of their common spatial frequencies. Due to the completely different natures of the two original datasets and thus unavoidable discrepancies, this has to be ensured by varying their common calibration scaling factor f_{cal} , which is the main control parameter of the IMMERGE task. In the case that the calibration of both data sets was done properly this factor should be close to unity, but its exact value has to be determined empirically in each particular case. If a compact source of 21cm emission were present in the field of view, both unresolved by the

VLA and unconfused with other emission by the GBT, determining f_{cal} would be as simple as dividing the interferometric flux density of this source by its single-dish flux density. Unfortunately, such sources are rare and not present in our data, so a more complex strategy of determining f_{cal} was used.

There is another important control parameter called ‘tapering’. If IMMERGE tapering is applied, the Fourier image of the interferometric data is smoothly continued into the low spatial-frequency region (Sault & Killeen 2008). This fixes possible edge effects in the Fourier transformation, but introduces an additional non-linear distortion of the data. As well as determining the best value of f_{cal} , it is necessary to decide if tapering should be applied.

4.2. Derivation of the Optimal f_{cal}

IMMERGE has a built-in method of matching the two datasets and deriving f_{cal} , provided that the overlapping range of spatial frequencies is defined. Figure 3 shows examples of application of this method. The interferometric image is convolved with the single-dish beam, then both images are Fourier-transformed and compared to each other within the overlapping spatial frequency range. The value of f_{cal} is selected by scaling the single-dish data until the slope of the line fit to the data is exactly 1. Based on several trials varying IMMERGE parameters with different samples taken from our data, we have determined that: 1) tapering distorts the data and makes a reasonable linear fit impossible; 2) due to a large scatter of the values the best linear fit usually does not characterize the data well and f_{cal} derived from it should be treated only as an estimate. Thus for our purposes we use IMMERGE without tapering and we determine the optimal f_{cal} by other methods.

It should be noted that describing the discrepancy between single-dish and

interferometric data with a single linear parameter is only an approximation of very complex behavior. One immediately notices that the optimal f_{cal} seems to be different for different channels (Stanimirović 1999). In particular, it is sensitive to the signal-to-noise ratio and spatial signal distribution of brightness in each channel. This is understandable as ideally f_{cal} should be determined from a point source unresolved by both telescopes. For a cloud comprised of diffuse gas that smoothly fills the field of view and is detectable by the single-dish but is completely invisible to the interferometer, the estimated f_{cal} approaches zero. In the cloud data we usually have some combination of these two extreme cases, and what seems to be the optimal f_{cal} may fluctuate significantly. But allowing it to vary with frequency would introduce an unknown non-linear distortion. Based on the general assumptions of this model, and as all clouds observed only with the VLA D-array present the same variety of interferometric data (similar beam sizes, noise levels, uv -coverage etc.), we sought a single value of f_{cal} that would work well not only for every channel of a particular cloud, but for all ten clouds.

One criterion for testing the goodness of a particular value of f_{cal} is that the spectrum of the merged cube averaged over an area somewhat larger than the GBT beam, but small enough not to be effected by the VLA primary beam pattern, should match the average taken over the same region in the single-dish data alone. We have found that averaging over an area $15'.3 \times 15'.3$ at the center of the field works well for all clouds observed with the VLA D-array. Requiring that the average spectrum over this area given by IMMERGE matches the single-dish mean profile is sufficient to derive an optimal $f_{\text{cal}} = 0.87$. In fact, this method may be preferable to any other since it directly preserves the single-dish flux.

Figure 4 shows the comparison of mean line profiles of the VLA, the GBT and the best IMMERGE combined images for all 10 targets using the single value of $f_{\text{cal}} = 0.87$, which was adopted for all subsequent work.

4.3. Testing the Accuracy of the Image Produced by IMMERGE

The average difference between the observed GBT and final IMMERGE line profiles can be calculated

$$\langle D \rangle = \frac{\sum_i (P_{\text{GBT}}(i) - P_{\text{IMMERGE}}(i))}{\sum_i P_{\text{GBT}}(i)} \quad (1)$$

where $P_{\text{GBT}}(i)$ and $P_{\text{IMMERGE}}(i)$ are the spectral values for individual channels and the summing is done over velocities of interest for each cloud. Figure 5 shows values of $\langle D \rangle$ for all 10 clouds. Taking into account the peculiarities of profiles that make their exact match impossible, e. g., the presence of large amounts of Galactic diffuse gas invisible to the interferometer as in clouds G33.4 – 8.0 and G44.8 – 7.0, these values set an upper limit to the error possibly introduced by IMMERGE in the process of merging the VLA and GBT data. For most of the clouds this error is only a few per cent, indicating that the resulting cubes are scaled accurately.

4.4. Converting to Galactic Coordinates

The final image cubes were regridded to Galactic coordinates as the last step of the data reduction. To ensure a smooth transformation the pixel size was decreased. The final cubes are 512×512 with a pixel size of $5''.7$ over the $49'$ diameter field. The synthesized beam sizes and resulting gains for the data cubes are given in Table 3.

4.5. The Noise Pattern

The detection threshold for the 21-cm line emission depends on the noise and its distribution across the map areas. Examining the noise distribution is also a useful test of the effects of the merger of the GBT and VLA data. We have measured the noise in the cubes at various stages of the analysis. An essential step of the VLA data reduction

is the primary beam attenuation correction, PBCOR, which involves scaling the data to correct for the attenuation from the primary beam response of the 25m dishes of the VLA. This correction must be done before using IMMERGE to determine f_{cal} as described in section 4.1. The correction for the primary beam response produces images whose noise is a strong function of radius from the pointing center. This is illustrated in Fig. 6, which shows the VLA+GBT column density map for G26.9 – 6.3. The high noise near the edges of the map shows the effect of the primary beam correction on the interferometer data, which persists after merger with the GBT data. (The GBT maps have nearly uniform sensitivity everywhere.) The noise distribution has a characteristic shape $\sigma(r)$ as a function of radius, r , from the field center. The noise at the map edge is so high that it dominates the brightness scale of the image.

To set a robust noise threshold for detection of the line, and to determine the errors in measured parameters based on the data, we need to understand the function $\sigma(r)$. The VLA primary beam gain factor is approximated in PBCOR by (Perley 2000):

$$G(X) = 1 + G_1 X^2 + G_2 X^4 + G_3 X^6, \quad (2)$$

$$X = fr,$$

where f is the frequency of observation in GHz and r is the angular radius in arcmin. The coefficients G_i are roughly constant for each VLA band; for our observations their values are:

$$\begin{aligned} G_1 &= -1.343 \times 10^{-3}, \\ G_2 &= +6.579 \times 10^{-7}, \\ G_3 &= -1.186 \times 10^{-10}. \end{aligned} \quad (3)$$

PBCOR divides the spectrum at each point by $G(fr)$ from eq. (2), thus amplifying both signal and noise, since $0 < G(fr) < 1$. The various clouds have slightly different values of the center frequency, f , depending on their radial velocities, and different values of σ_0 ,

which are almost entirely due to the noise in the VLA data, as explained in the next section. For setting detection thresholds and computing errors in the column density and mass at different points in each cloud, we use:

$$\sigma(r) = \sigma_0 \cdot [1 + G_1(fr)^2 + G_2(fr)^4 + G_3(fr)^6] \quad (4)$$

Figure 7 shows the measured values of $\sigma(r)$ using channels with no line emission as a function of distance from the center of the map shown in Fig. 6. The curve is the prediction of eq. 4, showing the effect of the primary beam correction applied to the VLA data, as it appears after merging with the GBT data. It is clear that noise from the VLA data completely dominates the noise in the final cubes, as the points in Fig. 7 are well described by the curve. For each cube we measure empirically the noise level at the field center, σ_0 , using off-line channels, and construct a noise function $\sigma(r)$ similar to that shown in Fig. 7. These are given in Table 4 in Kelvins and the equivalent error in N_{HI} for a 25 km s^{-1} wide velocity interval and the channel width of 0.64 km s^{-1} .

4.6. Noise Amplitude

Because of the angular resolution difference, noise from the GBT has little influence on the noise in the final cube, but rather appears as a systematic error in flux measurement over areas of a size comparable to the GBT beam. Rms noise values in the GBT cubes are $0.08 - 0.14 \text{ K}$, a factor 3-4 times smaller than the noise at the very center of any of the final H I maps. Thus the dominant noise in the final data comes from the VLA, and errors due to the GBT noise can be neglected.

We have processed the data in a number of non-trivial ways so it is important to check that the final noise level is reasonable, and is consistent with the noise in the VLA data at earlier reduction stages. Examination of the noise in line-free channels in the dirty continuum-subtracted cubes and in the clean cubes before PBCOR for four clouds is given

in Table 5. Comparing $\langle\sigma_{\text{clean}}\rangle$ for each cloud from Table 5 with σ_0 in Table 4 we conclude that despite a significant number of processing steps following the cleaning of the VLA image, the rms noise value remains virtually unchanged, except by the correction for the main beam gain of eq. (4).

Two conclusions can be drawn: 1) because rms noise values are good indicators of the finest scale of the image, the fact that they do not change much from the VLA to the final data cube shows that our procedure of recovering the short spacings from the GBT data has not distorted the small-scale structure of the interferometric data; 2) the values of σ_0 measured in § 4.5 and the noise pattern of eq. (4) are indeed valid indicators of the rms noise in the final data and can be used with confidence.

4.7. A Noise Threshold

Using eq. (4) we can establish a noise threshold for every pixel in a cube. If there is no emission $> 3\sigma(r)$ over the channel range of interest the spectrum is flagged and not used for making column density maps or other types of analysis. Figure 8 shows the same data as Figure 6, only with pixels blanked below the $3\sigma(r)$ level, leaving only emission detected significantly above the noise.

5. Results

5.1. Column Density Maps, Mass Profiles, Spectra

Fig. 9 shows in comparison both full and thresholded column density maps of G16.0 + 3.0 based separately on the GBT and VLA data, and final VLA+GBT results. Fig. 10 gives the corresponding mass profiles. Finally, Fig. 11 presents a summary of G16.0 + 3.0: thresholded VLA+GBT maps in relation to full GBT images, mass profile of

the VLA+GBT image, and spectra toward the N_{HI} peak of the clouds. Caption to the latter figure contains comments about the structure of the cloud.

Figures 12–38 present the same for the remaining 9 clouds.

Measured cloud properties are summarized in Table 6. The values of line brightness temperature, velocity and line width are derived from the Gaussian decomposition, sampled toward the position of the peak N_{HI} . Errors are 1σ from the Gaussian fit. Four of the clouds have spectral lines that require two Gaussians. The values of N_{HI} in col. 7 are integrals over the relevant velocity range (given in caption to each Figure) and are always close to the value from the sum of the Gaussian fits. We do not know the optical depth and so we cannot correct for self-absorption in the 21cm line, therefore the column densities and masses calculated in this paper are all lower limits.

The mass profiles were constructed in the following fashion. The mass was sampled over a set of annuli of varying radius increment but equal area, all centered at the main column density peak of the map. With equal areas, the mass in each annulus is proportional to the average N_{HI} with the same proportionality coefficient and thus the points can be plotted simultaneously with two sets of axes: distance-dependent mass M vs. linear radius and distance-independent $\langle N_{\text{HI}} \rangle$ vs. angular radius (see Fig. 10 and its counterparts, upper panels). The vertical error bars show the cumulative error due to noise², the horizontal ones show the average beam radius $r_{\text{beam}} \equiv \frac{1}{2}(B_{\text{maj}}B_{\text{min}})^{\frac{1}{2}}$, with B_{maj} and B_{min} for the VLA given in column 2 of Table 3. The GBT values are the same for all clouds: $10.2' \times 9.7'$, slightly increased compared to the original GBT beam due to pre-IMMERGE processing.

Since there is a significant freedom of choice for such annulus sets, we have selected a fixed maximum radius r_n of the sequence, the same for all clouds and equal to $0^\circ 319$, which

²Both the mass and the linear radius measurements are also subject to the distance uncertainty (see Table 7) not shown in these plots.

covers most of the VLA primary beam, with the exception of a small outer portion having the highest noise. Then we required the width of the largest annulus to be equal to r_{beam} , i.e. at the resolution of the map. Designating n the number of annuli and r_1 the smallest radius of the set, we arrive at the following equations:

$$r_n - r_{n-1} = r_{\text{beam}}, \quad (5)$$

$$r_i^2 - r_{i-1}^2 = r_1^2, \quad i \in [2, n], \quad (6)$$

$$r_i^2 - r_{i-1}^2 = \frac{r_{i-1}^2}{i-1}, \quad i \in [2, n], \quad (7)$$

$$r_i^2 = i r_1^2, \quad i \in [2, n]. \quad (8)$$

Solving eq. 5 together with eq. 8 at $i = n$ and $i = n - 1$ we get:

$$r_1 = [r_{\text{beam}}(2r_n - r_{\text{beam}})]^{\frac{1}{2}}. \quad (9)$$

Using eqns. 8 and 9 we have constructed the appropriate set of annuli for each cloud.

Comparing line parameters of the GBT-only observations of Table 1 with the high resolution GBT+VLA results in Table 6 we find identical mean velocities, with a difference of $0 \pm 2 \text{ km s}^{-1}$. As expected given the small angular structure revealed in the maps, the lines in the final maps are brighter by factors that range from 1.6 to 11 (for the very compact G16.0 + 3.0), with a median value around 4. These ratios are smaller than might occur: hydrogen clouds with sizes $< 1'$ should appear ≈ 100 times brighter to the VLA than the GBT, so it seems that the major structures in the clouds have been resolved in the current data. The line widths have a much smaller variation with the increased angular resolution. For lines that appear narrow to the GBT it is typical that they are even narrower in the combined data by around 20%, suggesting that the higher resolution observations are revealing colder or less turbulent material. But the broadest lines as measured with the GBT are sometimes even broader in the combined data, clouds G24.3 – 5.3 and G25.2 + 4.5 being examples.

5.2. Estimating Masses, Sizes and Densities of the Clouds

Table 7 gives the derived properties of the clouds for their adopted distances. Errors on derived parameters are dominated by the the distance uncertainties, whose estimates are discussed in §2.1.

In most cases the clouds do not display clear boundaries. In order to determine meaningful sizes and masses we have employed contours of constant N_{HI} . In each case a contour was chosen to encompass most of the visible cloud structures in the VLA+GBT maps (bottom left panels of Figures 9, 12 etc.). The resulting contours are shown in the left panels of Figures 39 – 42. The H I masses inside these contours for each cloud are listed in column 4. For comparison we have also drawn contours in the GBT maps at much lower N_{HI} values. The resulting contours are shown in the right panels of Figures 39 – 42 and the derived properties are listed in Table 8.

For each contour the major axis (the longest distance between two contour points) and the minor axis (the longest distance between contour points in the direction, perpendicular to the major axis) are determined. The length of these axes are listed as $D_{\text{maj}} \times D_{\text{min}}$ in column 5 of Table 7 and column 3 of Table 8.

The volume density in column 6 of Table 7 and column 4 of Table 8 is the total H I mass divided by the volume given by $\frac{4}{3}\pi r_e^3$ where the effective radius $r_e \equiv \frac{1}{2}(D_{\text{maj}}D_{\text{min}})^{\frac{1}{2}}$.

5.3. Cloud Cores

Table 9 gives estimates of the properties of the cloud cores, the denser regions of each cloud, determined by analyzing the H I emission at a higher value of N_{HI} around the column density peak of each cloud (column 2). The mass, size and number density of the enclosed area is given in cols. 3–5. The FWHM in Table 6 can be used to limit the kinetic

temperature — this value, T_{limit} is given in col. 6. Finally, multiplying values in columns 5 and 6 we can get a rough estimate of the core pressure in each cloud (column 7). For the clouds with two velocity components the total number density was split proportionally to the corresponding column densities.

5.4. Discussion

We have produced high angular-resolution 21cm H I maps of ten clouds that lie in the boundary between the disk and the halo in the inner Galaxy. This paper presents the data and the reduction methods necessary to insure accurate results. We defer a detailed discussion of the cloud properties to a separate publication, but some general comments can be made, for these clouds are unique samples of the neutral interstellar medium.

The disk-halo clouds, with masses of many hundreds of M_{\odot} and locations many hundreds of pc from the Galactic plane, are orders of magnitude denser than their surroundings.

The following rough estimates are made with the assumption of a spherical cloud of pure monoatomic hydrogen at constant number density n , its mass density $\rho = m_H n$. By the cloud “Size” we understand its diameter and take that T_{limit} determined based on the emission line FWHM, represents its true kinetic temperature T .

Under these conditions the sound-crossing time can be expressed as:

$$t_{\text{sound}} = \frac{\text{Size}}{c_s} \approx 2 \text{ Myr} \cdot \frac{\text{Size}}{\text{FWHM}}. \quad (10)$$

For clouds’ dense cores of sizes ~ 10 pc this is just a few Myr. But for whole clouds, with sizes ~ 100 pc, t_{sound} may reach 60 Myr.

On the other hand, the free-fall time of gravitational collapse:

$$t_{\text{ff}} = \sqrt{\frac{3\pi}{32G\rho}} \approx 50 \text{ Myr} \cdot n^{-\frac{1}{2}}. \quad (11)$$

For the highest cloud core density $\langle n \rangle \approx 10 \text{ cm}^{-3}$, $t_{\text{ff}} \approx 16 \text{ Myr}$, but for other cores it is 20–50 Myr and for whole clouds this time scale often exceeds 100 Myr. So in all cases $t_{\text{sound}} \ll t_{\text{ff}}$ and thus the clouds are not gravitationally bound.

It is instructive also to compare t_{sound} with the time t_z of vertical fall to the Galactic plane at cloud's location. Using a simple analytical expression of Wolfire et al. (1995b) for the z -component of the Galactic gravitational acceleration $g_z(R, z)$, one can see that for $|z| \lesssim 200 \text{ pc}$ the acceleration is close to linear: $g_z(R, z) \approx g'_z(R) \cdot z$. The values of g'_z range from $(10.8 \text{ Myr})^{-2}$ at $R = 8.5 \text{ kpc}$ to $(5.4 \text{ Myr})^{-2}$ at $R = 2.5 \text{ kpc}$. Since motion with such acceleration is harmonically periodic, the free-fall time is just $\frac{\pi}{2} g'_z{}^{-1/2}$. For higher $|z|$ where $g_z(R, z)$ flattens, these values can be used as lower limits:

$$t_z \gtrsim \frac{\pi}{2} (g'_z(R))^{-\frac{1}{2}}, \quad (12)$$

equal to 8 – 17 Myr for $2.5 \text{ kpc} < R < 8.5 \text{ kpc}$. In Pidopryhora (2006) a more precise ballistic calculation was done for $2 \text{ kpc} < R < 5.3 \text{ kpc}$ and a much greater distance from the plane $z \approx 3.4 \text{ kpc}$ using Walter Dehnen's *GalPot* package (Dehnen & Binney 1998), obtaining $t_z \approx 30 \text{ Myr}$, which can be used as an upper limit for all the disk-halo clouds.

For the cloud cores the condition $t_{\text{sound}} \ll t_z$ is true, so the clouds have time to respond to local physical conditions. The clouds must have come to internal pressure equilibrium, although the pressure may have contributions from turbulence on a range of scales, and possibly magnetic field and cosmic ray pressures as well. But since $t_{\text{sound}} \gtrsim t_z$ for the larger cloud structure, the overall density distribution of the cloud does not have time to dissipate in the low pressure of the halo over the time it takes the cloud to rise or to fall back to the disk.

Similarly one can estimate the clouds' Jeans masses as

$$M_J = \left(\frac{5k_B T}{Gm_H} \right)^{\frac{3}{2}} \left(\frac{3}{4\pi\rho} \right)^{\frac{1}{2}} \approx 9400 M_{\odot} \cdot \text{FWHM}^3 n^{-\frac{1}{2}}, \quad (13)$$

which is two to three orders of magnitude larger than their observed gas masses.

All this implies that the clouds are dynamic entities whose properties must reflect their history as well as conditions at their current locations (e.g., Koyama & Ostriker 2009; Saury et al. 2014). While the appearance of many of the disk-halo clouds suggests that they are interacting with their local environment producing the steep gradients in N_{HI} or asymmetric shapes, we find little correlation between location in the Galaxy and fundamental cloud properties, with one clear exception, G16.0 + 3.0 discussed below.

In theories of the interstellar medium the local pressure is often the controlling factor in the structure of neutral clouds, and over a wide range of conditions in the Galaxy it is expected that neutral clouds could consist of two phases, one warm and one cold (Field et al. 1969; McKee & Ostriker 1977; Wolfire et al. 1995a; Jenkins 2012). Four of the clouds studied here have line profiles indicating the presence of two components with different temperatures at the location of their peak N_{HI} . It is unlikely that this results from confusion of unrelated material as all two-component clouds are located at $|z| \geq 590$ pc from the Galactic plane. The components typically have similar but not identical values of V_{LSR} . The narrower line component contains between 30% and 50% of the total N_{HI} , about the mass fraction expected from some simulations (Saury et al. 2014). However, clouds may have two phases not easily separable in their emission profiles as the cold gas may have large velocity fluctuations that blend it with the warmer emission (Vázquez-Semadeni 2012; Saury et al. 2014).

Cloud G16.0 + 3.0 is particularly interesting, as it may lie within the area around the Galactic nucleus excavated by a hot wind: the “Fermi Bubble” (e.g., Bland-Hawthorn & Cohen 2003; Su et al. 2010). The boundaries of the region effected by the wind are not well-defined, especially at low latitudes, but the G16.0 + 3.0 cloud has such distinctive properties as to suggest that its environment is different from that of the other clouds. Within the hot wind the pressure is many times larger than the typical ISM (Bland-Hawthorn & Cohen 2003; Carretti et al. 2013); this is expected to force clouds into a purely cold phase (Field et

al. 1969; Gatto et al. 2015). The properties of G16.0 + 3.0, with its high density, narrow line width, and compact structure, are consistent with this interpretation. Moreover, G16.0 + 3.0 is notably smaller than the other clouds, but its size is similar to that of the H I clouds found to be entrained in the nuclear wind (McClure-Griffiths et al. 2013). In contrast, the nearby cloud G17.5 + 2.2 is nearly indistinguishable from the other clouds studied here. It might be as close as 135 pc to G16.0 + 3.0, but is more likely at least 1 kpc away given the uncertainties in our assignment of distances. Neither cloud shows kinematic anomalies suggesting that they have been accelerated by the nuclear wind (McClure-Griffiths et al. 2013).

We can also compare the properties of our disk-halo clouds with the disk clouds of Stil et al. (2006) observed at similar resolution, but all at $z \approx 0$. Only one of their clouds, 59.67 – 0.39 + 60 has an analogous morphology and size, with a few times larger mass and average density compared to the clouds of our survey. The properties of all their other clouds are close to our cloud cores, only in some cases displaying a few times larger average density.

These disk-halo H I structures allow us to study unconfused interstellar clouds in a variety of locations; this may lead to a better understanding of physical conditions that have hitherto been manifest only in ensemble averages. When the GASKAP survey (Dickey et al. 2013) is done, and even more when the full SKA is ready, studies like this one will reveal many more such clouds, and the techniques developed here will be useful for understanding their properties.

This research was supported in part by the Australian Research Council through grant DP110104101 to the University of Tasmania. YP has started working on this research project while he held a predoctoral fellowship at the NRAO and then did a part of it while being employed at the Joint Institute for VLBI in Europe (Dwingeloo, the Netherlands).

We thank the anonymous referee for comments and suggestions that helped to improve this paper.

Facilities: GBT, VLA

Table 1. Cloud Properties from GBT Observations

Name	T_b^1	V_{LSR}^1	FWHM	Distance	z
	(K)	(km s $^{-1}$)	(km s $^{-1}$)	(kpc)	(pc)
(1)	(2)	(3)	(4)	(5)	(6)
G16.0 + 3.0	1.1	+143	5.4	8.2 ± 1.0	$+430 \pm 50$
G17.5 + 2.2	1.6	+139	16.2	8.1 ± 1.1	$+310 \pm 40$
G19.5 − 3.6	3.5	+121	13.1	8.0 ± 1.6	-500 ± 100
G22.8 + 4.3	3.1	+137	7.8	7.9 ± 1.4	$+590 \pm 100$
G24.3 − 5.3	1.3	+124	13.5	7.8 ± 1.5	-720 ± 140
G24.7 − 5.7	1.8	+127	8.9	7.8 ± 1.5	-770 ± 150
G25.2 + 4.5	2.6	+147	10.4	7.7 ± 1.6	$+610 \pm 130$
G26.9 − 6.3	3.4	+123	8.8	7.6 ± 1.7	-840 ± 190
G33.4 − 8.0	1.1	+102	5.5	7.2 ± 2.0	-1000 ± 280
G44.8 − 7.0	3.3	+94	9.0	6.1 ± 2.5	-740 ± 300

Table 2. Parameters of the VLA Observations

Cloud	Pointing Coordinates (J2000)	Integration Time, minutes	Central Velocity, km s ⁻¹	Calibrators
G16.0 + 3.0	18 ^h 08 ^m 42.850 ^s -13°35'17"	131	+140	1833-210, 1331+305
G17.5 + 2.2	18 ^h 14 ^m 46.672 ^s -12°39'31"	105	+135	1833-210, 1331+305
G19.5 - 3.6	18 ^h 39 ^m 46.681 ^s -13°32'41"	90	+120	1833-210, 1331+305
G22.8 + 4.3	18 ^h 17 ^m 20.803 ^s -06°59'31"	143	+120	1812-068, 1331+305
G24.3 - 5.3	18 ^h 54 ^m 52.557 ^s -10°03'07"	222	+125	1833-210, 1331+305
G24.7 - 5.7	18 ^h 57 ^m 05.347 ^s -09°52'41"	64	+125	1833-210, 1331+305
G25.2 + 4.5	18 ^h 21 ^m 24.210 ^s -04°49'06"	172	+145	1812-068, 1833-210, 1331+305
G26.9 - 6.3	19 ^h 03 ^m 07.240 ^s -08°17'17"	215	+122	1833-210, 0137+331, 1331+305
G33.4 - 8.0	19 ^h 20 ^m 52.118 ^s -03°16'43"	102	+102	1939-100, 1331+305
G44.8 - 7.0	19 ^h 38 ^m 25.318 ^s +07°17'16"	105	+94	1941-154, 1331+305

Table 3. Synthesized beam sizes

Cloud	FWHM ($''$)	Gain (K/Jy)	\langle FWHM \rangle (pc)
G16.0 + 3.0	89.5×52.6	129	2.7
G17.5 + 2.2	85.7×56.5	126	2.7
G19.5 − 3.6	84.6×58.0	124	2.7
G22.8 + 4.3	72.9×56.1	149	2.4
G24.3 − 5.3	75.6×56.2	143	2.5
G24.7 − 5.7	77.0×59.8	132	2.6
G25.2 + 4.5	71.2×55.6	154	2.4
G26.9 − 6.3	73.5×57.3	145	2.4
G33.4 − 8.0	73.0×58.3	143	2.3
G44.8 − 7.0	68.5×57.7	154	1.9

Table 4. Noise levels at the field center

Cloud	σ_0 (K)	$\sigma(N_{HI})^1$ (10^{18} cm^{-2})
G16.0 + 3.0	0.45	3.2
G17.5 + 2.2	0.58	4.1
G19.5 − 3.6	0.51	3.7
G22.8 + 4.3	0.55	3.9
G24.3 − 5.3	0.46	3.3
G24.7 − 5.7	0.48	3.5
G25.2 + 4.5	0.42	3.0
G26.9 − 6.3	0.42	3.0
G33.4 − 8.0	0.43	3.1
G44.8 − 7.0	0.41	3.0

¹In assumption of 40 channels of the total width of 25 km s^{-1} .

Table 5. Propagation of Noise Through the Imaging

Cloud	$\langle\sigma_{\text{dirty}}\rangle$ (mJy/beam)	$\langle\sigma_{\text{dirty}}\rangle$ (K)	$\langle\sigma_{\text{clean}}\rangle$ (mJy/beam)	$\langle\sigma_{\text{clean}}\rangle$ (K)
G16.0 + 3.0	3.3	0.42	3.6	0.46
G26.9 − 6.3	2.7	0.39	2.9	0.42
G33.4 − 8.0	2.8	0.40	3.0	0.42
G44.8 − 7.0	2.6	0.41	2.7	0.42

Table 6. Measured Cloud Properties

Cloud	R	z	T_b	V_{LSR}	FWHM	Peak N_{HI}
	(kpc)	(pc)	(K)	(km s $^{-1}$)	(km s $^{-1}$)	(10 20 cm $^{-2}$)
(1)	(2)	(3)	(4)	(5)	(6)	(7)
G16.0 + 3.0	2.34	+430	12.3 ± 0.3	143.6 ± 0.1	4.7 ± 0.1	1.2
G17.5 + 2.2	2.56	+310	6.2 ± 0.3	138.3 ± 0.4	18.2 ± 1.0	2.1
G19.5 – 3.6	2.84	–500	14.6 ± 0.4	118.8 ± 0.1	9.9 ± 0.3	2.9
G22.8 + 4.3	3.29	+590	4.9 ± 0.4	135.2 ± 0.2	5.8 ± 0.6	1.7
			3.2 ± 0.4	131.7 ± 0.8	24.3 ± 2.2	
G24.3 – 5.3	3.50	–720	2.7 ± 0.1	125.6 ± 0.5	17.4 ± 1.1	0.9
G24.7 – 5.7	3.55	–770	7.8 ± 0.3	128.0 ± 0.1	5.5 ± 0.2	1.0
G25.2 + 4.5	3.62	+610	6.3 ± 0.2	144.5 ± 0.2	13.4 ± 0.5	1.6
G26.9 – 6.3	3.85	–840	13.0 ± 0.4	120.3 ± 0.1	3.0 ± 0.1	2.2
			5.2 ± 0.3	124.1 ± 0.3	14.5 ± 0.6	
G33.4 – 8.0	4.68	–1000	3.5 ± 0.3	101.9 ± 0.2	4.3 ± 0.5	0.8
			1.7 ± 0.3	101.0 ± 0.8	20.2 ± 3.1	
G44.8 – 7.0	5.99	–740	6.8 ± 0.4	93.4 ± 0.1	6.1 ± 0.4	1.7
			2.3 ± 0.3	99.4 ± 1.1	18.7 ± 1.5	

Table 7. Derived Cloud Properties

Cloud	R	z	M_{HI}^1	Size ^{1 2}	$\langle n \rangle$
	(kpc)	(pc)	(M_\odot)	(pc)	(cm^{-3})
(1)	(2)	(3)	(4)	(5)	(6)
G16.0 + 3.0	2.34 ± 0.20	$+430 \pm 50$	45_{-10}^{+12}	16×10 (0.12)	1.73 ± 0.20
G17.5 + 2.2	2.56 ± 0.23	$+310 \pm 40$	440_{-110}^{+130}	43×23 (0.14)	1.10 ± 0.15
G19.5 − 3.6	2.84 ± 0.42	-500 ± 100	830_{-300}^{+370}	67×28 (0.20)	0.80 ± 0.16
G22.8 + 4.3	3.29 ± 0.29	$+590 \pm 100$	550_{-180}^{+210}	50×35 (0.18)	0.59 ± 0.11
G24.3 − 5.3	3.50 ± 0.31	-720 ± 140	300_{-100}^{+130}	59×29 (0.19)	0.33 ± 0.06
G24.7 − 5.7	3.55 ± 0.30	-770 ± 150	290_{-100}^{+120}	60×38 (0.19)	0.21 ± 0.04
G25.2 + 4.5	3.62 ± 0.34	$+610 \pm 130$	690_{-260}^{+320}	58×48 (0.21)	0.37 ± 0.08
G26.9 − 6.3	3.85 ± 0.36	-840 ± 190	600_{-240}^{+300}	66×32 (0.22)	0.48 ± 0.11
G33.4 − 8.0	4.68 ± 0.41	-1000 ± 280	160_{-80}^{+100}	38×28 (0.28)	0.36 ± 0.10
G44.8 − 7.0	5.99 ± 0.50	-740 ± 300	840_{-550}^{+830}	62×41 (0.41)	0.51 ± 0.21

¹Clouds' sizes and masses determined based on contours shown in the left panels of Figs. 39–42.

²Fractional uncertainties in both dimensions are identical and are given by the value in parentheses.

Table 8. Wide-Field Cloud Properties Based on GBT Data

Cloud	M_{HI}^1	Size ^{1 2}	$\langle n \rangle$
	(M_{\odot})	(pc)	(cm^{-3})
(1)	(2)	(3)	(4)
G16.0 + 3.0	83^{+21}_{-19}	47×43 (0.12)	0.07 ± 0.01
G17.5 + 2.2	750^{+220}_{-190}	57×39 (0.14)	0.56 ± 0.08
G19.5 − 3.6	1920^{+840}_{-690}	100×71 (0.20)	0.25 ± 0.05
G22.8 + 4.3	1370^{+530}_{-440}	103×70 (0.18)	0.17 ± 0.03
G24 − 5 ³	1150^{+480}_{-400}	158×59 (0.19)	0.10 ± 0.02
G25.2 + 4.5	1690^{+780}_{-630}	119×75 (0.21)	0.16 ± 0.03
G26.9 − 6.3	1570^{+780}_{-620}	151×85 (0.22)	0.08 ± 0.02
G33.4 − 8.0	540^{+340}_{-260}	115×58 (0.28)	0.08 ± 0.02
G44.8 − 7.0	2560^{+2530}_{-1670}	122×85 (0.41)	0.19 ± 0.08

¹Clouds' sizes and masses determined based on contours shown in the right panels of Figs. 39–42.

²Fractional uncertainties in both dimensions are identical and are given by the value in parentheses.

³Total for the group of three clouds, containing G24.3 − 5.3 and G24.7 − 5.7.

Table 9. Cloud Core Properties

Cloud	contour N_{HI} (10^{20} cm^{-2})	M_{HI} (M_{\odot})	Size ¹ (pc)	$\langle n_c \rangle$ (cm^{-3})	T_{limit} (K)	$T_{\text{limit}} \cdot \langle n_c \rangle$ (10^3 K cm^{-3})
(1)	(2)	(3)	(4)	(5)	(6)	(7)
G16.0 + 3.0	0.2	45^{+12}_{-10}	16×10 (0.12)	1.7 ± 0.2	480 ± 20	0.8 ± 0.14
G17.5 + 2.2	1.5	66^{+19}_{-17}	14×6 (0.14)	6.7 ± 0.9	7200 ± 790	48 ± 12
G19.5 – 3.6	2.2	60^{+26}_{-22}	10×6 (0.20)	10.0 ± 2.0	2100 ± 130	21 ± 6
G22.8 + 4.3	1.2	57^{+22}_{-18}	11×9 (0.18)	4.5 ± 0.8		
				1.2 ± 0.2	730 ± 150	0.9 ± 0.3
				3.3 ± 0.6	13000 ± 2300	42 ± 15
G23.1 + 4.3 ²	0.9	38^{+15}_{-12}	10×6 (0.18)	6.4 ± 1.2		
				2.2 ± 0.4	590 ± 200	1.3 ± 0.7
				4.2 ± 0.8	7300 ± 2200	30 ± 14
G24.3 – 5.3	0.6	45^{+19}_{-16}	15×14 (0.19)	1.2 ± 0.2	6600 ± 830	7.6 ± 2.4
G24.7 – 5.7	0.5	53^{+22}_{-18}	21×7 (0.19)	2.3 ± 0.4	660 ± 50	1.5 ± 0.4
G25.2 + 4.5	1.2	57^{+26}_{-21}	15×7 (0.21)	4.1 ± 0.9	3900 ± 290	16 ± 5
G26.9 – 6.3	1.3	54^{+27}_{-21}	10×7 (0.22)	7.2 ± 1.6		
				2.5 ± 0.5	200 ± 13	0.5 ± 0.14
				4.7 ± 1.1	4600 ± 380	22 ± 7
G33.4 – 8.0	0.5	47^{+30}_{-22}	24×8 (0.28)	1.4 ± 0.4		
				0.4 ± 0.1	400 ± 90	0.2 ± 0.1
				1.0 ± 0.3	8900 ± 2700	9 ± 5

Table 9—Continued

Cloud	contour N_{HI} (10^{20} cm^{-2})	M_{HI} (M_{\odot})	Size ¹ (pc)	$\langle n_c \rangle$ (cm^{-3})	T_{limit} (K)	$T_{\text{limit}} \cdot \langle n_c \rangle$ (10^3 K cm^{-3})
(1)	(2)	(3)	(4)	(5)	(6)	(7)
G44.8 – 7.0	1.2	54^{+53}_{-35}	15×7 (0.41)	3.9 ± 1.6		
				1.9 ± 0.8	810 ± 110	1.6 ± 0.8
				2.0 ± 0.8	7600 ± 1200	15 ± 9

¹Fractional uncertainties in both dimensions are identical and are given by the value in parentheses.

²A small separate cloud at the high-longitude side of the G22.8 + 4.3 field. First velocity component: $T_b = 6.4 \pm 0.9 \text{ K}$, $V_{\text{LSR}} = 129.3 \pm 0.3 \text{ km s}^{-1}$, $\text{FWHM} = 5.2 \pm 0.9$; second velocity component: $T_b = 3.4 \pm 0.6 \text{ K}$, $V_{\text{LSR}} = 135.1 \pm 1.7 \text{ km s}^{-1}$, $\text{FWHM} = 18.3 \pm 2.7$.

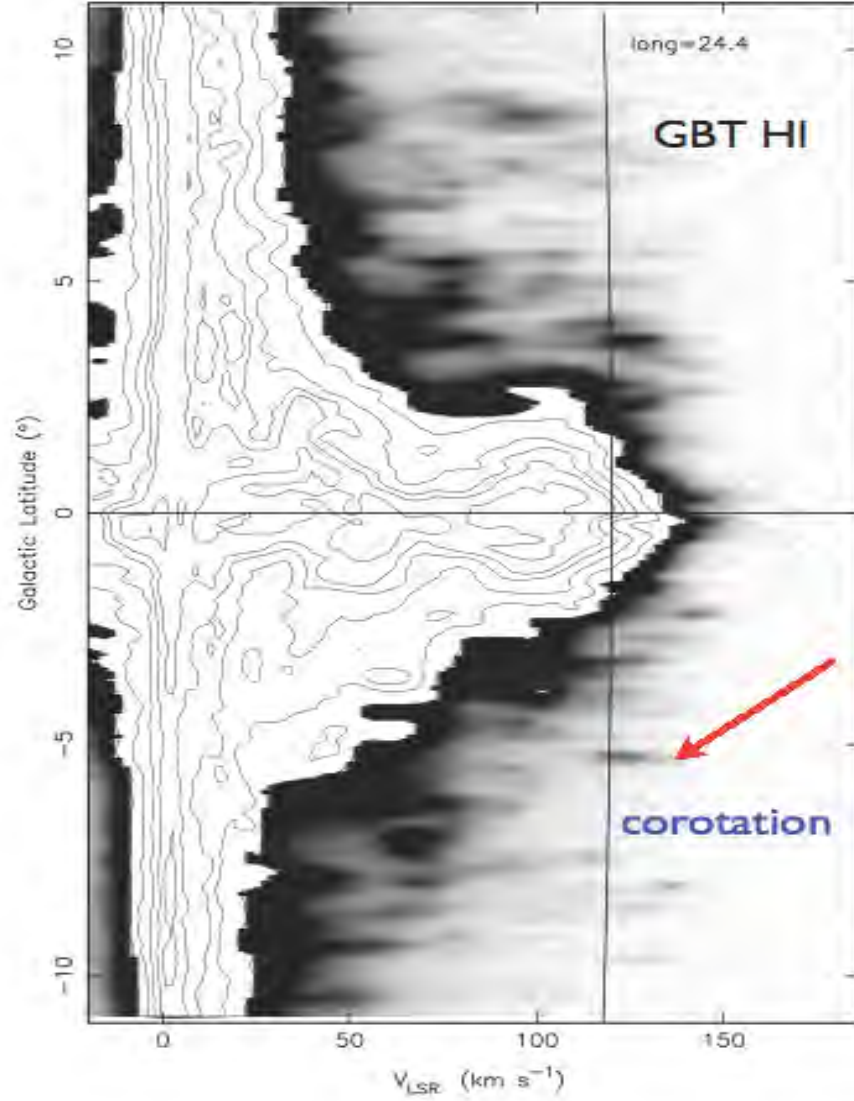


Fig. 1.— Velocity-latitude image of H I emission from GBT observations after Lockman & Pidopryhora (2005). The cloud at 24.3 – 5.3 is marked with an arrow. The expected maximum V_{LSR} from Galactic rotation (Clemens 1985) is marked by the slightly curved vertical line. The location of G24.3 – 5.3 slightly beyond the maximum velocity indicates that it must lie near the tangent point in its direction. Note that it is separated in position and velocity from other H I emission and is thus relatively unconfused.

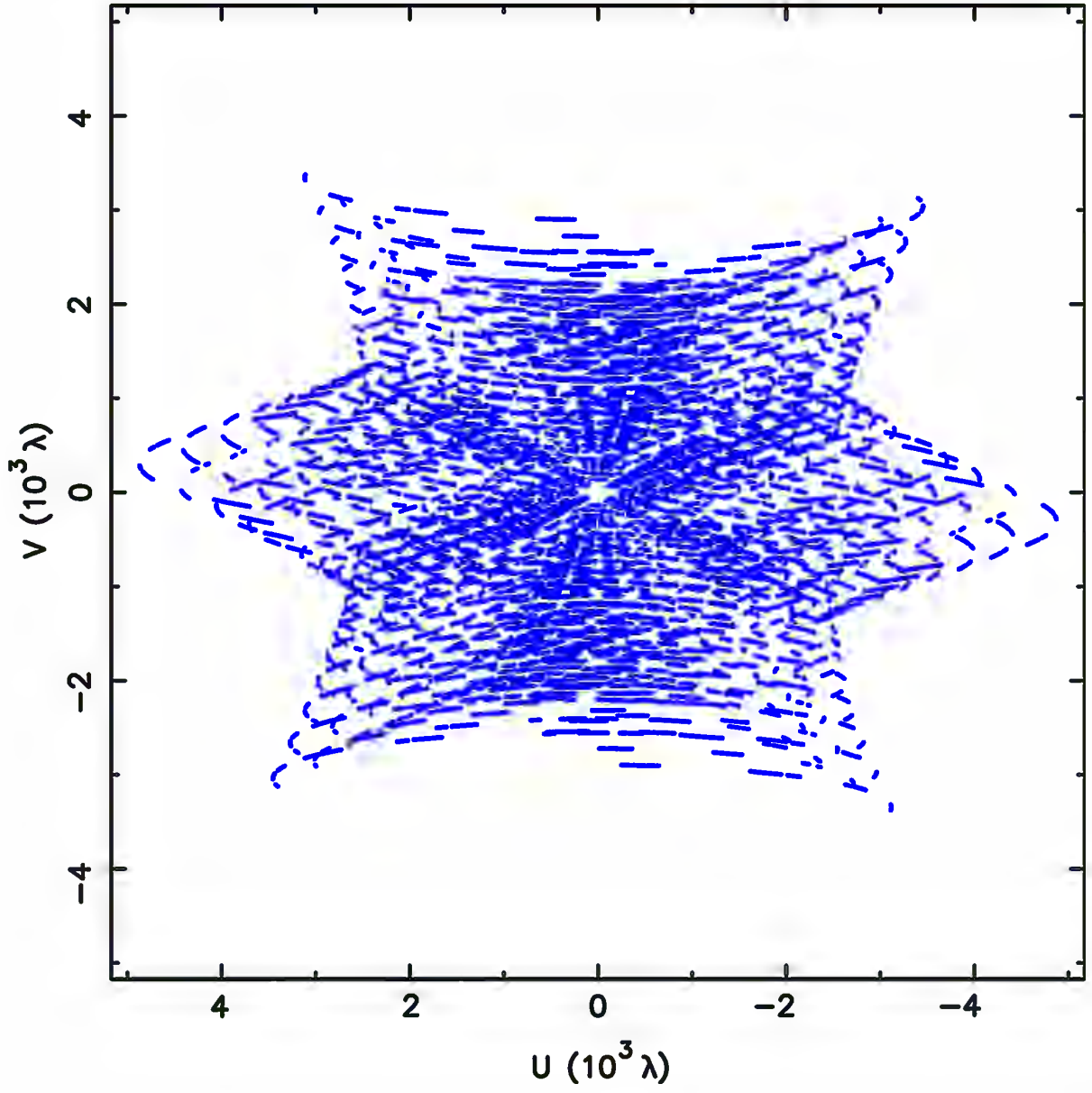


Fig. 2.— uv -coverage of the VLA observations of one of the clouds, G26.9–6.3. Two epochs of June 29 and July 24 2004 combined, total integration time 215 min., source declination $\delta \approx -8^\circ$.

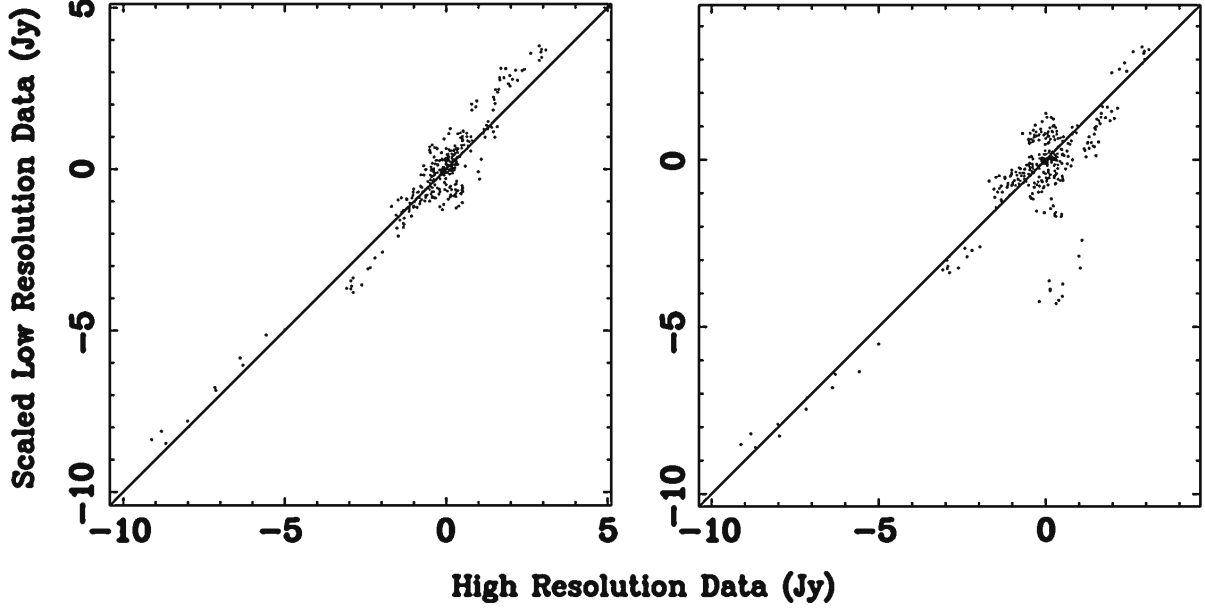


Fig. 3.— Linear fit to pixel-by-pixel comparison of single-dish and interferometer data of cloud G17.5 + 2.2 generated by Miriad’s task IMMERGE in the process of solving for the optimal f_{cal} value. The left panel is without tapering, the right panel uses tapering. Data are used from the position of the brightest line averaged over a region $15'.3 \times 15'.3$. The overlapping frequency range in the Fourier domain was set to be 20 – 50 meters $\approx 95 - 240\lambda$. The values for the high resolution data were calculated from the interferometric data convolved with the single-dish beam to compensate for the difference in resolution. The values for the low resolution, single-dish data were scaled by f_{cal} . The value of f_{cal} determined from the left panel is 0.68, from the right is 0.62. In the tapered case it is clear that the assumption of linearity fails, while in the non-tapered case the bulk of the points close to zero favor a somewhat different slope.

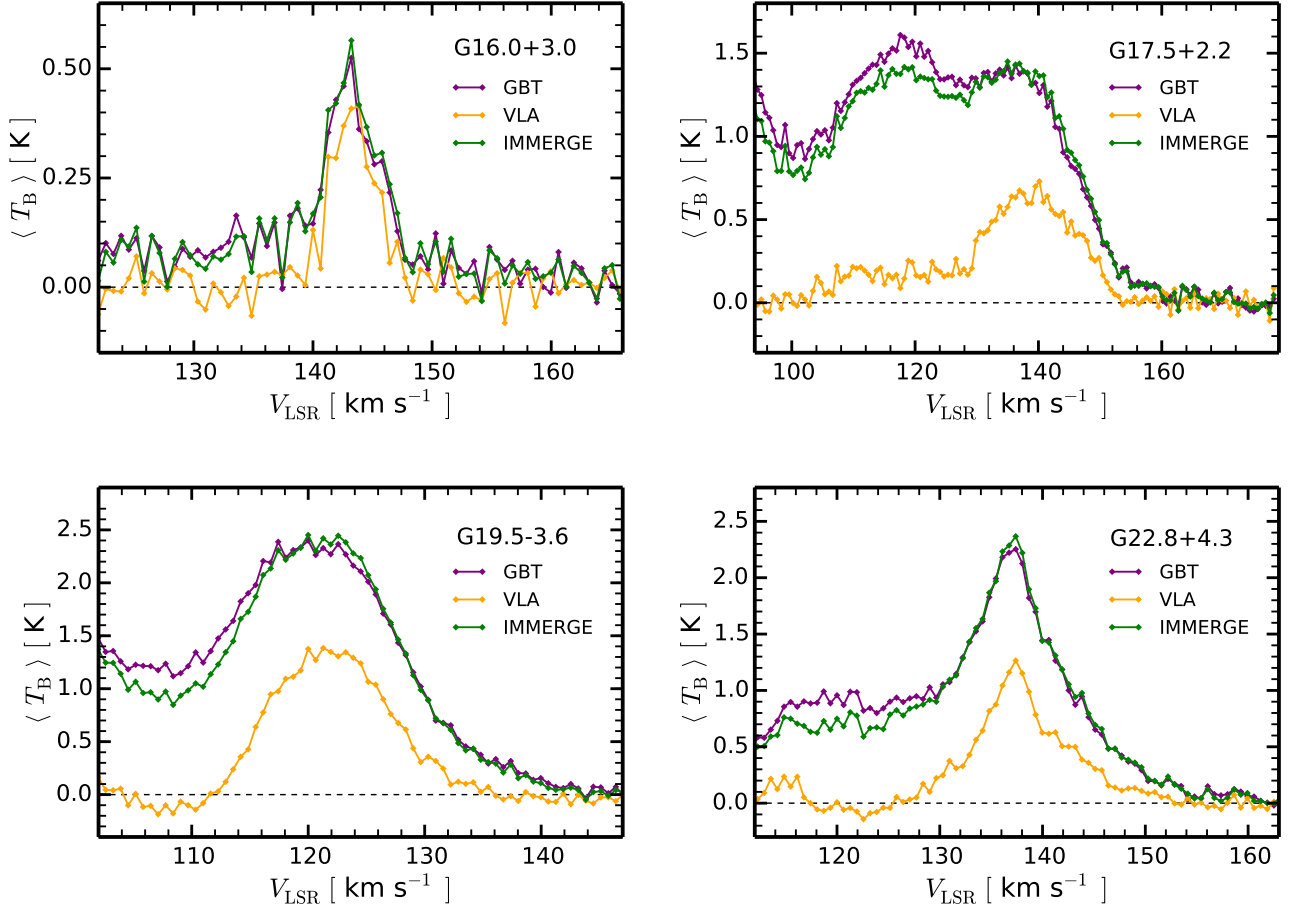


Fig. 4.— Page 1 of 3 — Mean line profiles in brightness temperature T_b , at the center of each field for clean VLA data (orange), GBT data (purple) and results of running IMMERGE on these two images with $f_{\text{cal}}=0.87$ and no tapering (green). This sum is calculated over all pixels in an 80 by 80 pixel box. The comparison shows how well the total single-dish flux is recovered by IMMERGE.

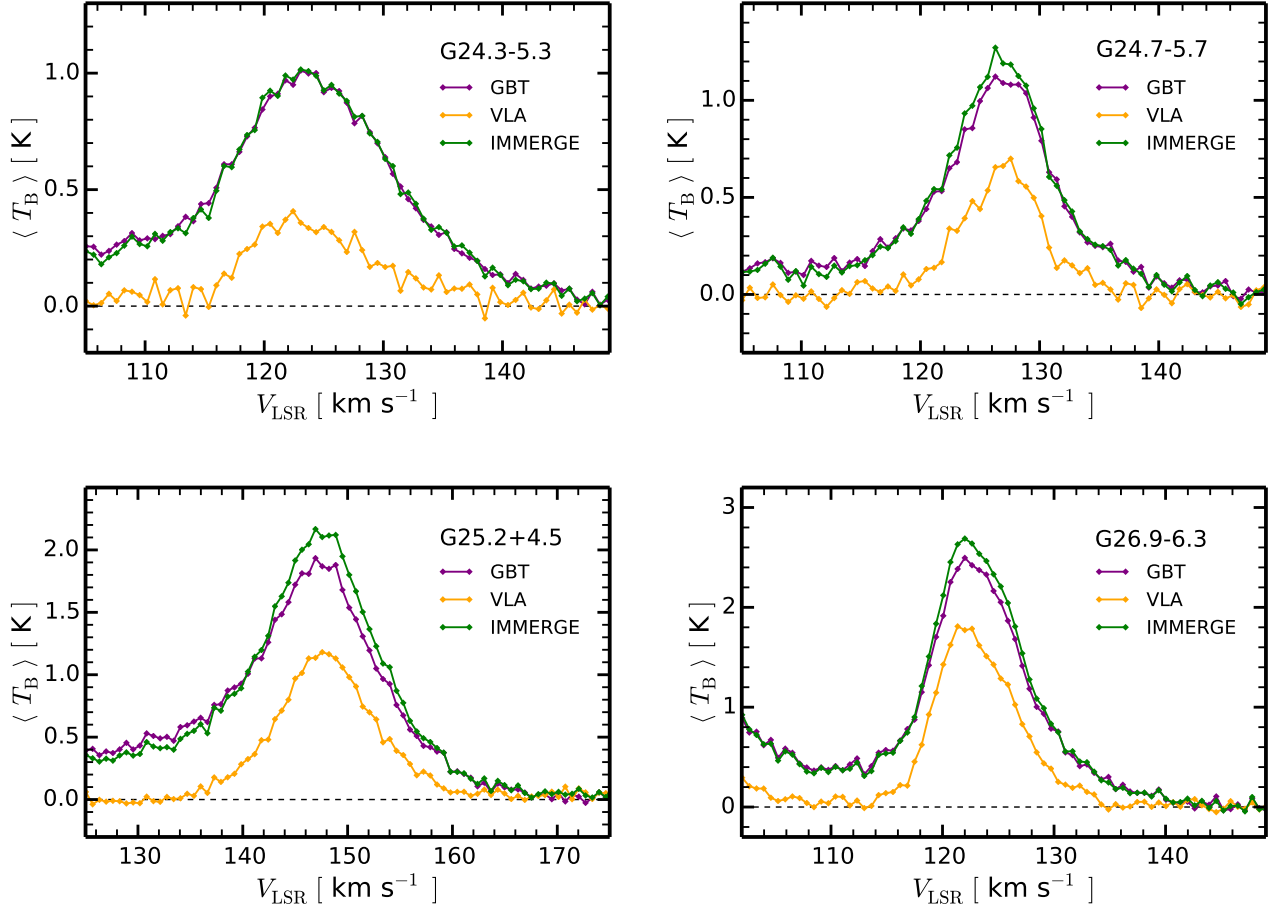


Fig. 4.— Page 2 of 3 — Mean line profiles in brightness temperature T_b , at the center of each field for clean VLA data (orange), GBT data (purple) and results of running IMMERGE on these two images with $f_{\text{cal}}=0.87$ and no tapering (green). This sum is calculated over all pixels in an 80 by 80 pixel box. The comparison shows how well the total single-dish flux is recovered by IMMERGE.

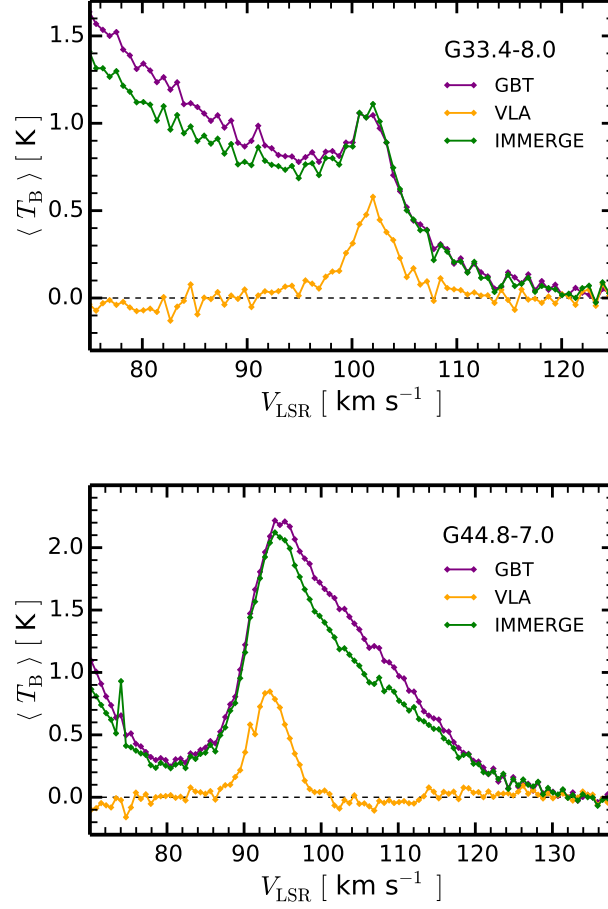


Fig. 4.— Page 3 of 3 — Mean line profiles in brightness temperature T_b , at the center of each field for clean VLA data (orange), GBT data (purple) and results of running IMMERGE on these two images with $f_{\text{cal}}=0.87$ and no tapering (green). This sum is calculated over all pixels in an 80 by 80 pixel box. The comparison shows how well the total single-dish flux is recovered by IMMERGE.

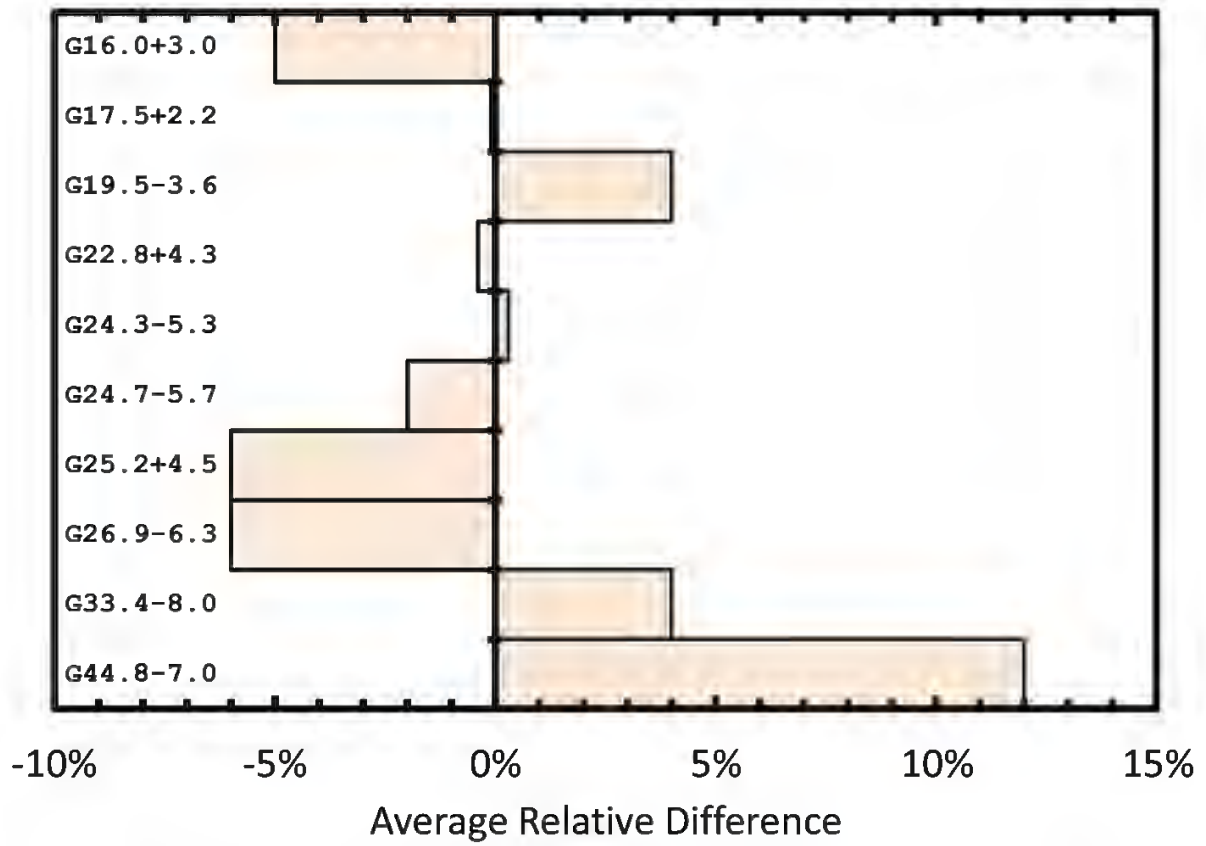


Fig. 5.— Quantitative measure of the difference between GBT and IMMERGE spectra defined by eq. 1. The small differences indicate that the data reduction procedure has restored the missing flux in the line.

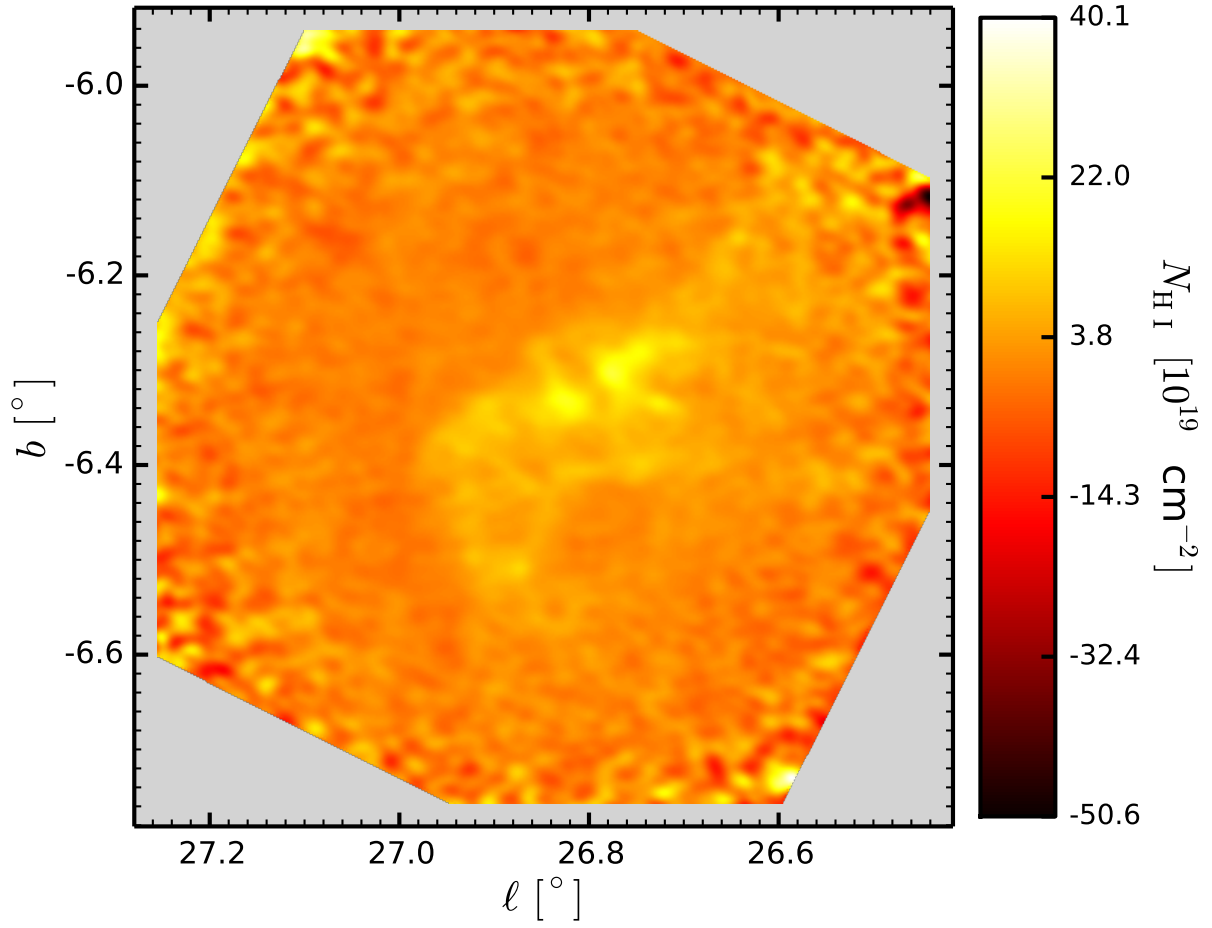


Fig. 6.— An example of an H I column density map with no noise threshold applied, showing the distinct radial increase in noise pattern arising from the VLA primary beam correction. This map of cloud G26.9 – 6.3 was made from 51 spectral channels covering the velocity range $108.47 \leq V_{\text{LSR}} \leq 140.68 \text{ km s}^{-1}$.

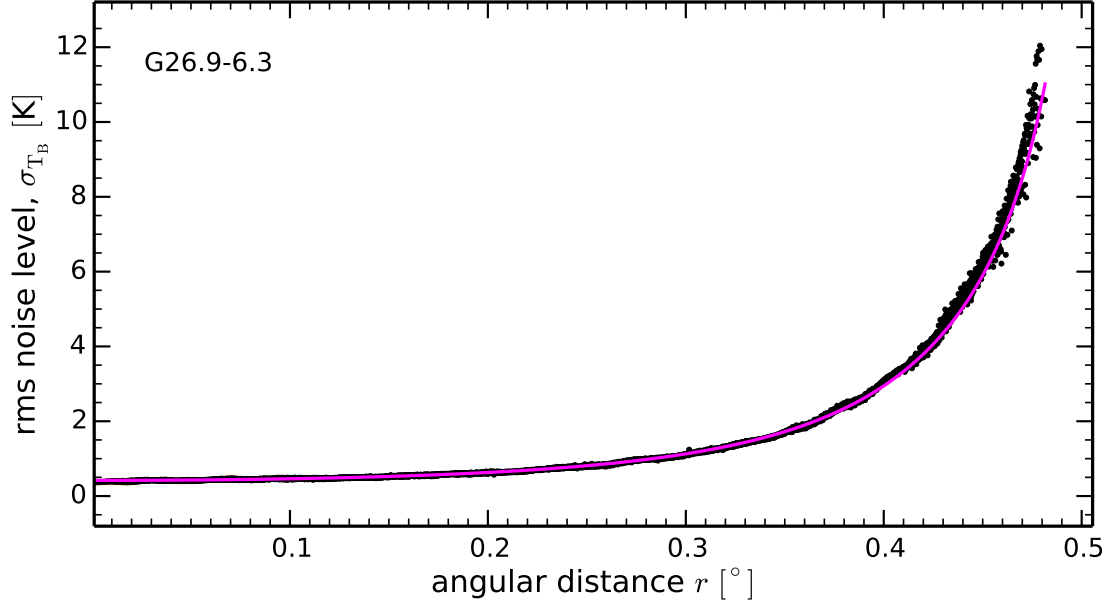


Fig. 7.— The rms noise value $\sigma_{\text{T}_B}(r)$ for the final G26.9 – 6.3 VLA+GBT cube as a function of angular distance r from the center of the field of view. The values of scattered points in this plot were calculated from the same data cube as the map in Fig. 6, only in a range of 41 line-free channels $150.34 \leq V_{\text{LSR}} \leq 176.11 \text{ km s}^{-1}$. The magenta curve fit was obtained by multiplying each point by the corresponding beam gain factor from eq. 2, averaging, then multiplying the resulting mean value $\sigma_0 = 0.42 \text{ K}$ by the same gain factor (eq. 4).

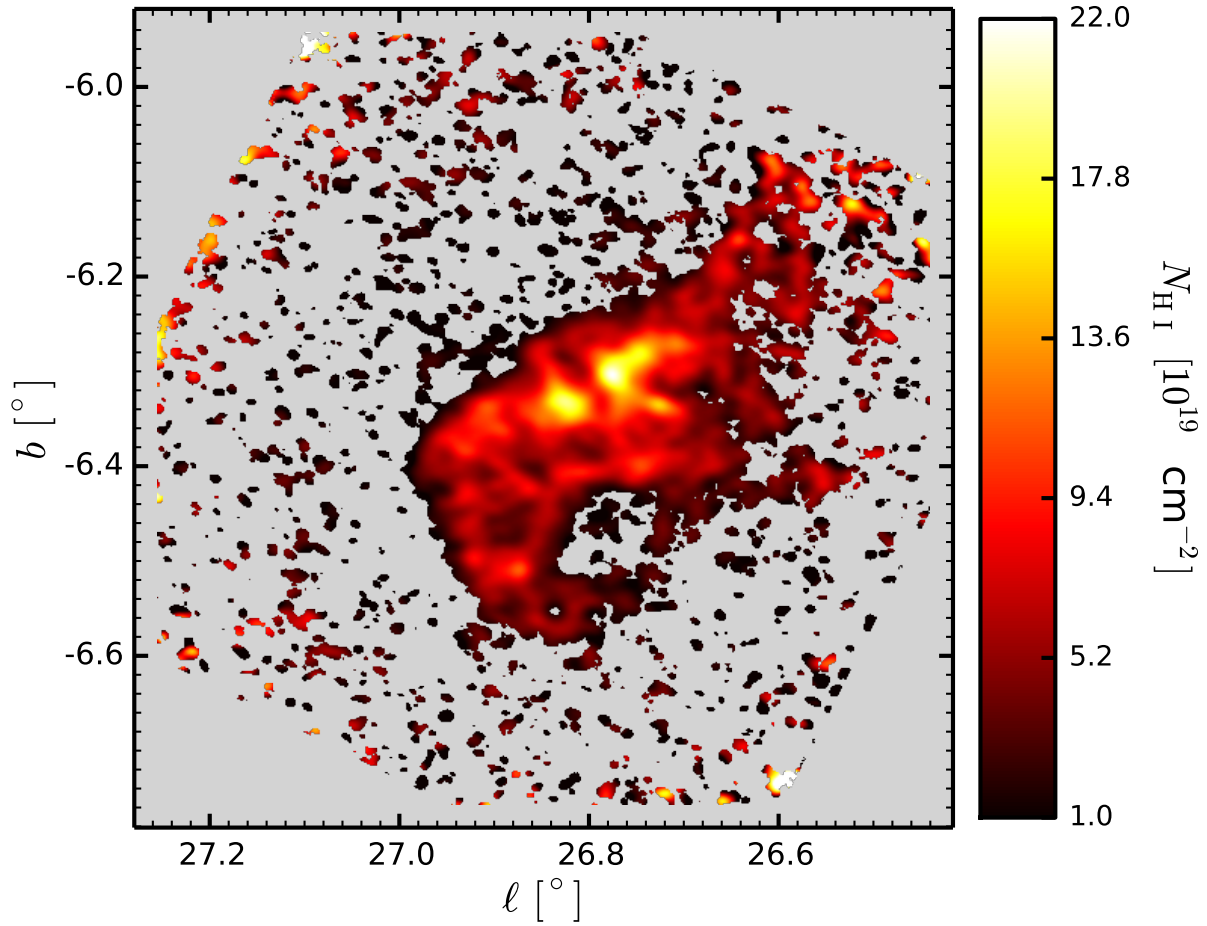


Fig. 8.— H I column density map of G26.9 – 6.3 displaying the same data as Fig. 6, where spectra with values below $3\sigma(r)$ were flagged and not plotted, as explained in § 4.7. The noise $\sigma(r)$ was calculated using eq. (4) with values of σ_0 and f from Table 4. The figure shows data over the interval $1 \times 10^{19} \leq N_{\text{HI}} \leq 2.2 \times 10^{20} \text{ cm}^{-2}$, where the lower limit is three times the column density noise at the center of the field.

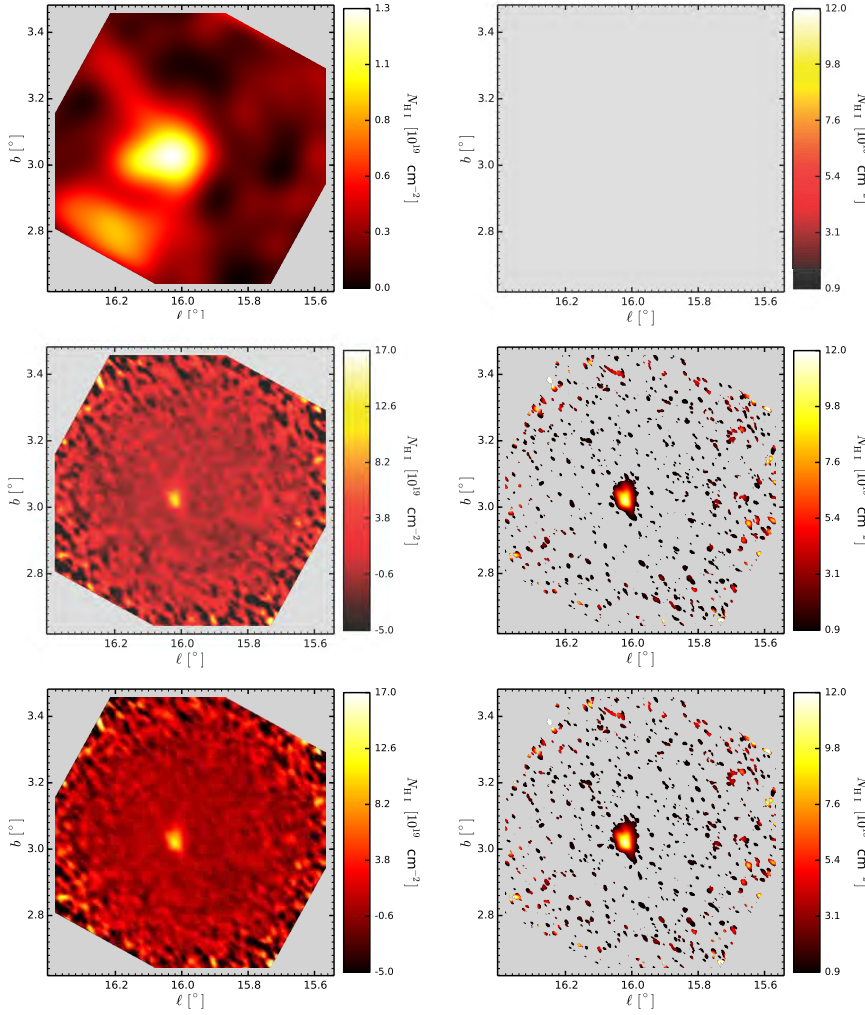


Fig. 9.— Comparison of H I column density maps of G16.0 – 3.0, integrated over 36 spectral channels in the interval $132.3 \leq V_{\text{LSR}} \leq 154.8 \text{ km s}^{-1}$. 3 channels at $139.4 - 140.6 \text{ km s}^{-1}$ were flagged due to RFI and replaced with a linear interpolation. Upper row: GBT data regridded to match the VLA. Middle row: VLA data. Bottom row: The result of IMMERGE, VLA+GBT. Left column: full data. The column density range of the full VLA and VLA+GBT maps (left middle and left bottom correspondingly) of this and all similar figures is fixed at $-5 \times 10^{19} \leq N_{\text{HI}} \leq 1.7 \times 10^{20} \text{ cm}^{-2}$. Right column: The same maps as in left column, only thresholded by $3\sigma(r)$ of the VLA noise level, similar to Fig. 8. All three are shown over the same interval of column densities, $9 \times 10^{18} \leq N_{\text{HI}} \leq 1.2 \times 10^{20} \text{ cm}^{-2}$, where the lower limit is three times the column density noise at the center of the field. This shows the GBT data (upper right) compared to both VLA signal and noise values. In this particular case, alone among the ten clouds under consideration, the GBT signal is never greater than the VLA $3\sigma(r)$ level.

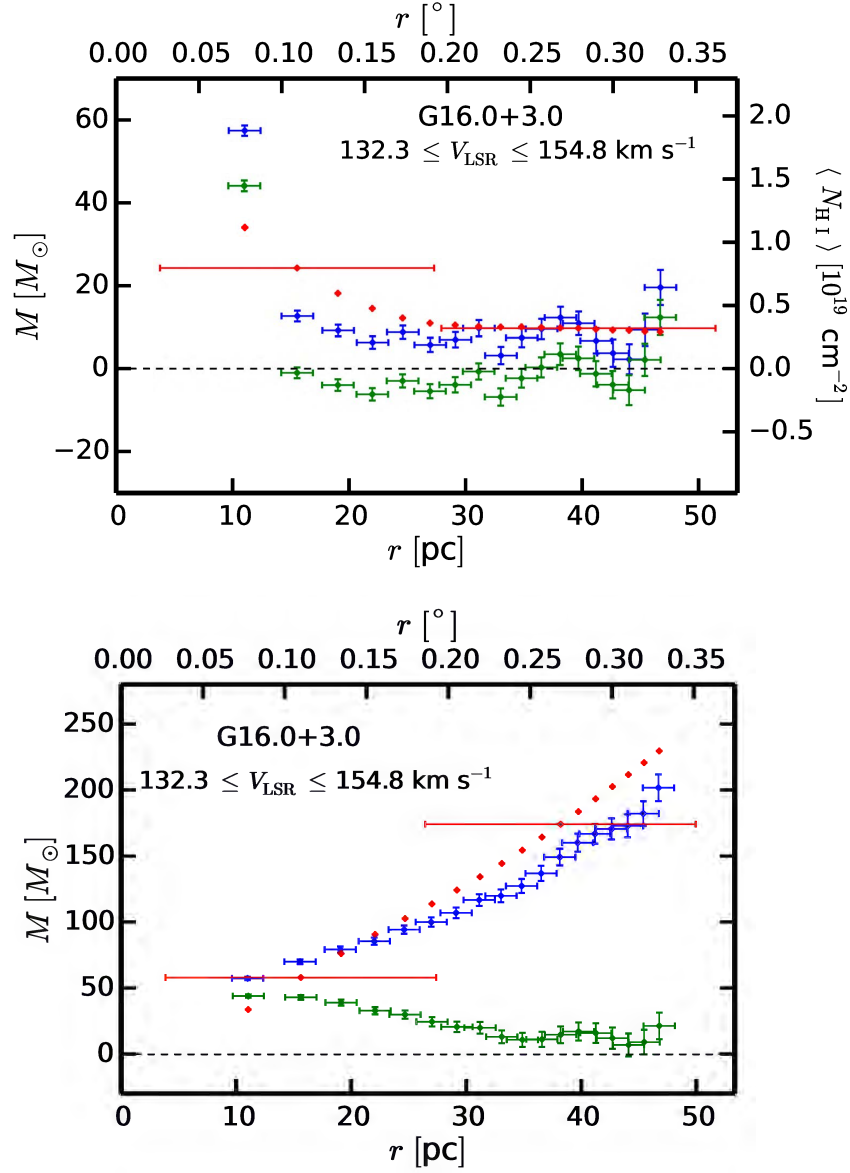


Fig. 10.— Radial mass distribution for G16.0 + 3.0. Top: mass and average column density per annulus, with sequence designed to ensure equal areas in each bin, as explained in § 5.1. Bottom: integral mass within circles of each radius. Red – GBT data, corresponding to Fig. 9 top left (only two of the error bars are shown to avoid clutter). Green – VLA data, corresponding to Fig. 9 middle left. Blue – VLA+GBT data, corresponding to Fig. 9 bottom left.

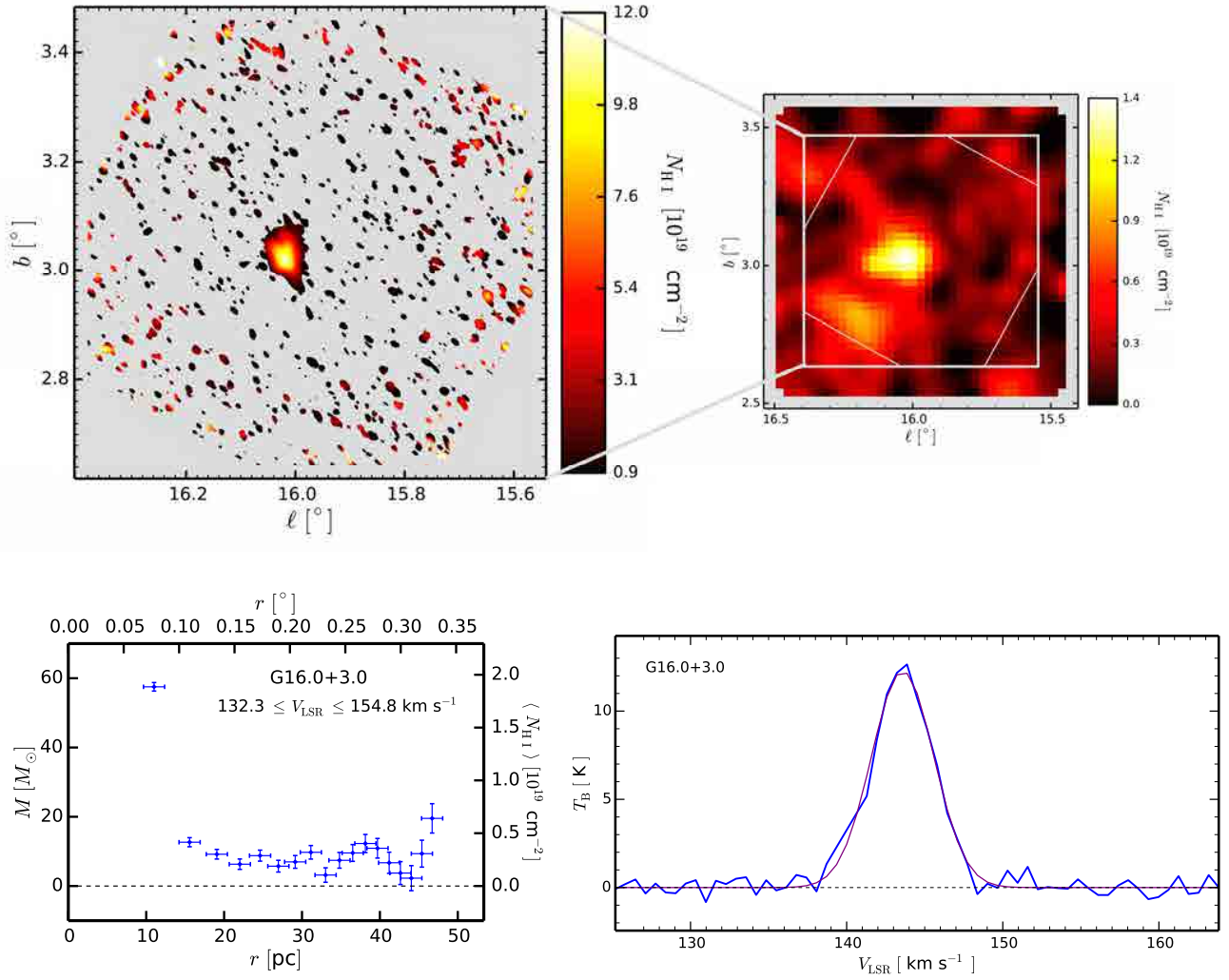


Fig. 11.— Summary of G16.0 + 3.0. Top left: $3\sigma(r)$ thresholded VLA+GBT map, same as Fig. 9 bottom right. Top right: GBT column density map integrated over the same velocity range, with the box marking the extent of the VLA map. Lower left: radial mass distribution, same as blue points in Fig. 10 top. Lower right: final spectrum toward the position of the peak N_{HI} with the Gaussian whose parameters are given in Table 6. This is a very little cloud with no structure, unlike any other cloud in the group. It is the smallest cloud by far, has one of the narrowest line widths implying a kinetic temperature < 500 K, and has the largest mean density by a factor ≈ 5 (see §5.4). About one half of the cloud mass is confined to the dense and very compact core. It may be in the region of the Galaxy excavated by a hot wind from the Galactic nucleus as discussed in §5.4. This isolated cloud is similar to the dense cores seen in other clouds, e.g., G26.9 – 6.3.

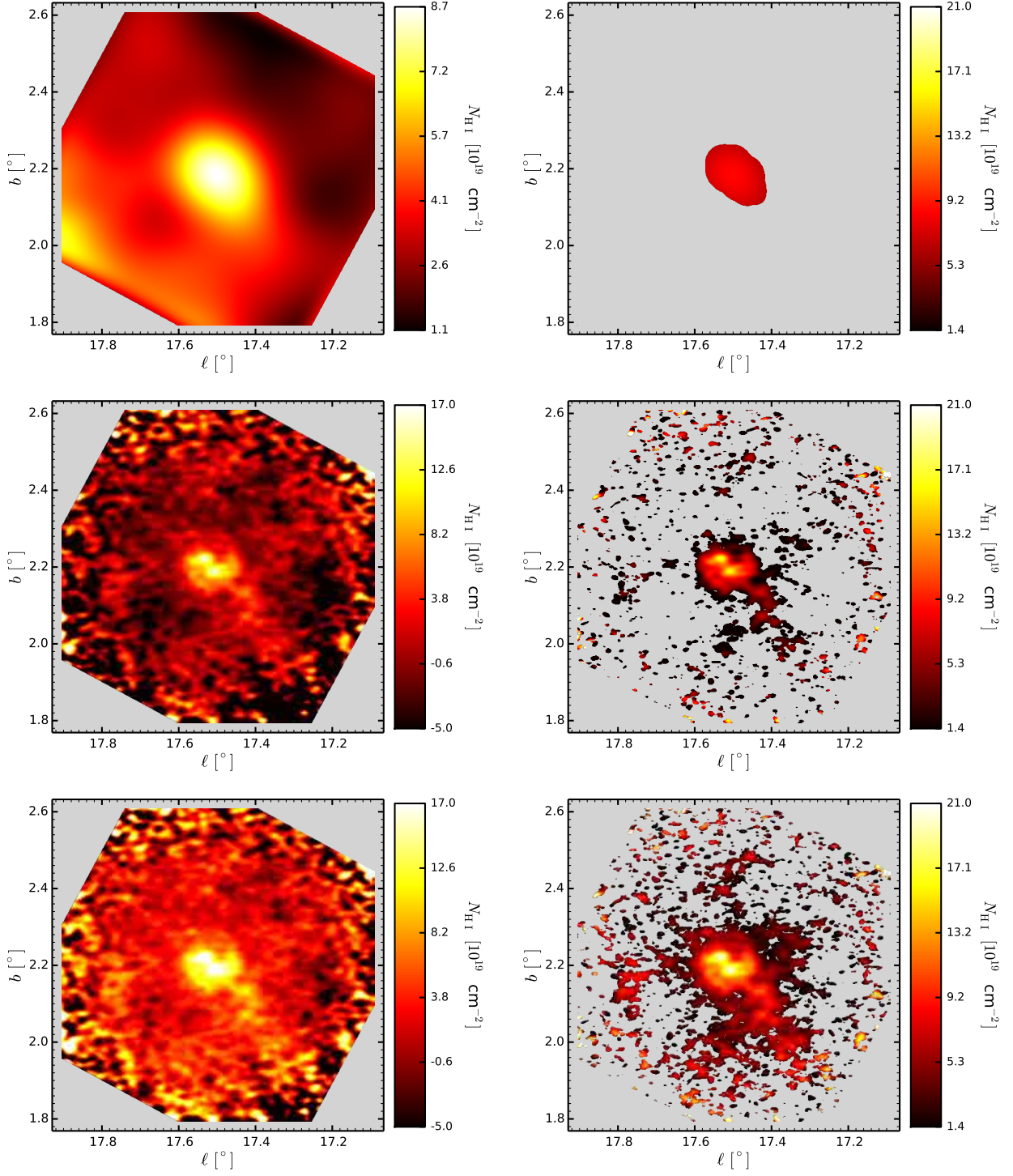


Fig. 12.— H I column density maps for G17.5 + 2.2, integrated over 48 spectral channels in the interval $122.8 \leq V_{\text{LSR}} \leq 153.0 \text{ km s}^{-1}$, as described in the caption to Fig. 9

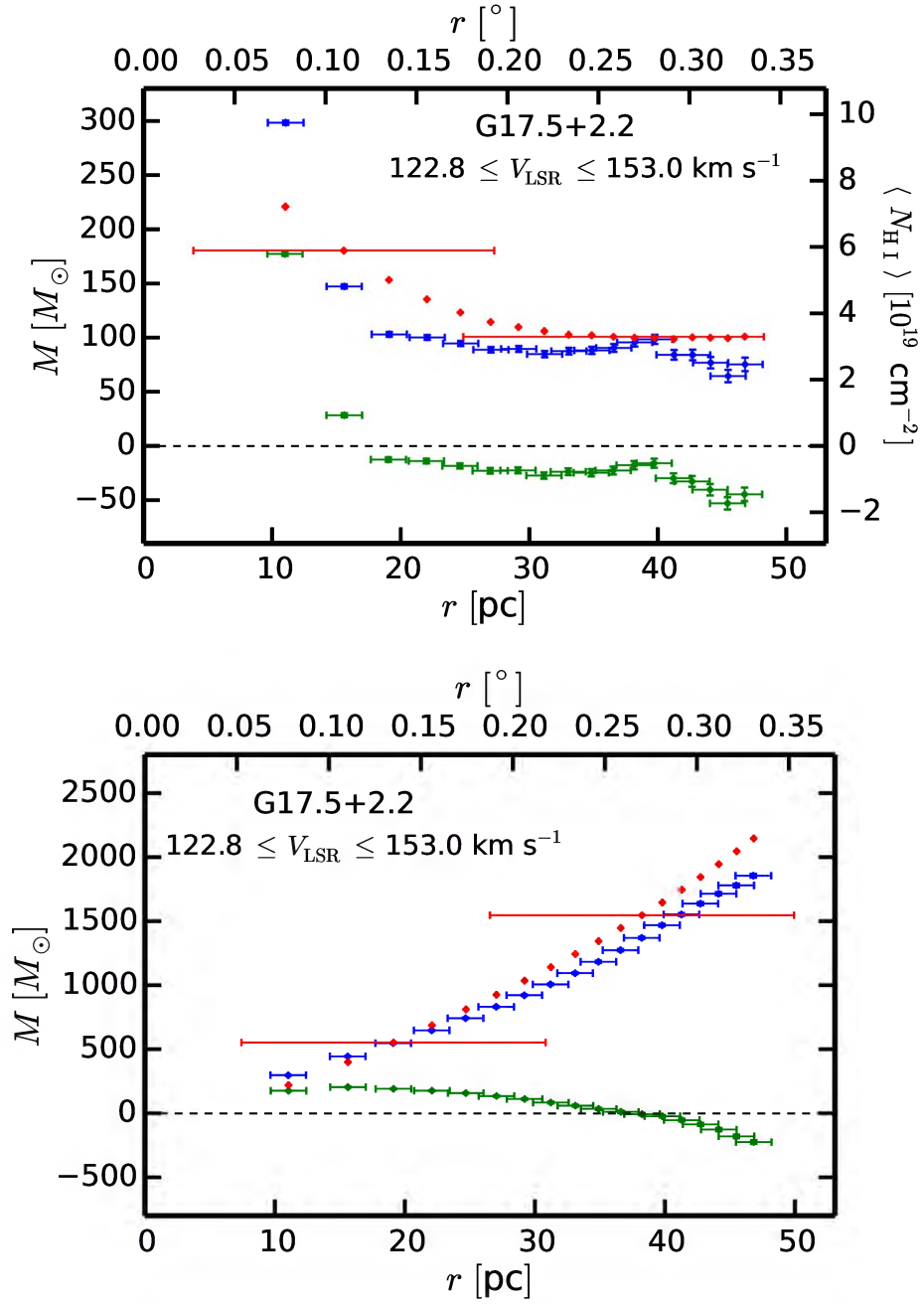


Fig. 13.— Radial mass profiles for G17.5 + 2.2 as described in the caption to Fig. 10.

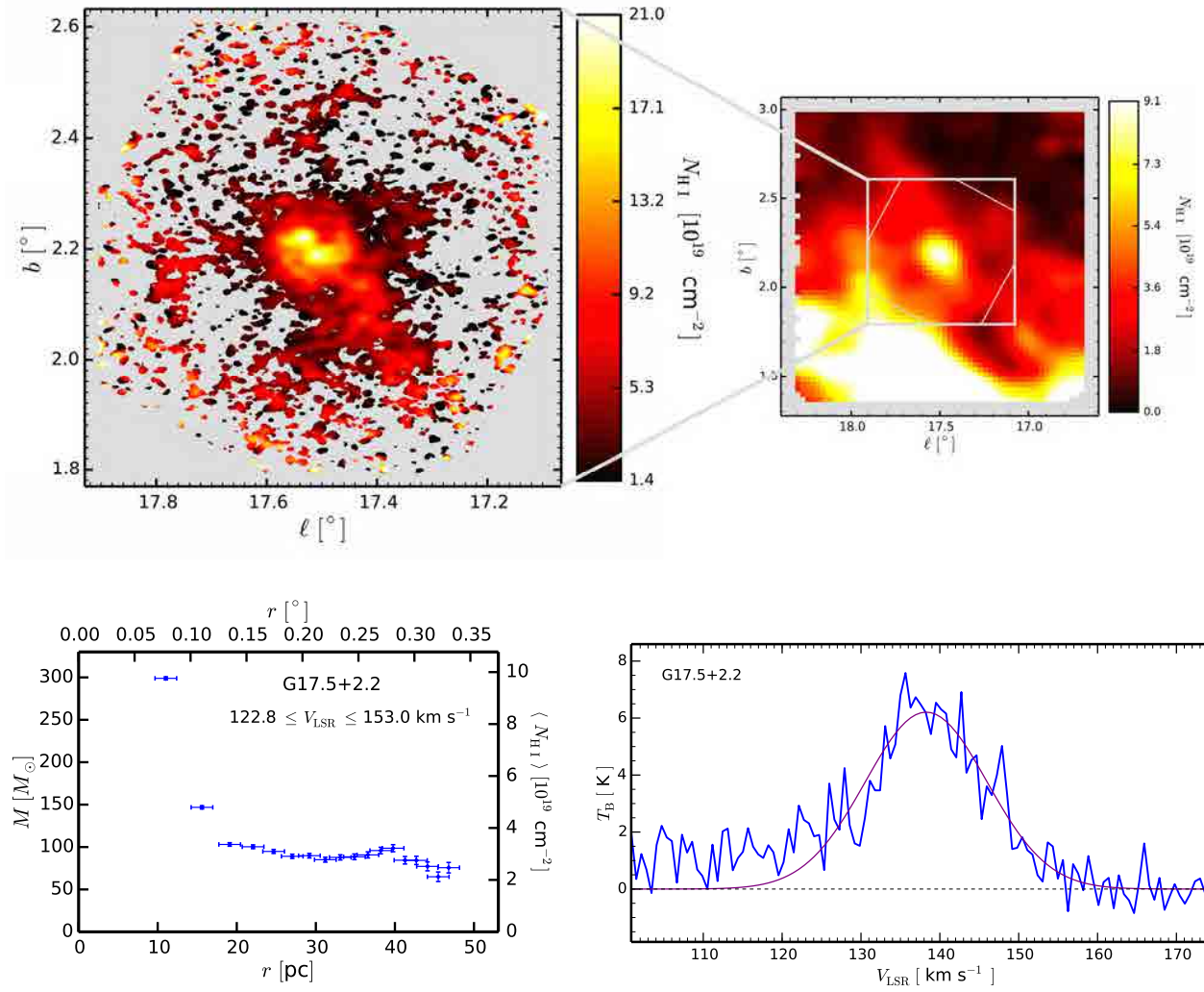


Fig. 14.— Summary of G17.5 + 2.2 as described in the caption to Fig. 11. A cloud with an almost circular core ≈ 30 pc in diameter that contains two peaks of similar N_{HI} and about half of the cloud’s mass. Surrounding the core are irregular structures of low N_{HI} , the densest of which has a cometary appearance stretching to lower longitude and latitude.

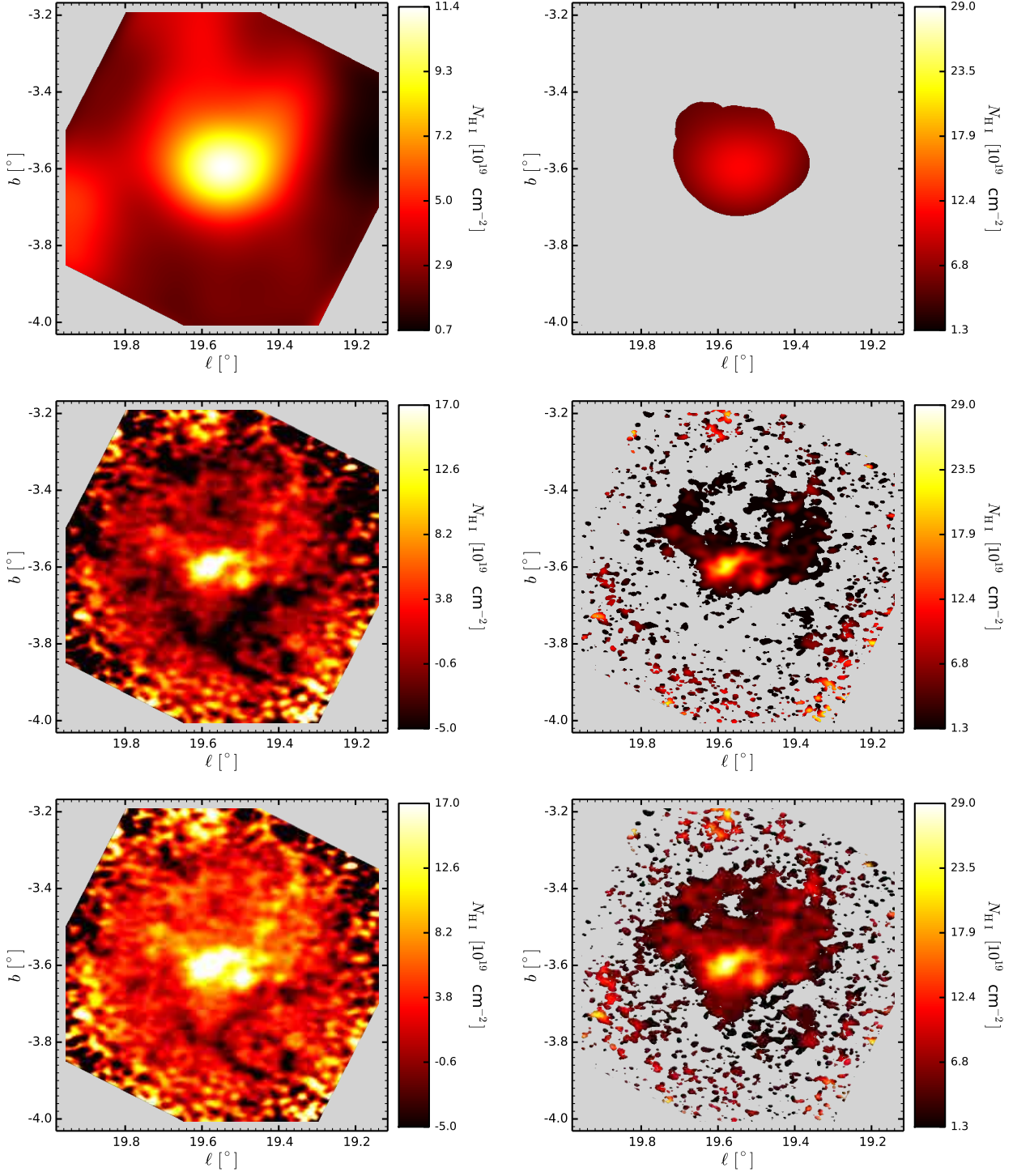


Fig. 15.— H I column density maps for G19.5 – 3.6, integrated over 56 spectral channels in the interval $107.8 \leq V_{\text{LSR}} \leq 143.2 \text{ km s}^{-1}$, as described in the caption to Fig. 9.

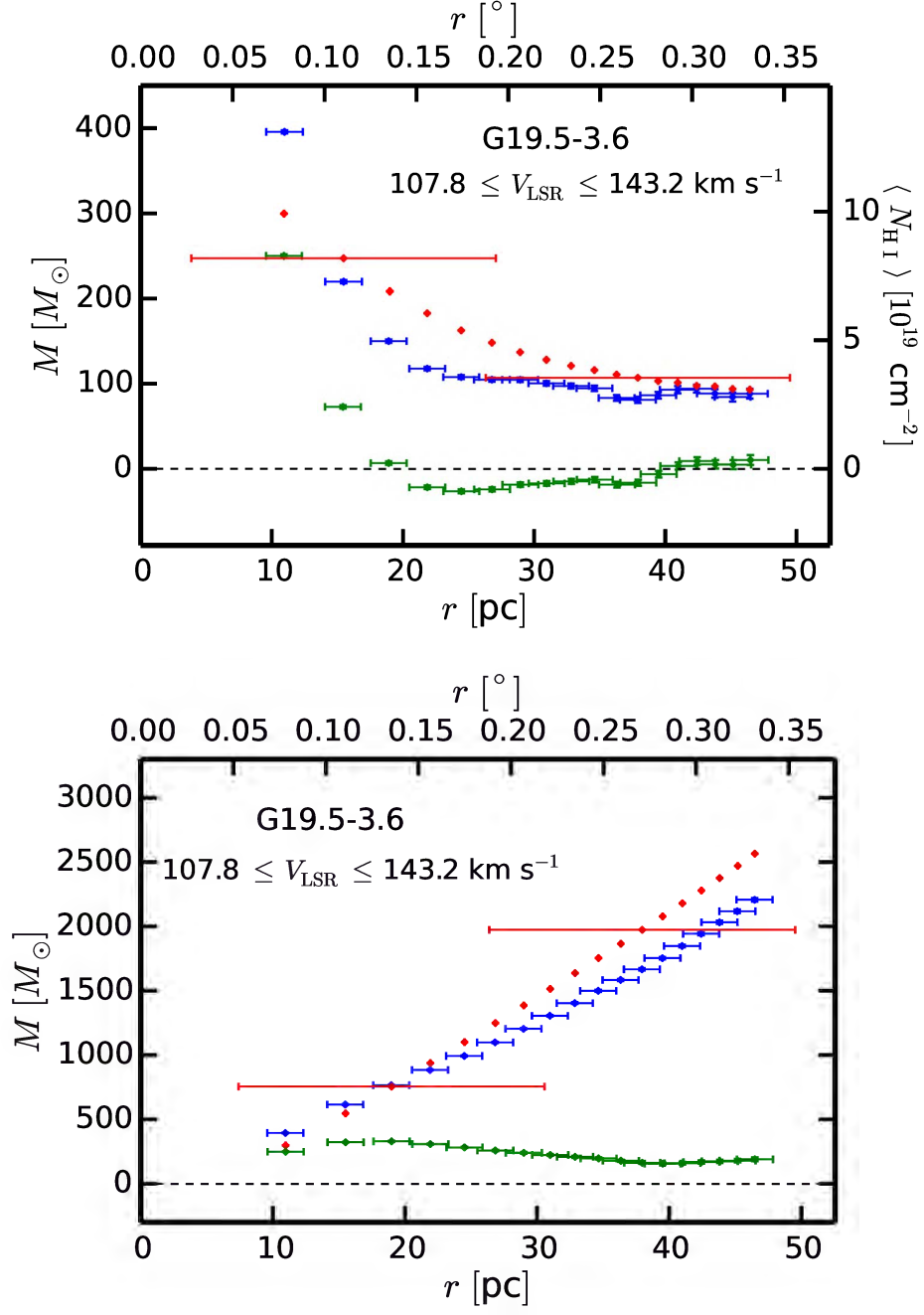


Fig. 16.— Radial mass profiles for G19.5 – 3.6 as described in the caption to Fig. 10.

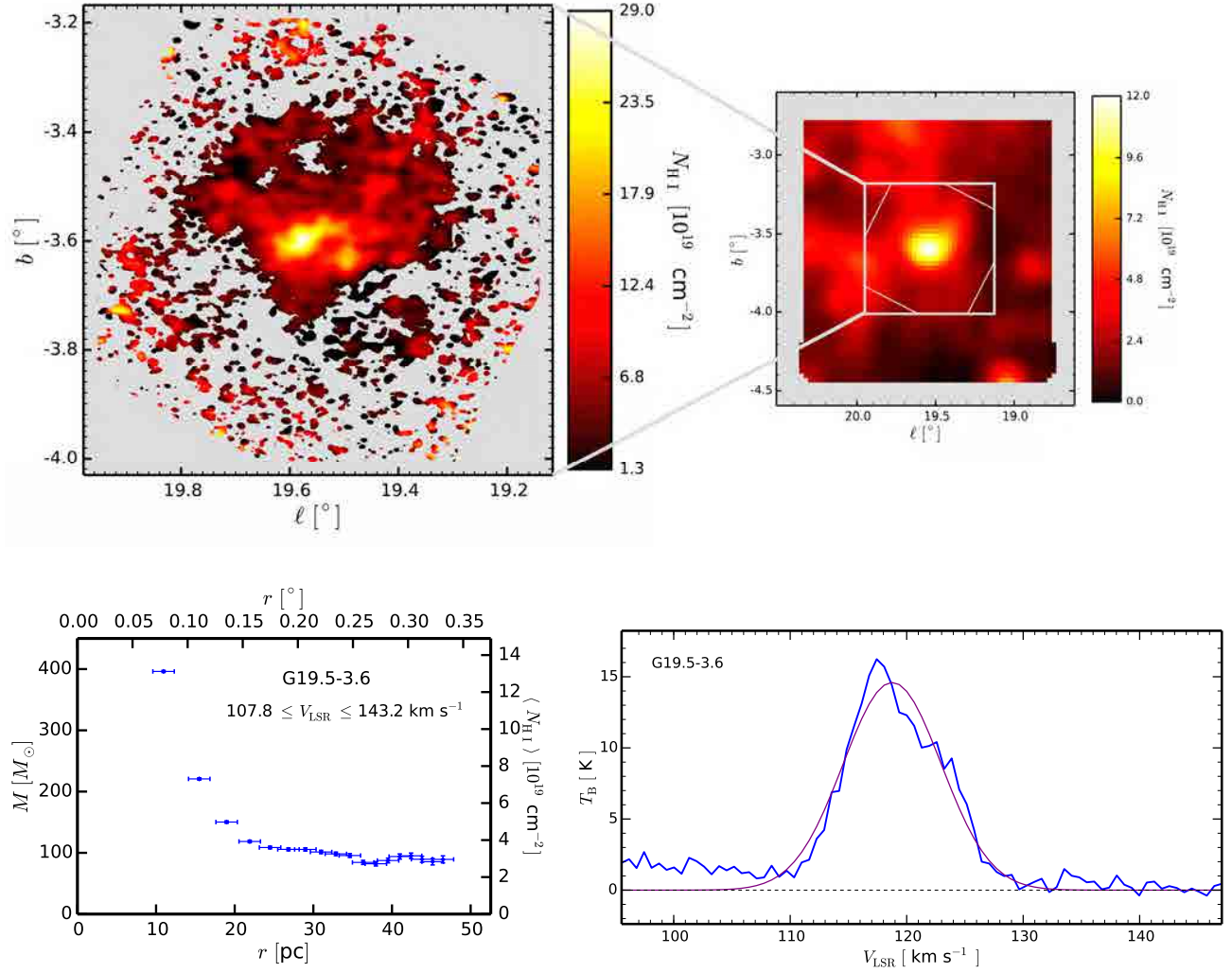


Fig. 17.— Summary of G19.5 – 3.6 as described in the caption to Fig. 11. One of the two largest clouds in the sample with a diameter > 60 pc and a mass around $800 M_{\odot}$ in the central region and more than $1000 M_{\odot}$ in its extended envelope. The cloud’s boundary is sharpest away from the Galactic plane and there are two “tails” of less bright emission stretching back toward the plane.

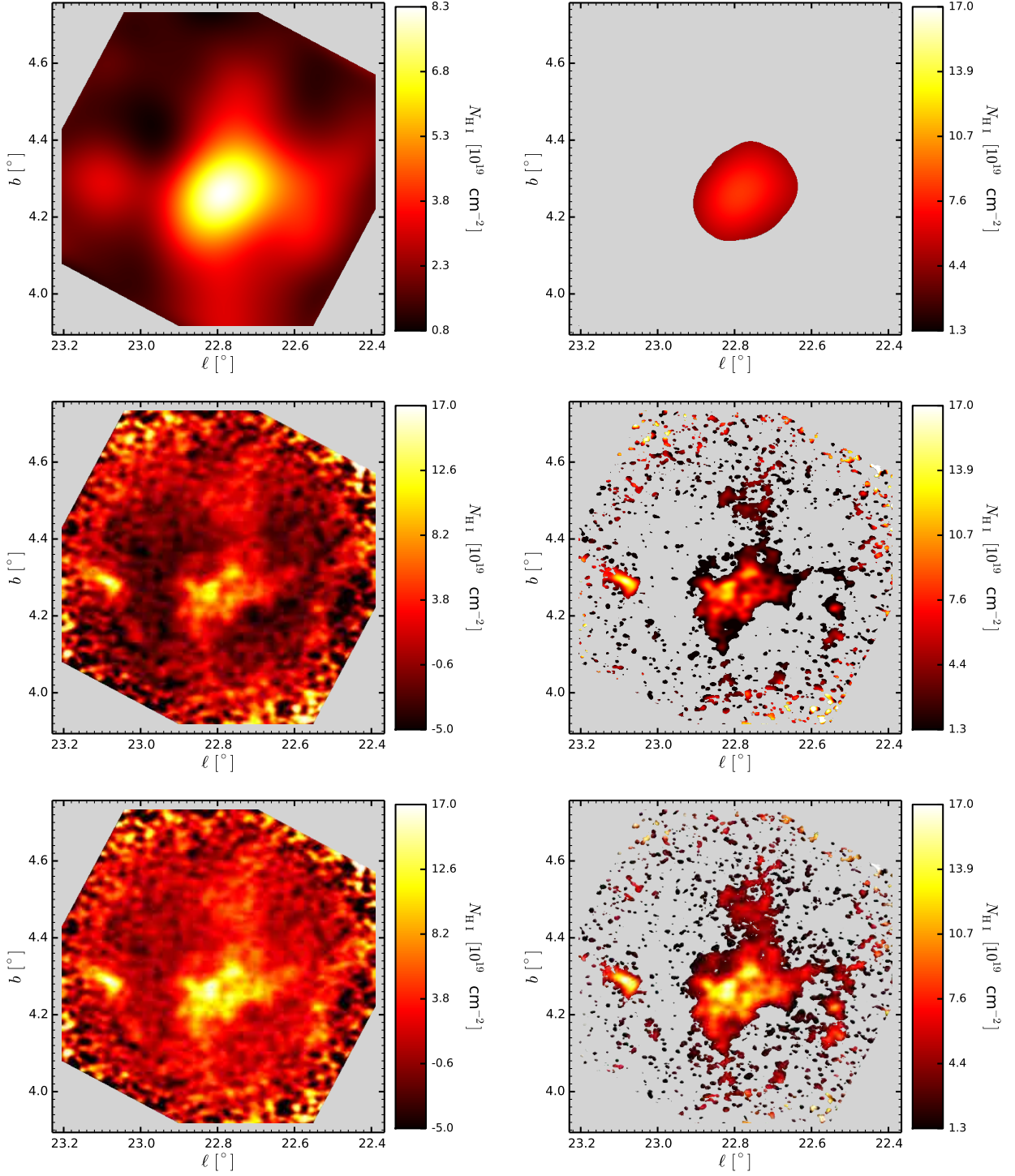


Fig. 18.— H I column density maps for G22.8 + 4.3, integrated over 46 spectral channels in the interval $125.2 \leq V_{\text{LSR}} \leq 154.1 \text{ km s}^{-1}$, as described in the caption to Fig. 9.

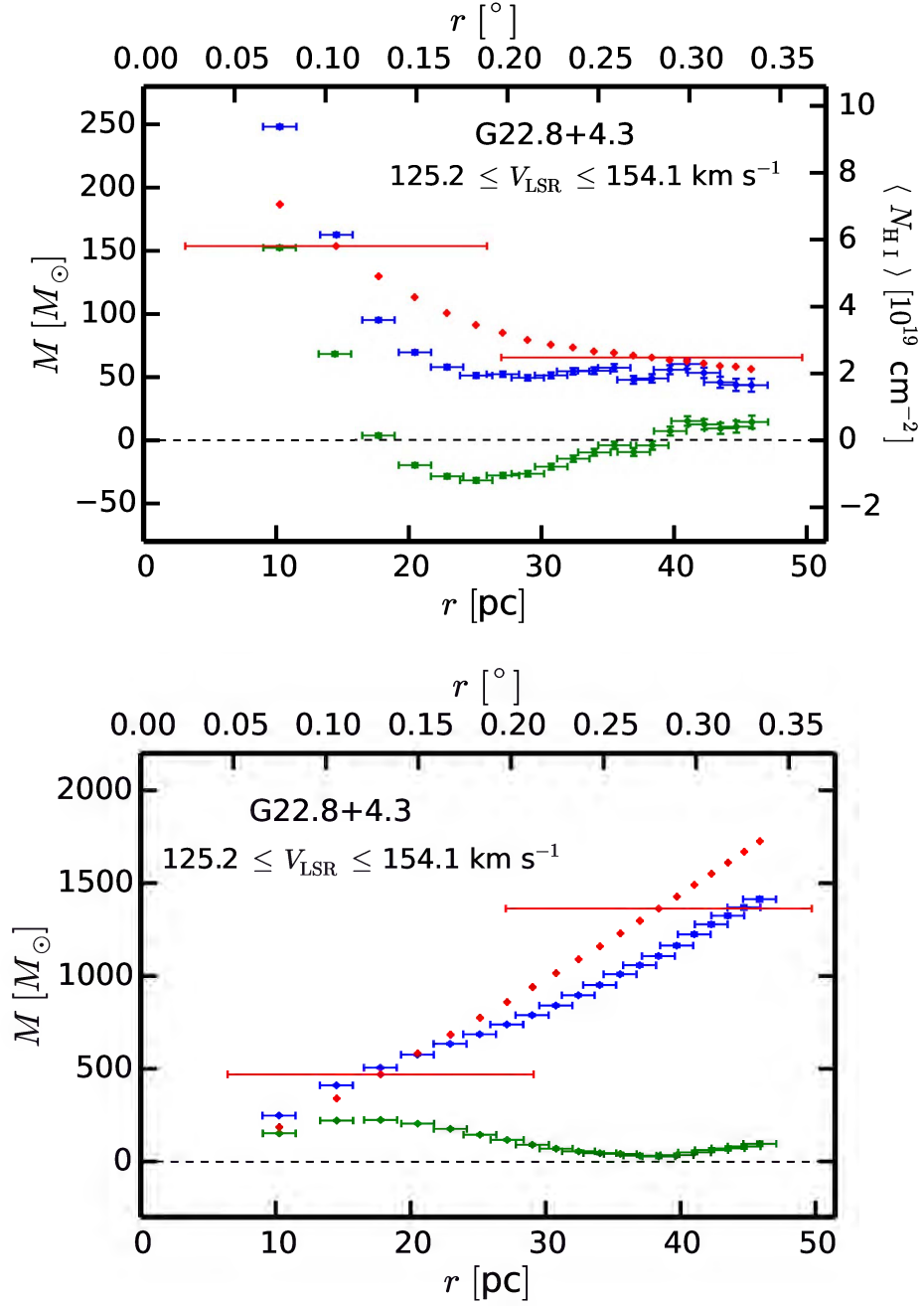


Fig. 19.— Radial mass profiles for G22.8 + 4.3 as described in the caption to Fig. 10.

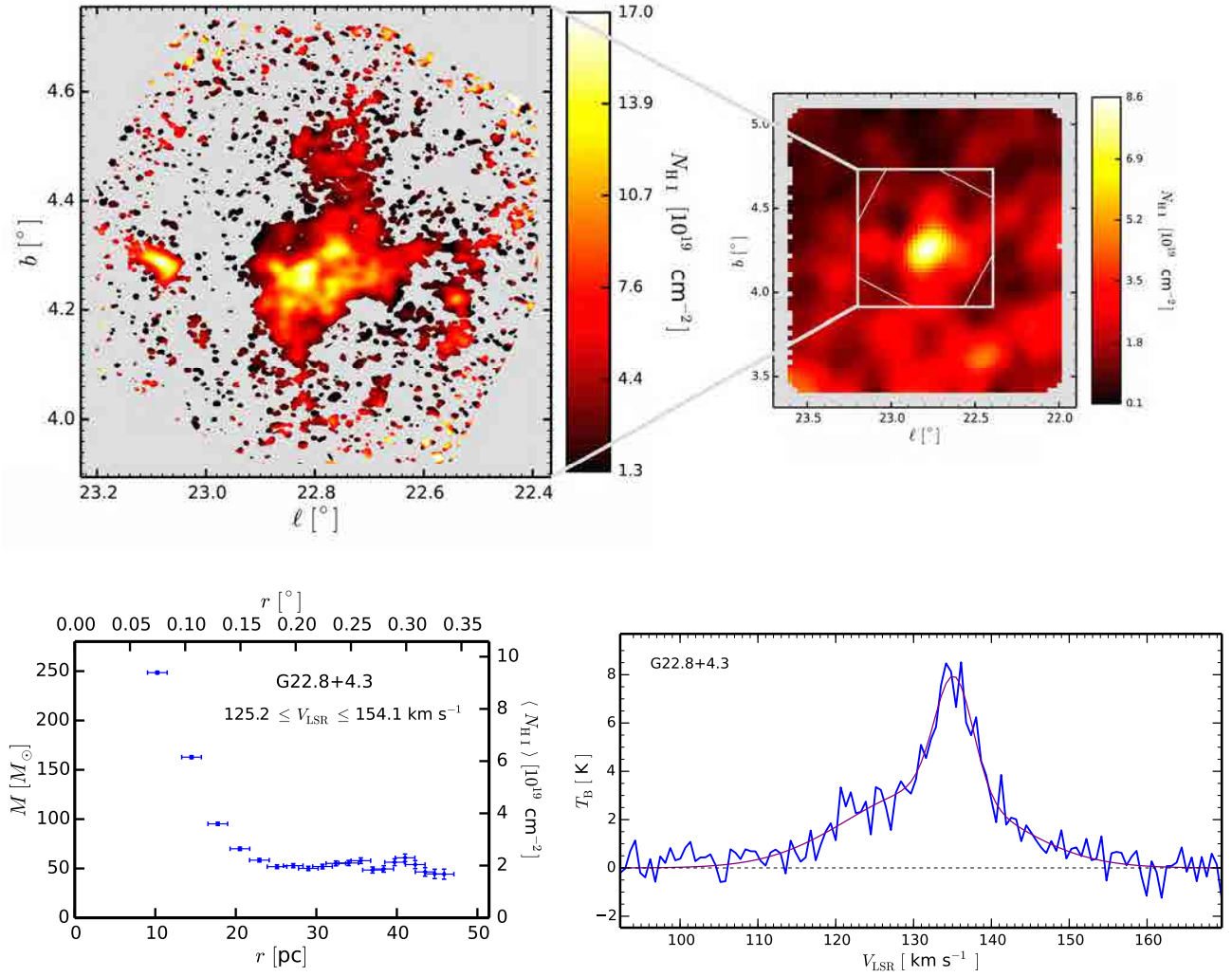


Fig. 20.— Summary of G22.8+4.3 as described in the caption to Fig. 11. This cloud consists of several fragments, one of which (G23.1 + 4.3) has a size of 20 pc and a mass of 70 M_{\odot} , similar to the small isolated cloud G16.0 + 3.0. The line at the peak N_{HI} consists of two components, one broad and one narrow.

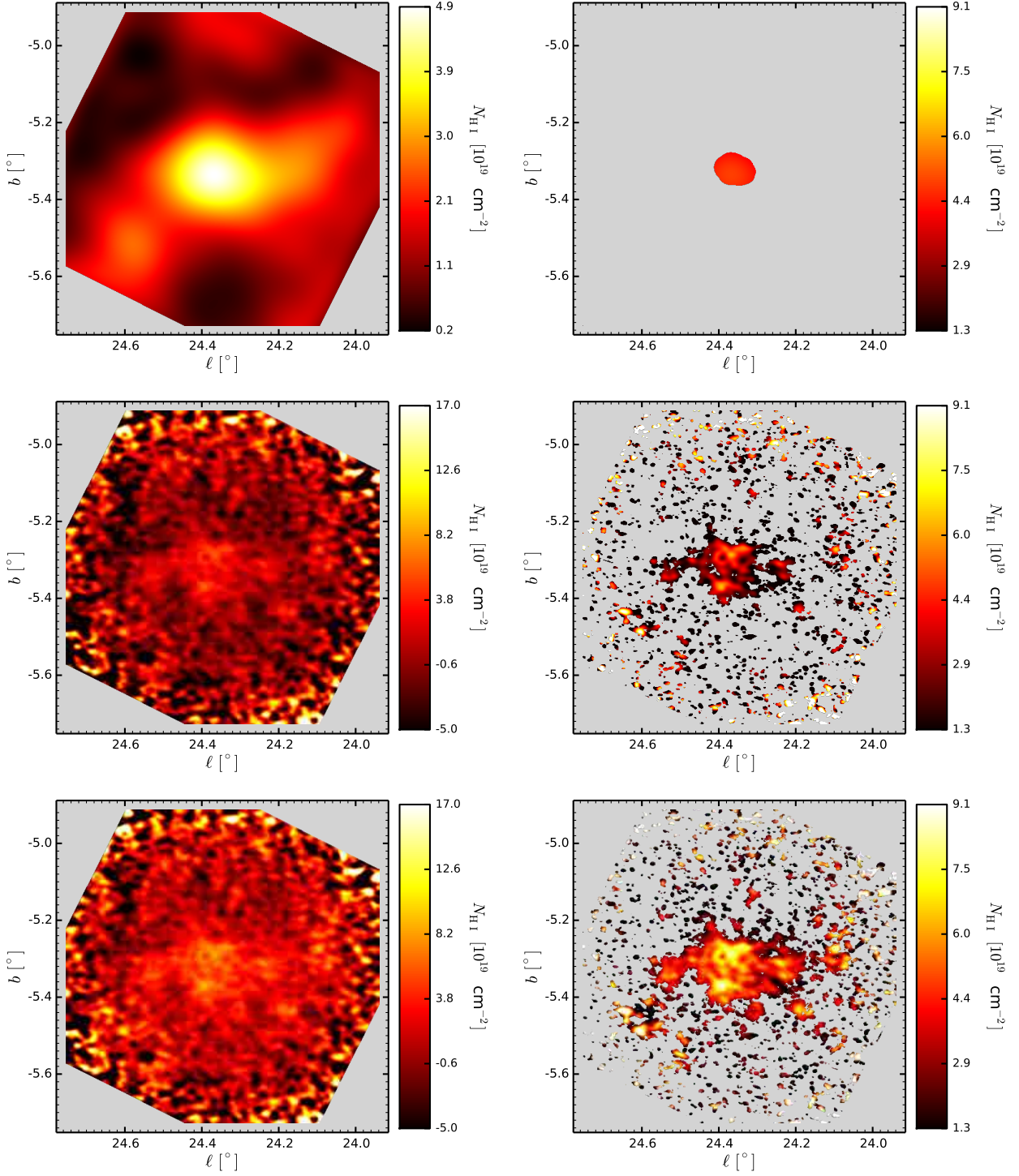


Fig. 21.— H I column density maps for G24.3 – 5.3, integrated over 70 spectral channels in the interval $107.0 \leq V_{\text{LSR}} \leq 151.4 \text{ km s}^{-1}$, as described in the caption to Fig. 9.

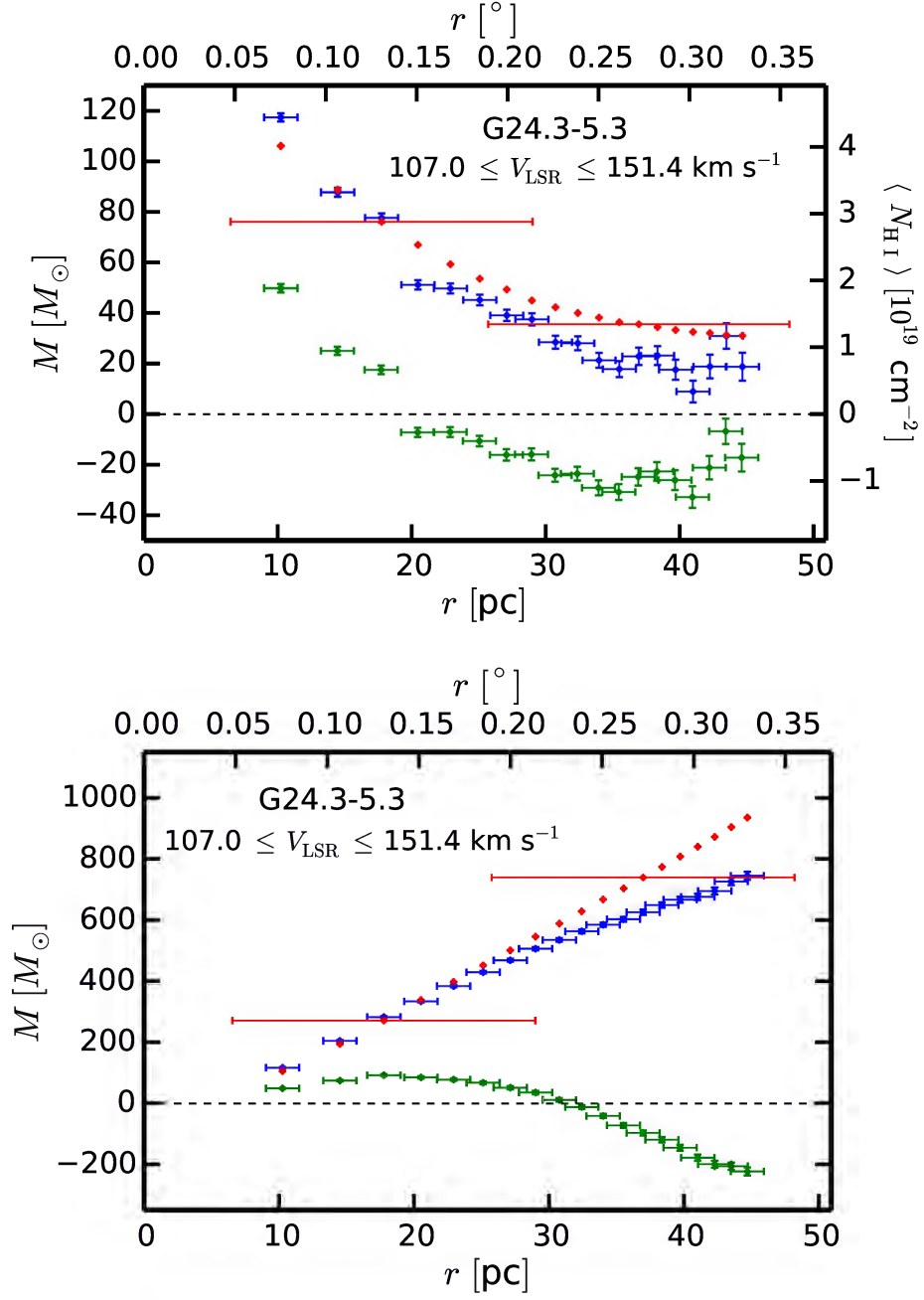


Fig. 22.— Radial mass profiles for G24.3 – 5.3 as described in the caption to Fig. 10.

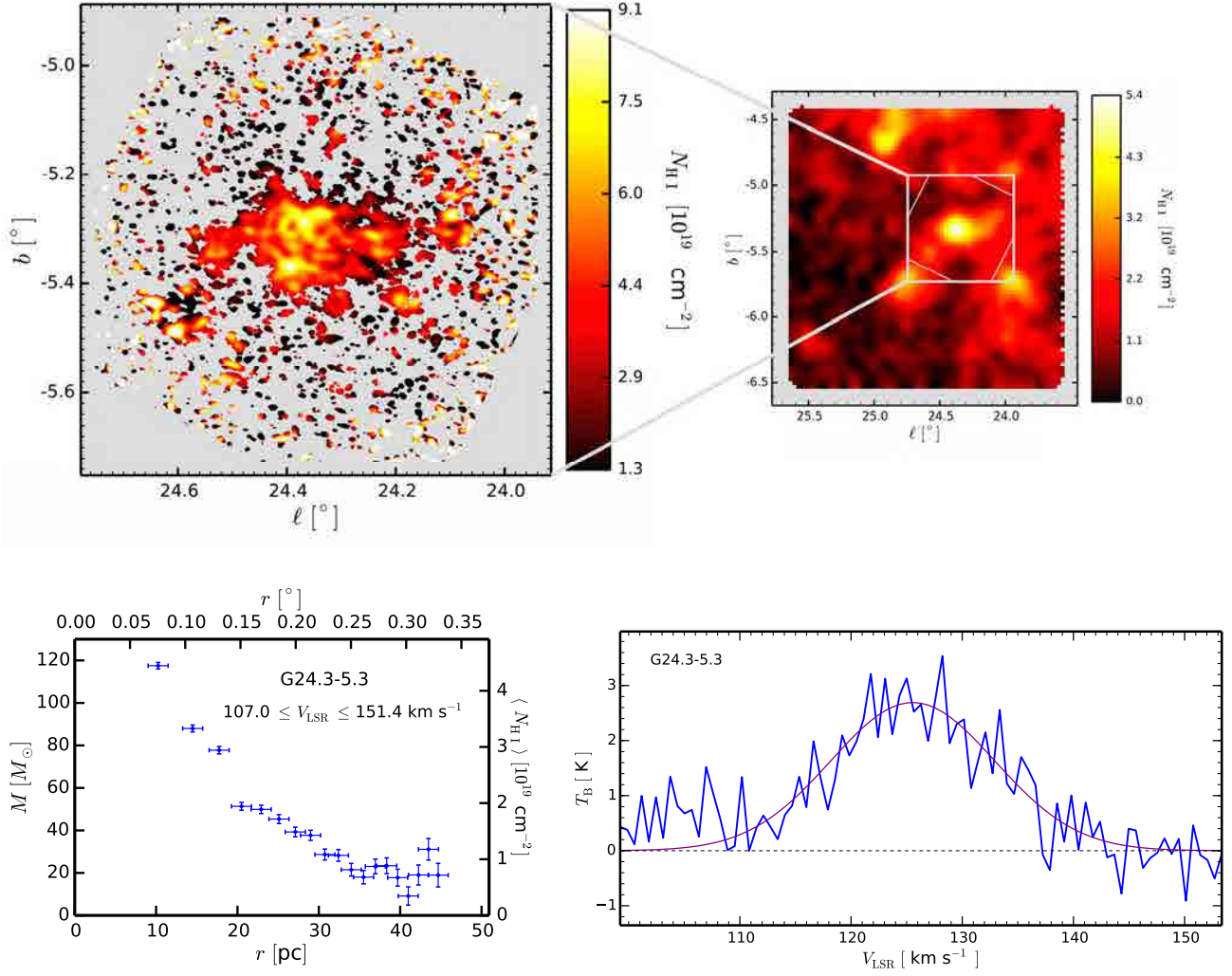


Fig. 23.— Summary of G24.3–5.3 as described in the caption to Fig. 11. This cloud, together with G24.7 – 5.7 and a smaller one that lies between them, form a chain of three clouds connected by diffuse H I emission. G24.3 – 5.3 has no clear core, but rather several column density peaks of similar values spread over the body of the cloud. Its radial mass profile shows the lack of central concentration. In contrast to G16.0 + 3.0, which is a core without an envelope, this cloud is an envelope without a core. With a FWHM of $17.4 \pm 1.1 \text{ km s}^{-1}$, its line is one of the broadest in the sample.

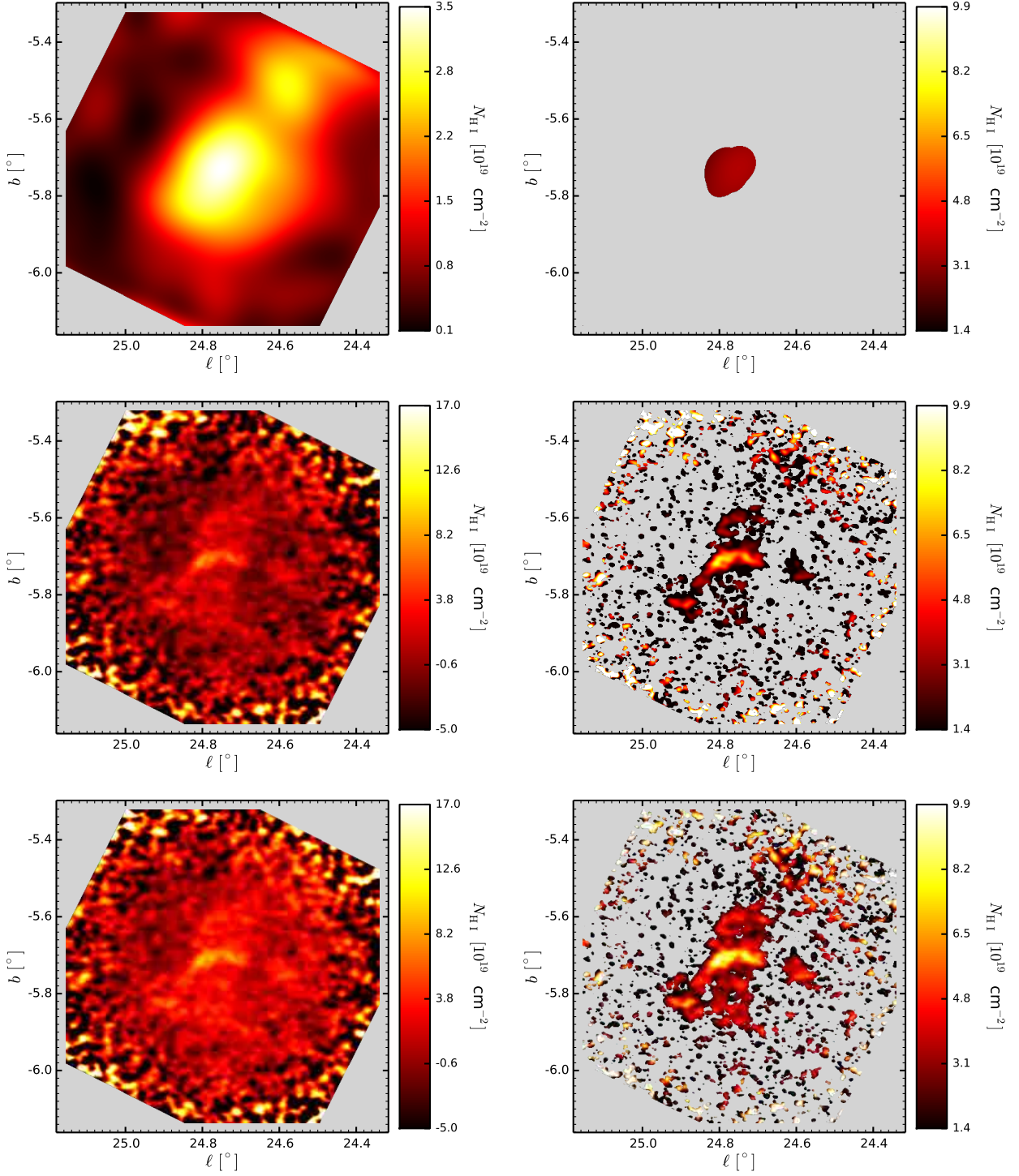


Fig. 24.— H I column density maps for G24.7 – 5.7, integrated over 66 spectral channels in the interval $103.7 \leq V_{\text{LSR}} \leq 145.6 \text{ km s}^{-1}$, as described in the caption to Fig. 9.

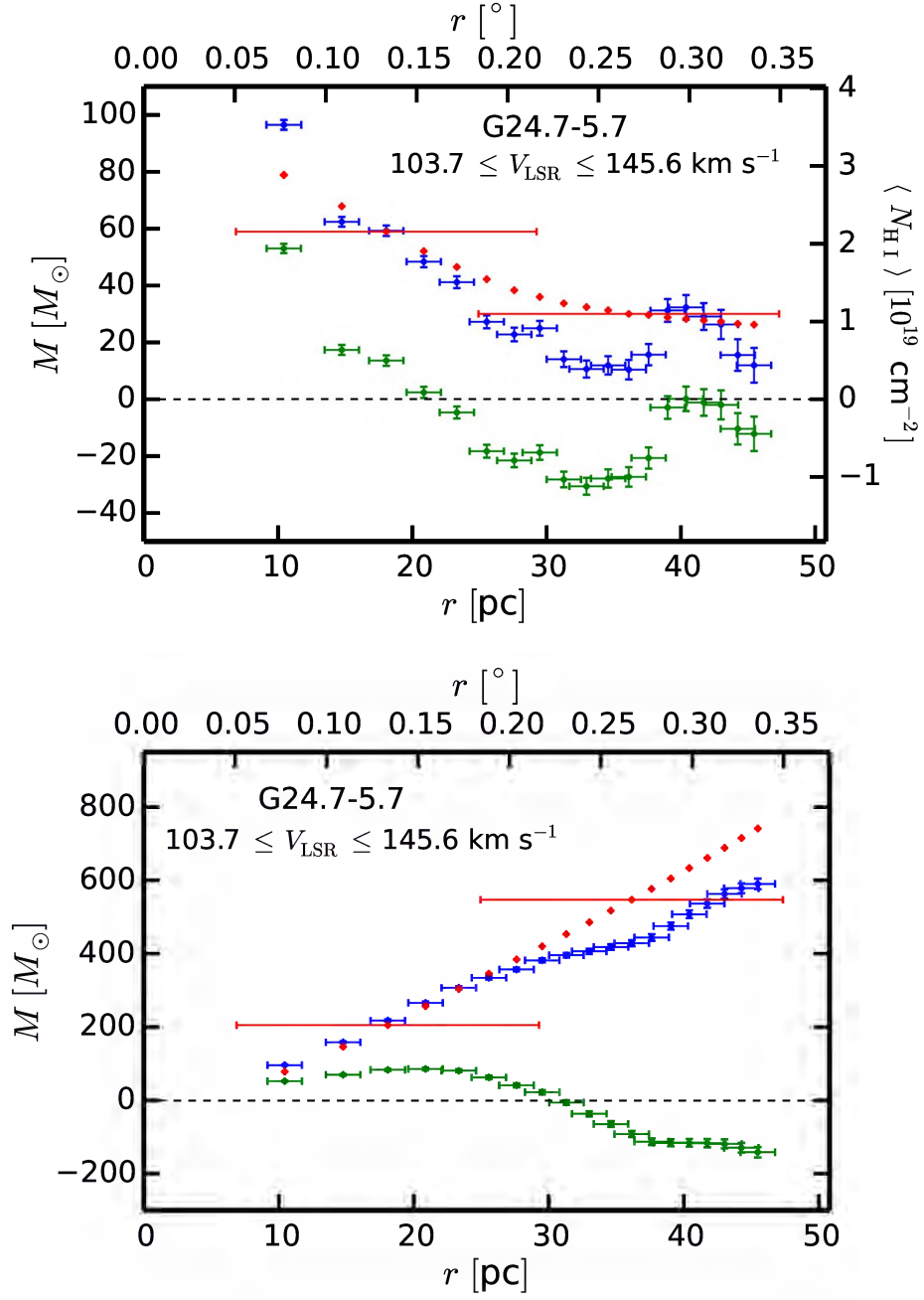


Fig. 25.— Radial mass profiles for G24.7 – 5.7 as described in the caption to Fig. 10.

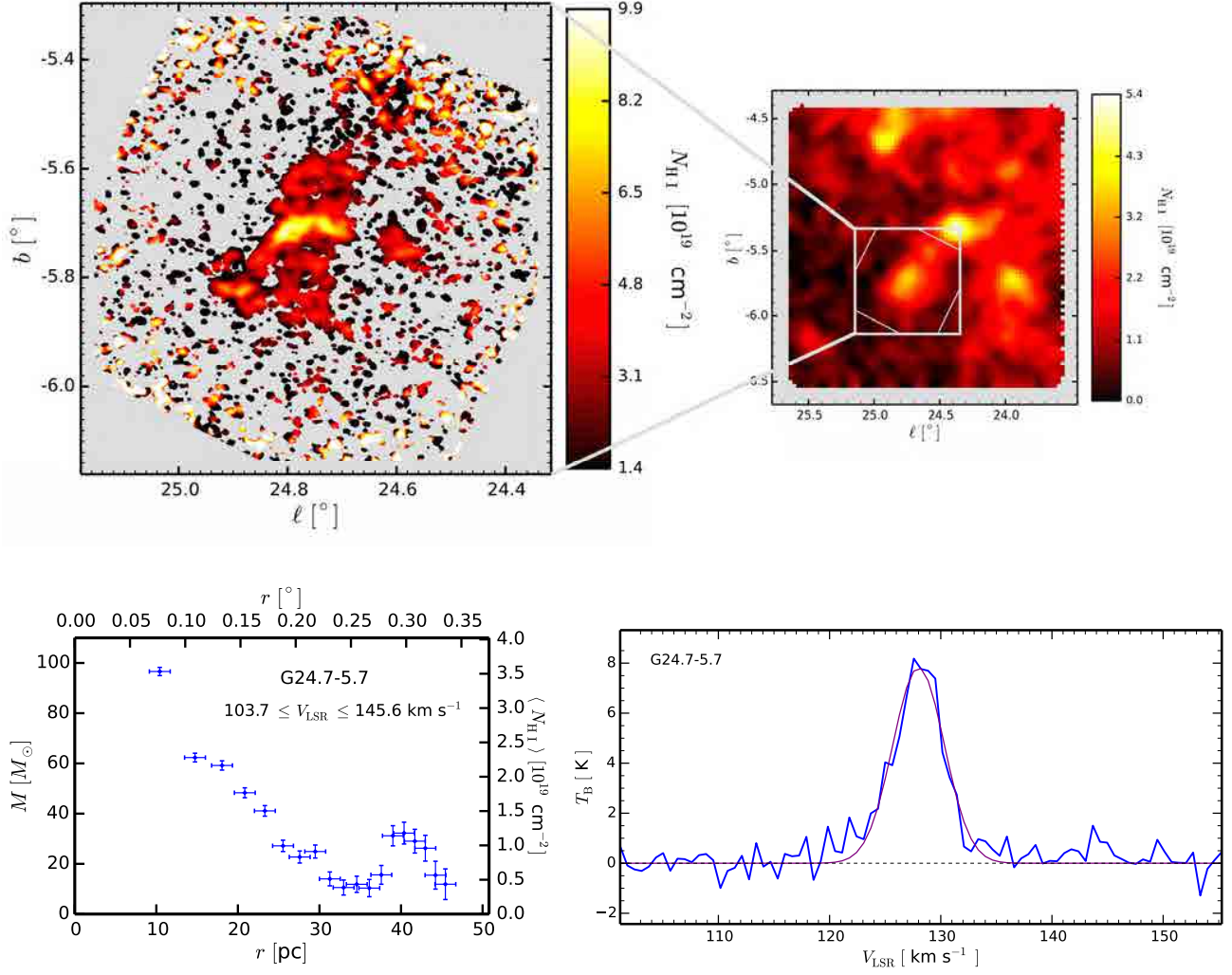


Fig. 26.— Summary of G24.7 – 5.7 as described in the caption to Fig. 11. A relatively small cloud that together with G24.3 – 5.3 and a cloud between them forms a chain of three clouds connected spatially and kinematically. Unlike its companion G24.3 – 5.3, it has a clear core with a narrow line of $\text{FWHM}=5.5 \text{ km s}^{-1}$, but still has a similar range of column densities. The edge of the chain of clouds is quite sharp at higher longitudes.

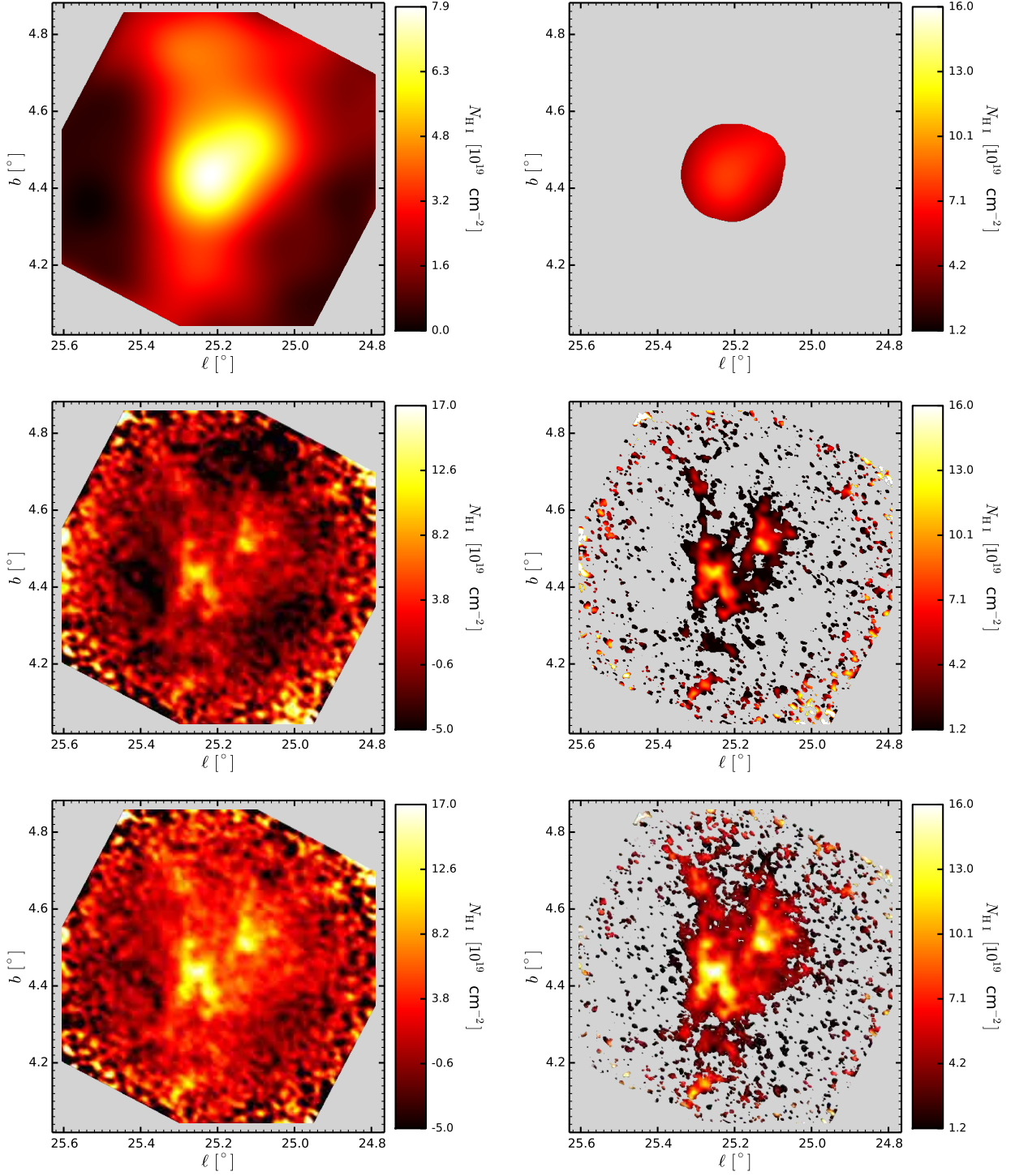


Fig. 27.— H I column density maps for G25.2 + 4.5, integrated over 64 spectral channels in the interval $125.7 \leq V_{\text{LSR}} \leq 166.3 \text{ km s}^{-1}$, as described in the caption to Fig. 9.

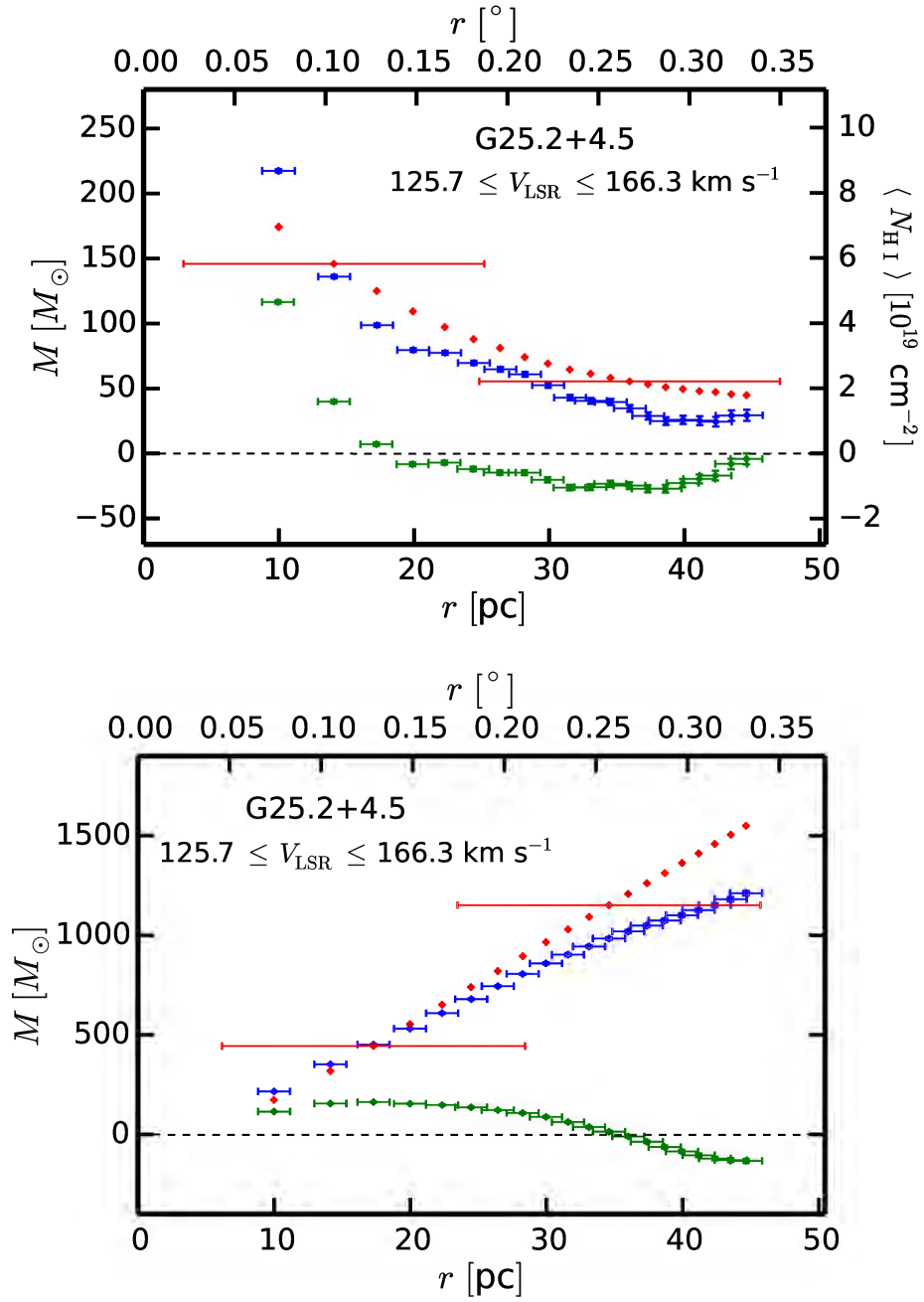


Fig. 28.— Radial mass profiles for G25.2 + 4.5 as described in the caption to Fig. 10.

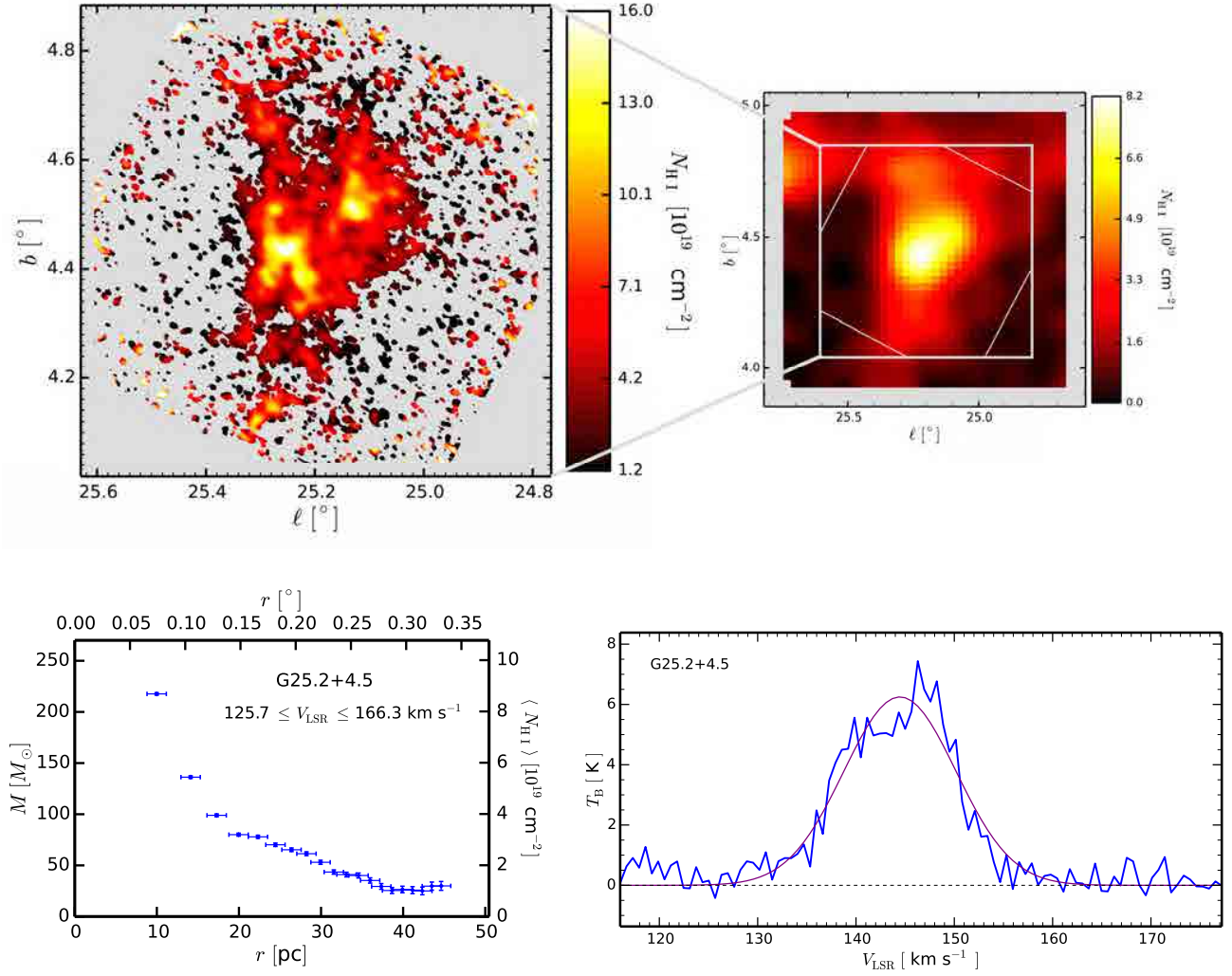


Fig. 29.— Summary of G25.2 + 4.5 as described in the caption to Fig. 11. The VLA data reveal the considerable complexity of this cloud. There seems to be no single core, but instead many dense regions. The broad line with $\text{FWHM}=13.4 \text{ km s}^{-1}$ may indicate the blending of several kinematically distinct components within the $1''.05$ angular resolution of the map, equivalent to 2.35 pc at the adopted distance of the cloud. The cloud has a relatively sharp edge to higher longitudes with diffuse material spreading out to lower longitudes. The relatively broad mass profile and the GBT data suggest that the diffuse components of the cloud may extend well beyond the VLA field of view.

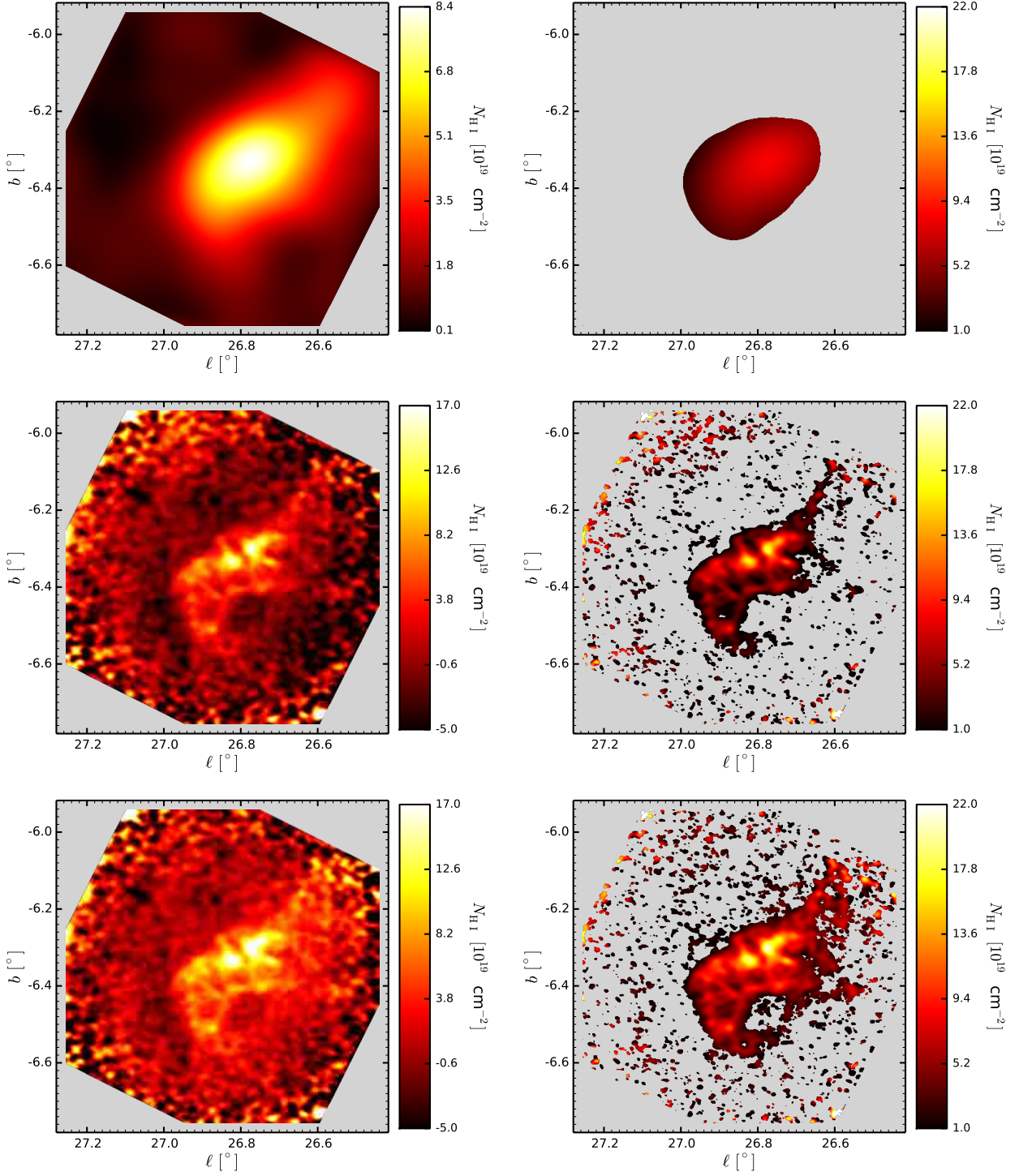


Fig. 30.— H I column density maps for G26.9 – 6.3, integrated over 51 spectral channels in the interval $108.5 \leq V_{\text{LSR}} \leq 140.7 \text{ km s}^{-1}$, as described in the caption to Fig. 9.

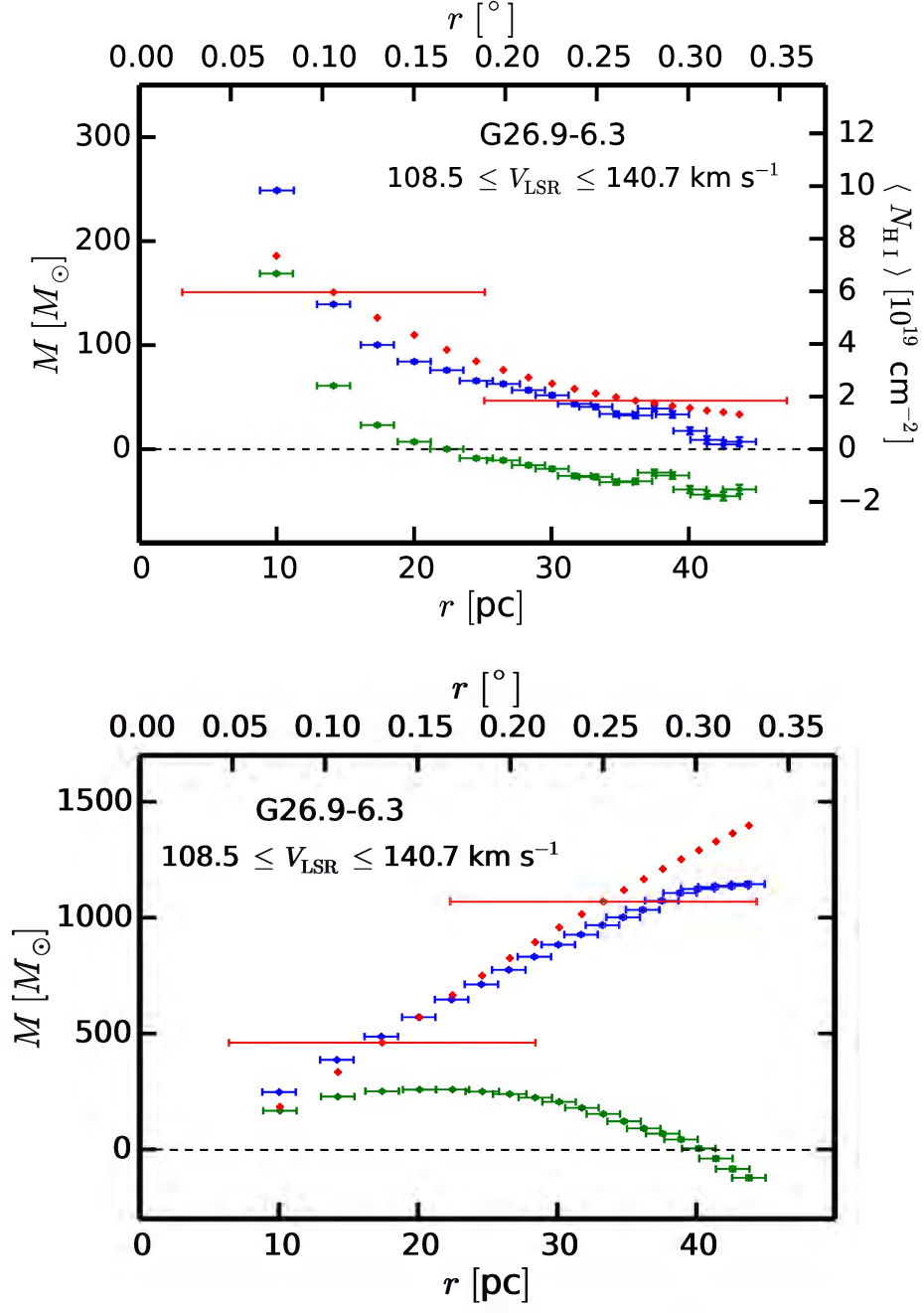


Fig. 31.— Radial mass profiles for G26.9 – 6.3 as described in the caption to Fig. 10.

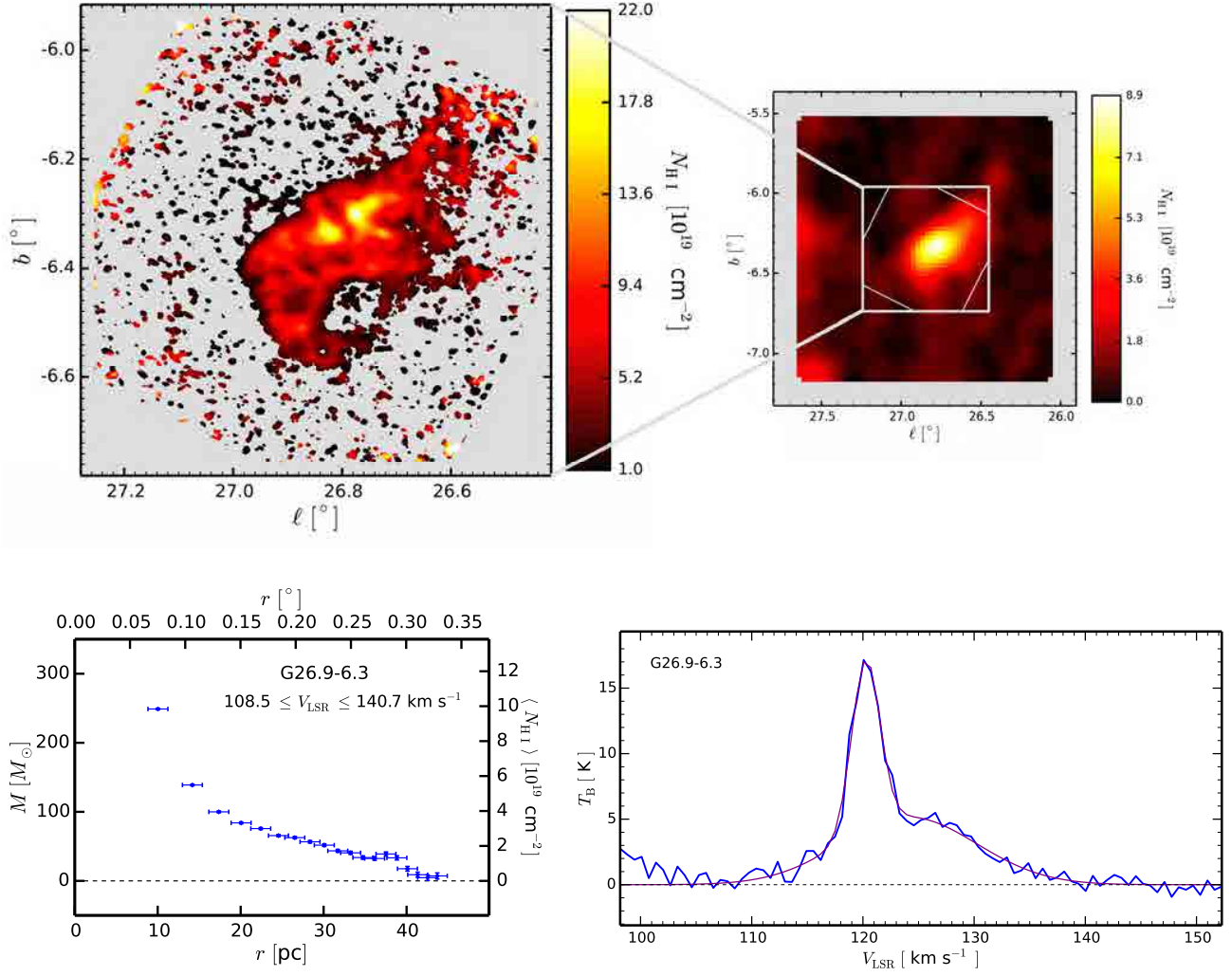


Fig. 32.— Summary of G26.9 – 6.3 as described in the caption to Fig. 11. A cloud with a sharp boundary toward high latitude and toward the plane, and diffuse material spreading out on the opposite side. More than half of the mass is within 20 pc of the brightest point, but the diffuse material is responsible for the broad mass profile. Its spectrum at peak N_{HI} shows two components with broad and narrow FWHM of 14.5 and 3.0 km s^{-1} , suggestive of a cloud with a two-phase structure. The line widths of the two components place an upper limit on their temperatures of 4600 K and 200 K.

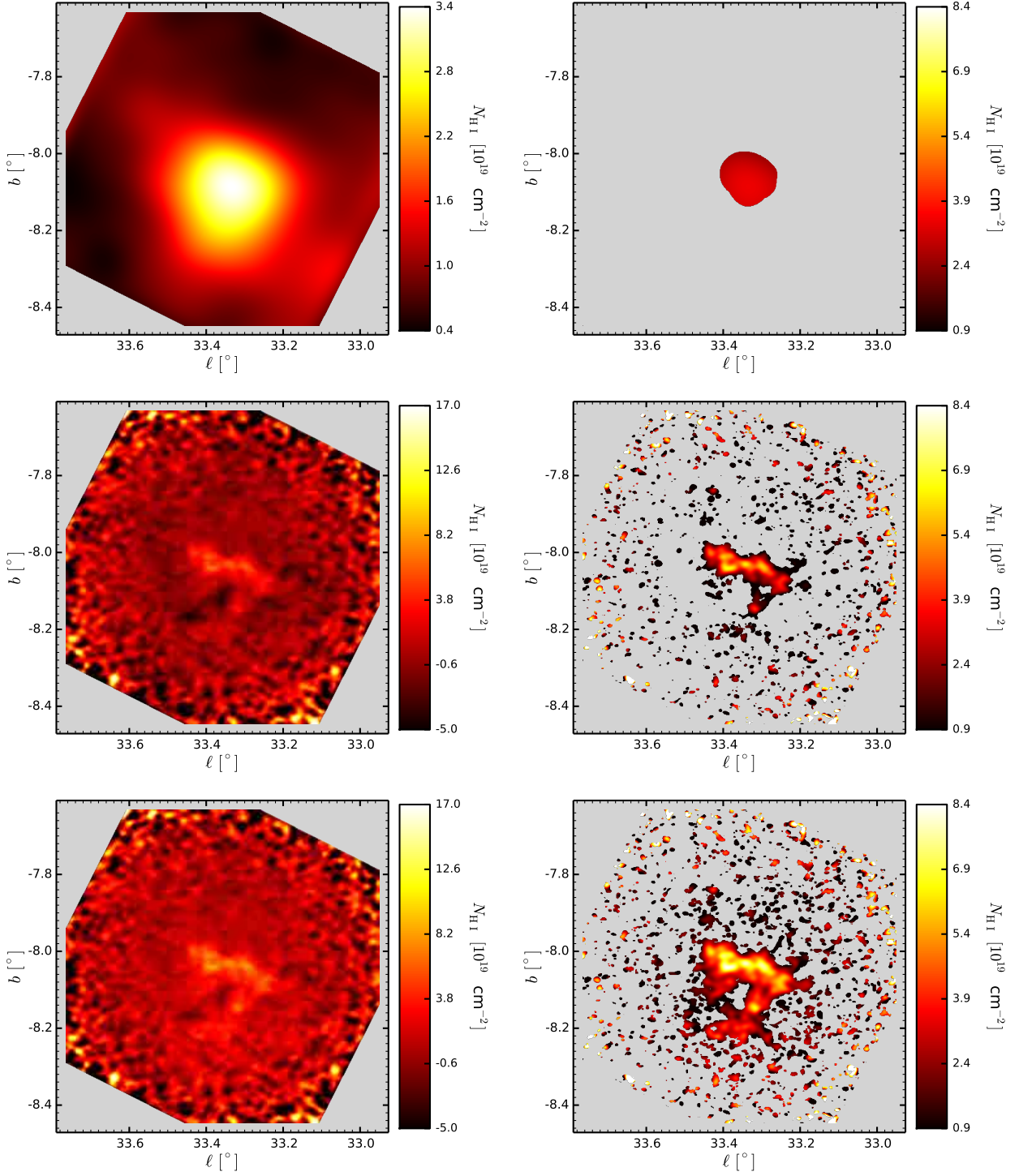


Fig. 33.— H I column density maps for G33.4 – 8.0, integrated over 37 spectral channels in the interval $92.3 \leq V_{\text{LSR}} \leq 115.5 \text{ km s}^{-1}$, as described in the caption to Fig. 9.

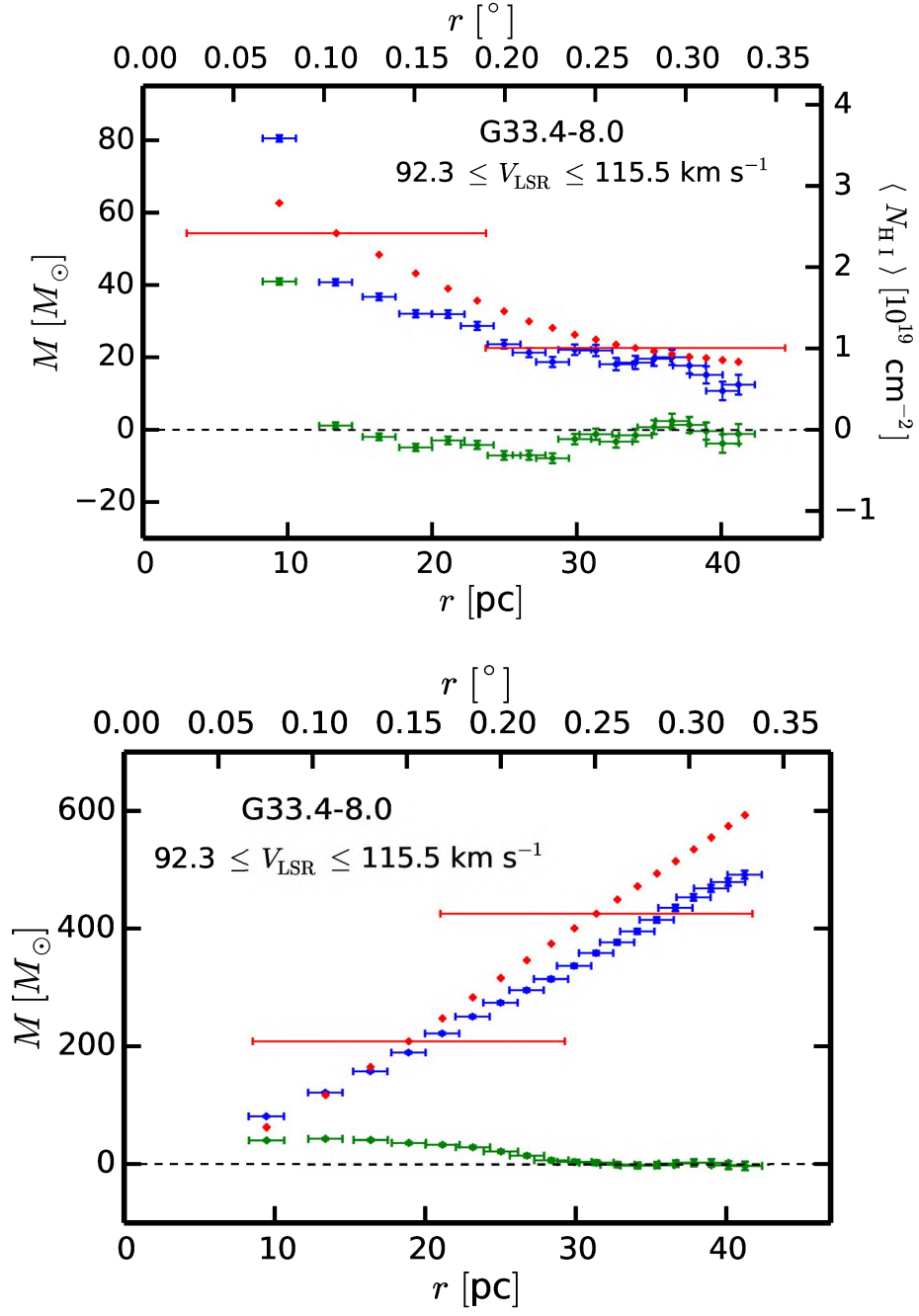


Fig. 34.— Radial mass profiles for G33.4 – 8.0 as described in the caption to Fig. 10.

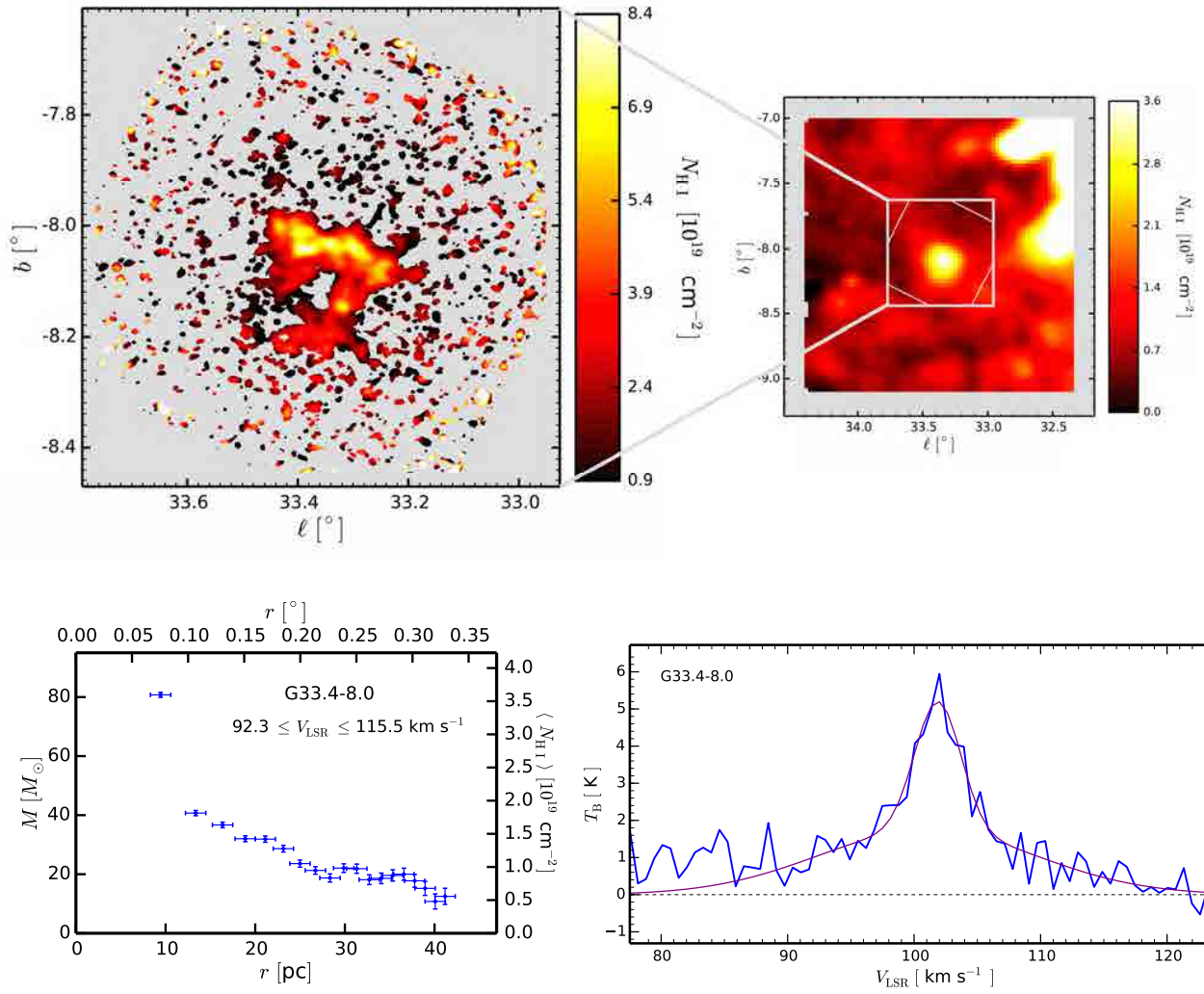


Fig. 35.— Summary of G33.4 – 8.0 as described in the caption to Fig. 11. This small isolated cloud of $\sim 160 M_{\odot}$ in its dense part is the most distant from the Galactic plane of any in the sample and has a complex structure. It has many column density maxima spread along a central ridge on the edge closest to the Galactic plane. The spectrum at the highest column density point has two components, one broad and one narrow, suggesting a two-phase thermal structure.

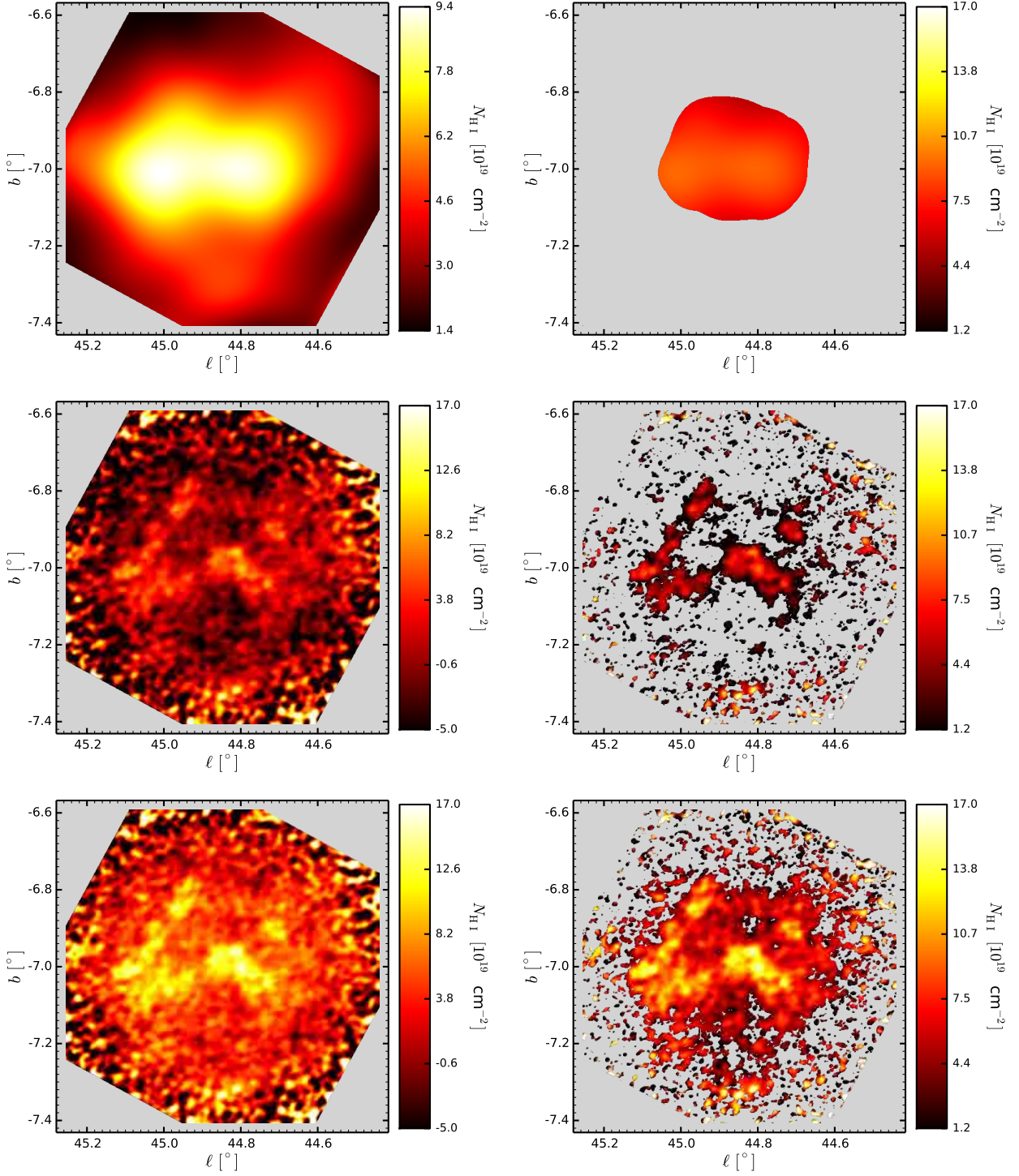


Fig. 36.— H I column density maps for G44.8 – 7.0, integrated over 73 spectral channels in the interval $79.8 \leq V_{\text{LSR}} \leq 126.2 \text{ km s}^{-1}$, as described in the caption to Fig. 9.

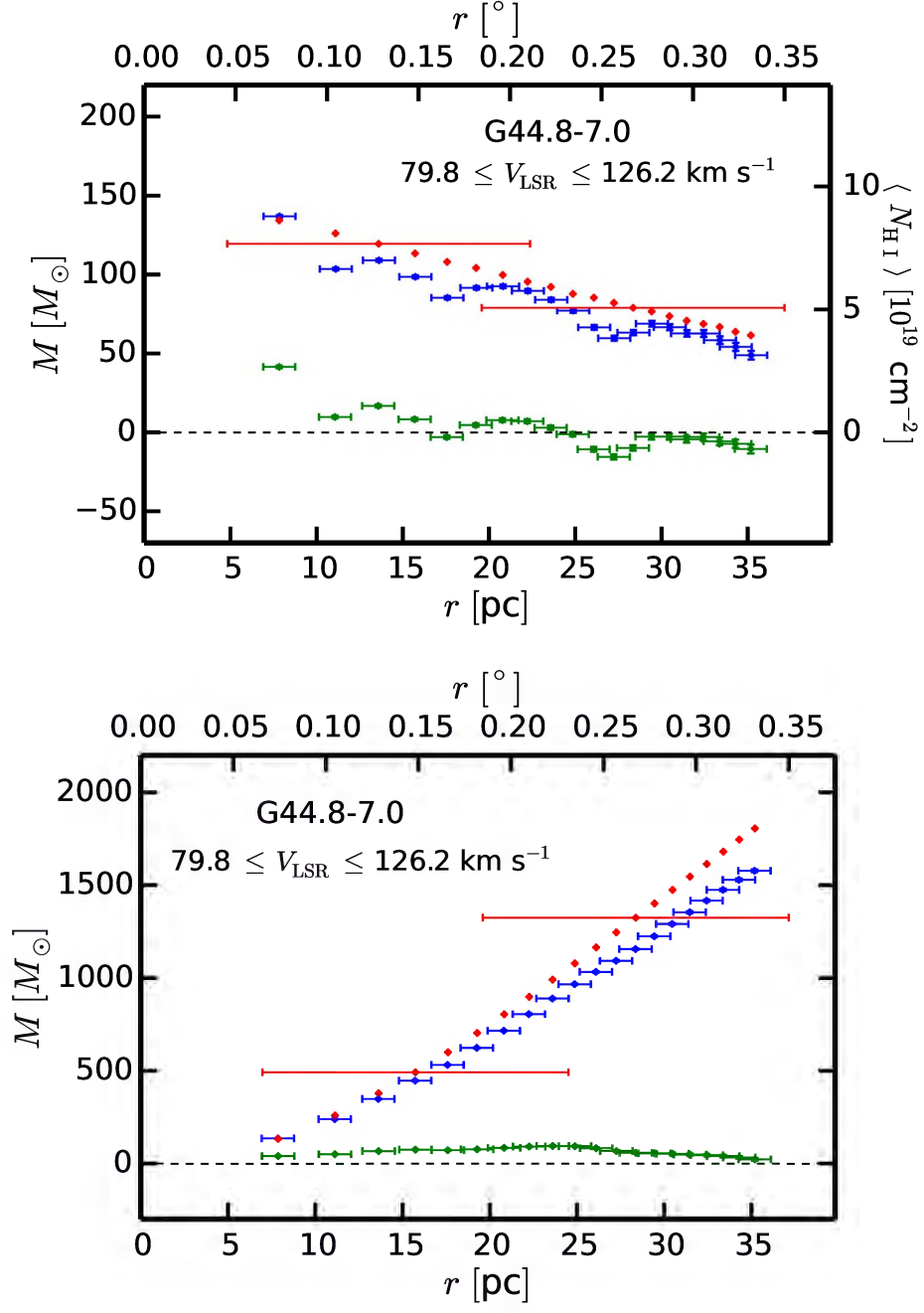


Fig. 37.— Radial mass profiles for G44.8 – 7.0 as described in the caption to Fig. 10.

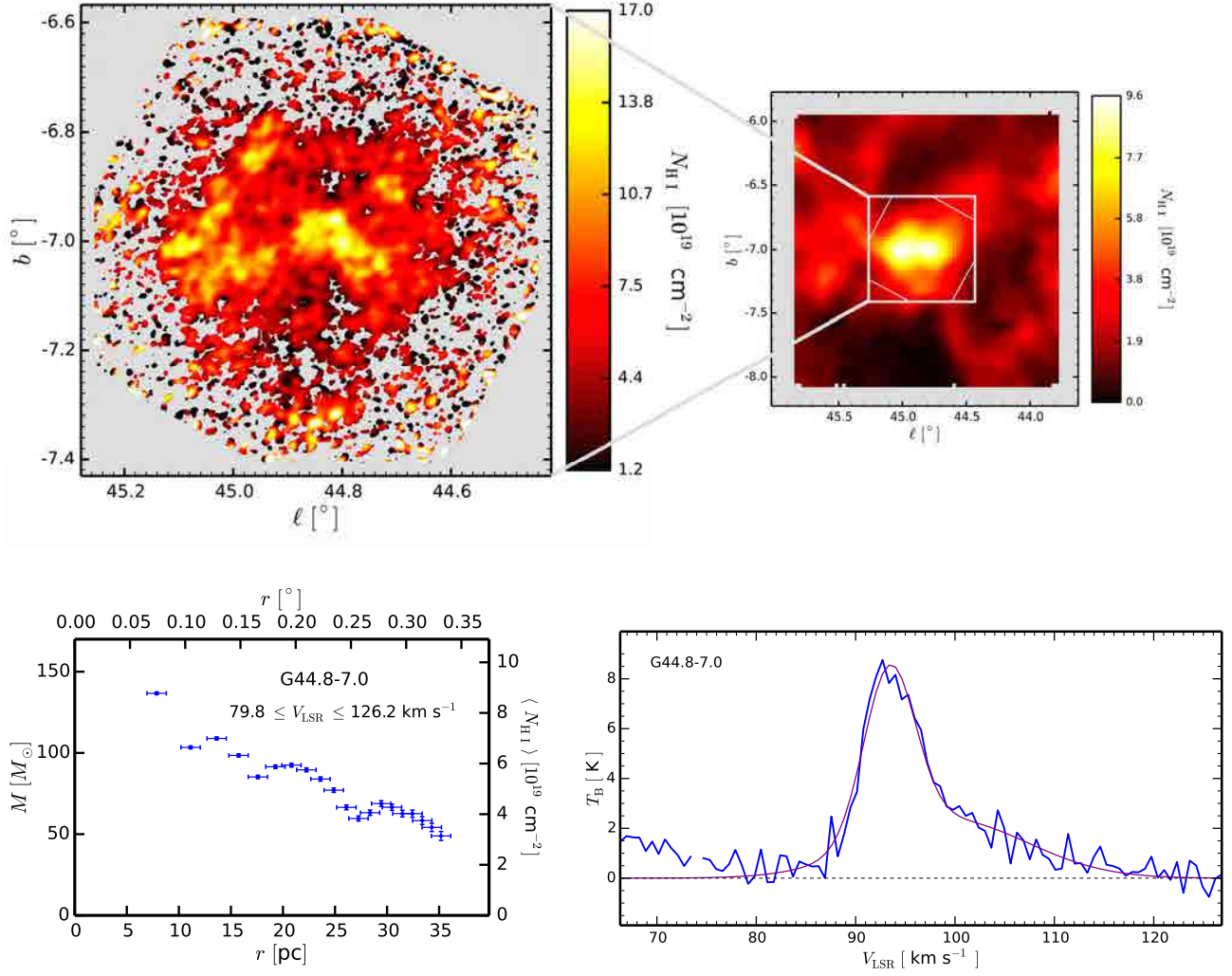


Fig. 38.— Summary of G44.8 – 7.0 as described in the caption to Fig. 11. In the spectrum a channel at 74.0 km s^{-1} is flagged due to an RFI spike. This large, massive cloud extends beyond the primary beam of the VLA. This, and the very small cloud G16.0+3.0 are the only clouds whose shape is nearly circular, though the brightest gas is concentrated in numerous small clumps. The spectrum at the N_{HI} peak is asymmetric with a broad wing to higher velocity. This cloud has among the largest excess V_{LSR} beyond the expected V_t of any in the sample.

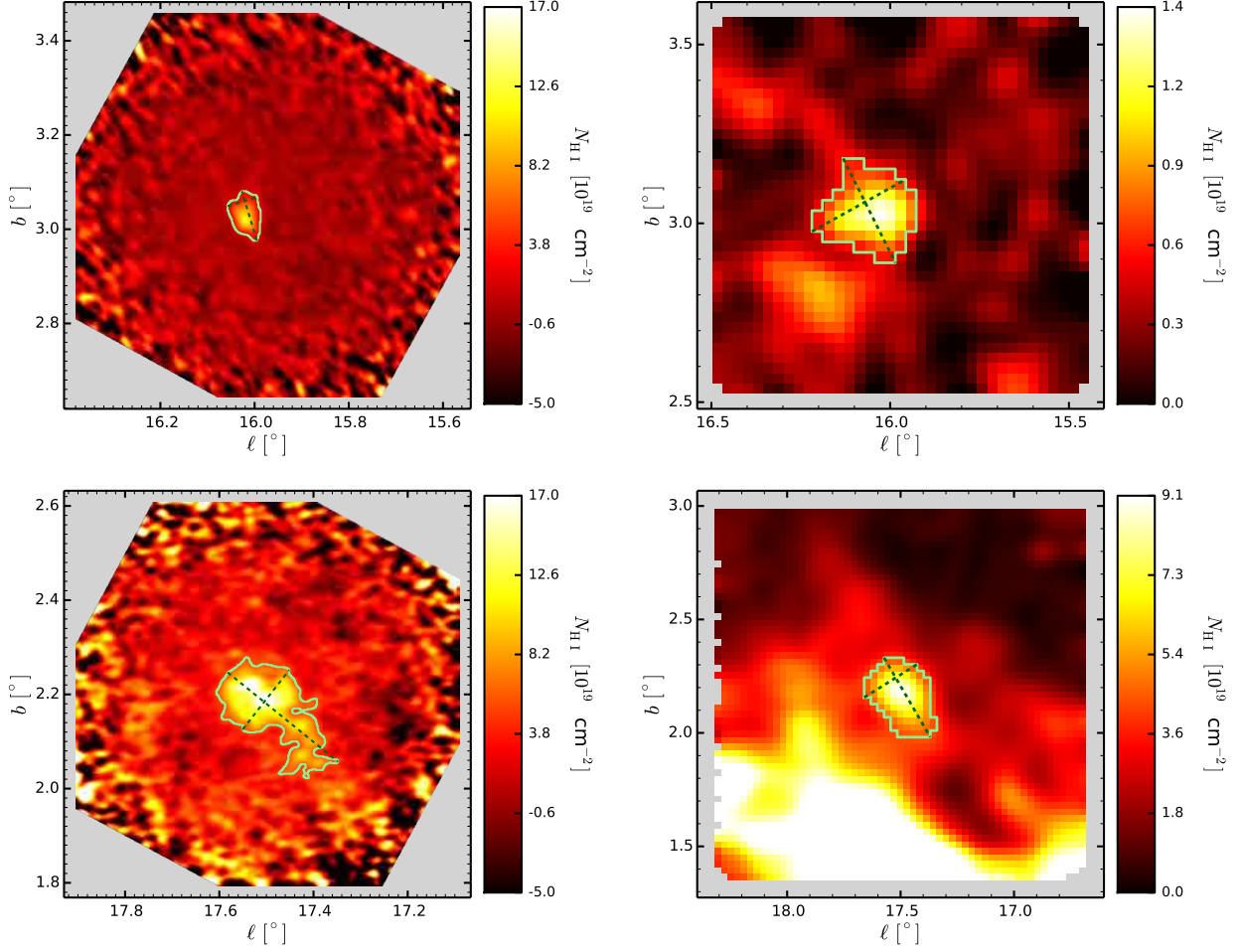


Fig. 39.— Contours for determination of size and mass of clouds based on VLA+GBT (left) and GBT only (right). Top: G16.0+3.0, contour levels $N_{\text{HI}} = 2.0 \times 10^{19} \text{ cm}^{-2}$ (VLA+GBT) and $5.5 \times 10^{18} \text{ cm}^{-2}$ (GBT); bottom: G17.5+2.2, contour levels $N_{\text{HI}} = 5.6 \times 10^{19} \text{ cm}^{-2}$ (VLA+GBT) and $4.4 \times 10^{19} \text{ cm}^{-2}$ (GBT). The dashed lines designate the axes: major (the longest distance between two contour points) and minor (the longest distance between contour points in the direction, perpendicular to the minor axis).

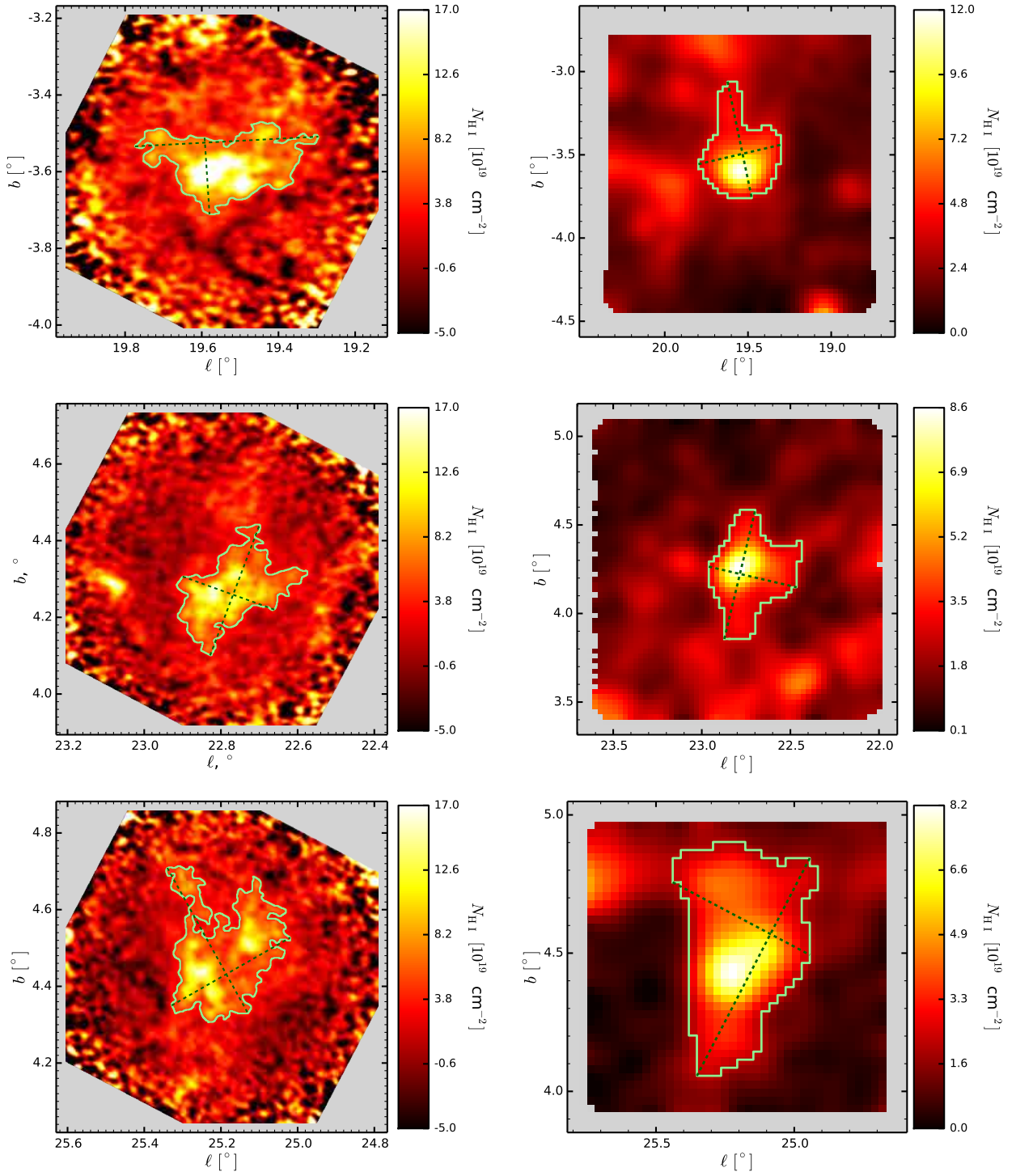


Fig. 40.— Contours for determination of size and mass of clouds based on VLA+GBT (left) and GBT only (right). Top: G19.5 – 3.6, contour levels $N_{\text{HI}} = 5.5 \times 10^{19} \text{ cm}^{-2}$ (VLA+GBT) and $3.9 \times 10^{19} \text{ cm}^{-2}$ (GBT); middle: G22.8 + 4.3, contour levels $N_{\text{HI}} = 4.1 \times 10^{19} \text{ cm}^{-2}$ (VLA+GBT) and $2.6 \times 10^{19} \text{ cm}^{-2}$ (GBT); bottom: G25.2 + 4.5, contour levels $N_{\text{HI}} = 4.3 \times 10^{19} \text{ cm}^{-2}$ (VLA+GBT) and $2.2 \times 10^{19} \text{ cm}^{-2}$ (GBT).

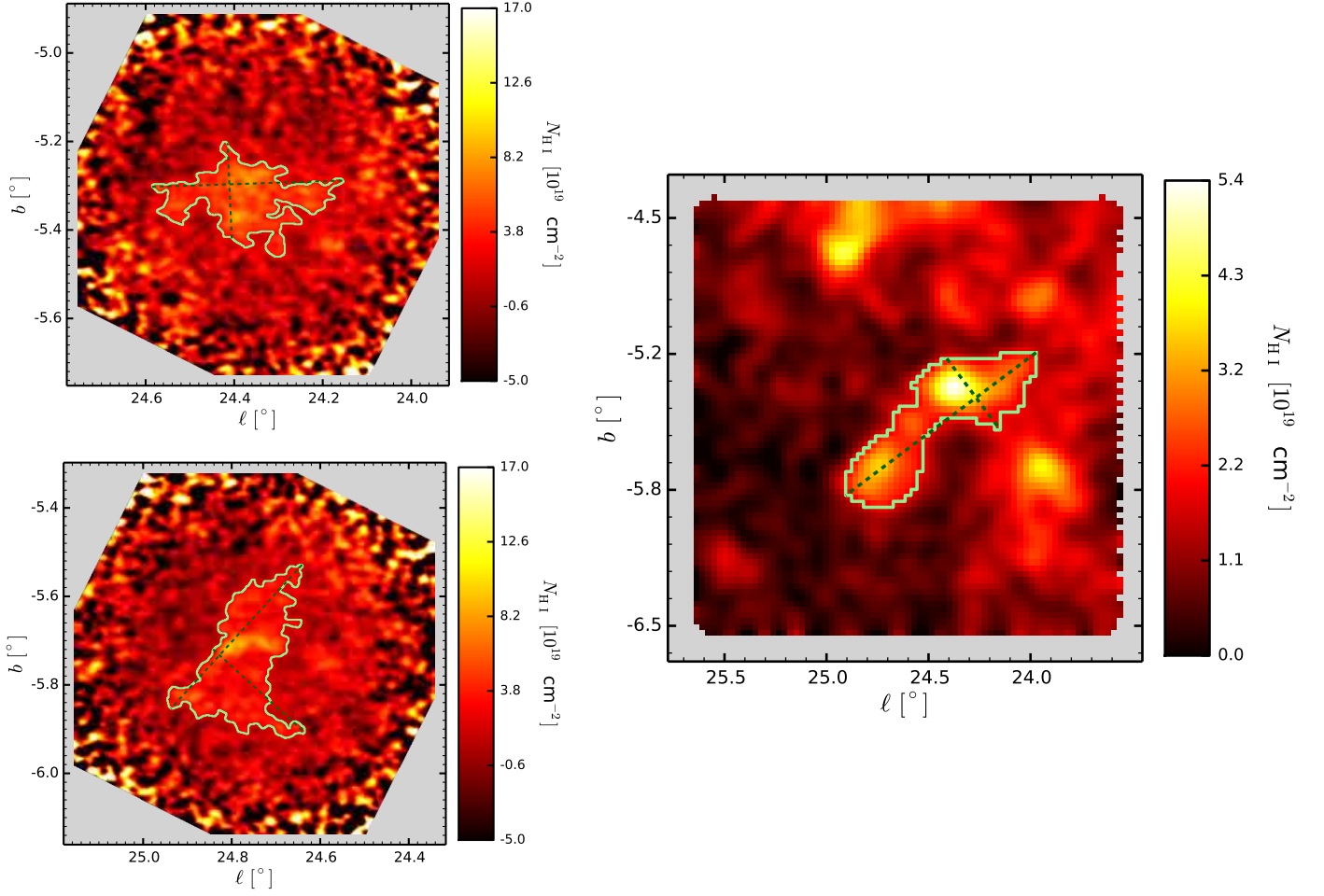


Fig. 41.— Contours for determination of size and mass of clouds based on VLA+GBT (left) and GBT only (right). Top left: G24.3–5.3 (VLA+GBT), contour at $N_{\text{HI}} = 3.1 \times 10^{19} \text{ cm}^{-2}$; bottom left: G24.7–5.7 (VLA+GBT), contour at $N_{\text{HI}} = 2.3 \times 10^{19} \text{ cm}^{-2}$; right: Group of G24.3–5.3 and G24.7–5.7 (GBT), contour at $N_{\text{HI}} = 1.9 \times 10^{19} \text{ cm}^{-2}$.

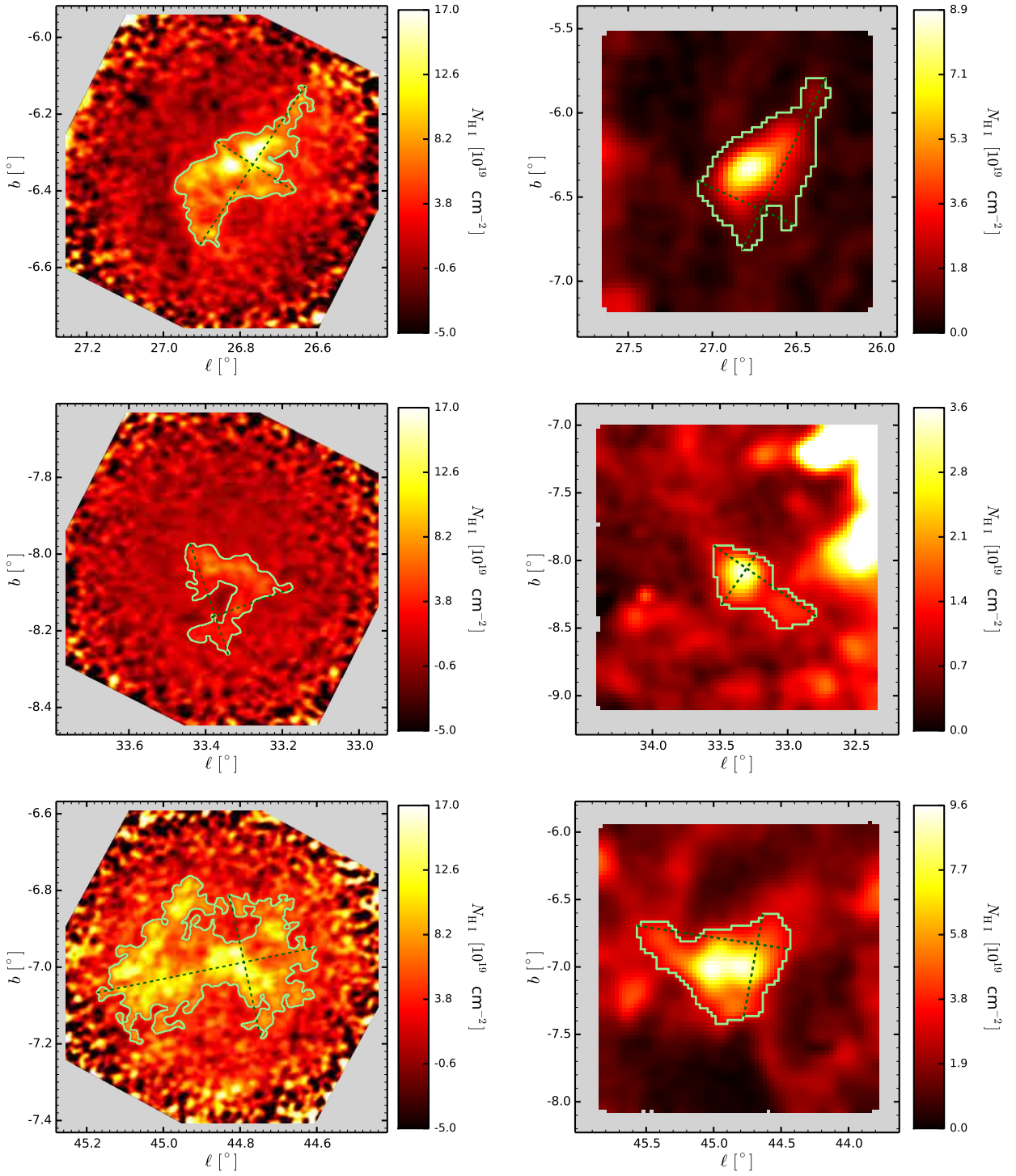


Fig. 42.— Contours for determination of size and mass of a cloud based on VLA+GBT (left) and GBT only (right): Top: G26.9 – 6.3, contours at $N_{\text{HI}} = 5.3 \times 10^{19} \text{ cm}^{-2}$ (VLA+GBT) and $1.1 \times 10^{19} \text{ cm}^{-2}$ (GBT); middle: G33.4 – 8.0, contours at $N_{\text{HI}} = 2.5 \times 10^{19} \text{ cm}^{-2}$ (VLA+GBT) and $1.2 \times 10^{19} \text{ cm}^{-2}$ (GBT); bottom: G44.8 – 7.0, contours at $N_{\text{HI}} = 5.5 \times 10^{19} \text{ cm}^{-2}$ (VLA+GBT) and $3.1 \times 10^{19} \text{ cm}^{-2}$ (GBT).

REFERENCES

- Bland-Hawthorn, J., & Cohen, M. 2003, *ApJ*, 582, 246
- Boothroyd, A. I., Blagrove, K., Lockman, F. J., et al. 2011, *A&A*, 536, A81
- Burton, W. B., & Liszt, H. S. 1993, *A&A*, 274, 765
- Carretti, E., Crocker, R. M., Staveley-Smith, L., et al. 2013, *Nature*, 493, 66
- Clark, B. G. 1965, *ApJ*, 142, 1398
- Clemens, D. P. 1985, *ApJ*, 295, 422
- Dedes, L., & Kalberla, P. W. M. 2010, *A&A*, 509, 60
- Dehnen, W., & Binney, J. 1998, *MNRAS*, 294, 429
- Dickey, J. M. 2013, in *Planets, Stars and Stellar Systems*, vol 5, eds. T.D. Oswalt and G. Gilmore (Dordrecht: Springer Science+Business Media), 549
- Dickey, J. M., & Lockman, F. J. 1990, *ARA&A*, 28, 215
- Dickey, J.M., McClure-Griffiths, N., Gibson, S.J., et al. 2013, *PASA* 30, 3
- Field, G. B., Goldsmith, D. W., & Habing, H. J. 1969, *ApJ*, 155, L149
- Ford, H. A., McClure-Griffiths, N. M., Lockman, F. J., et al. 2008, *ApJ*, 688, 290
- Ford, H. A., Lockman, F. J., & McClure-Griffiths, N. M. 2010, *ApJ*, 722, 367
- Gatto, A., Walch, S., Mac Low, M.-M., et al. 2015, *MNRAS*, 449, 1057
- Heiles, C., & Troland, T. H. 2003, *ApJ*, 586, 1067
- Heiles, C., & Troland, T. H. 2005, *ApJ*, 624, 773

- Hobbs, L. M. 1978, ApJ, 222, 491
- Jenkins, E. B. 2012, in EAS Pub. Ser. 56, The Role of the Disc-Halo Interaction in Galaxy Evolution: Outflows vs. Infall?, ed. M.A. de Avillez (Les Ulis: EDP Sciences), 31
- Jenkins, E. B., & Tripp, T. M. 2011, ApJ, 734, 65
- Kalberla, P. M. W. & Kerp, J. 2009, ARA&A, 47, 27
- Kerr, F. J., & Lynden-Bell, D. 1986, MNRAS, 221, 1023
- Koyama, H., & Ostriker, E. C. 2009, ApJ, 693, 1346
- Kulkarni, S. R., & Heiles, C. 1987, in Interstellar Processes, ed. D. Hollenbach, & H. Thronson (Dordrecht: Reidel), 87
- Lallement, R., Welsh, B. Y., Vergely, J. L., Crifo, F., & Sfeir, D. 2003, A&A, 411, 447
- Lazarian, A., & Pogosyan, D. 2000, ApJ, 537, 720
- Lockman, F. J. 1984, ApJ, 283, 90
- Lockman, F. J. 2002, ApJ, 580, L47
- Lockman, F. J. 2004, in IAU Symp. 217, Recycling Intergalactic and Interstellar Matter, ed. P.-A. Duc, J. Braine, & E. Brinks (San Francisco: ASP), 130
- Lockman, F.J., & Pidopryhora, Y. 2005, in ASP Conf. Ser. 331, Extra-planar Gas, ed. R. Braun (San Francisco: ASP), 59
- McClure-Griffiths, N. M., & Dickey, J. M. 2007, ApJ, 671, 427
- McClure-Griffiths, N. M., Green, J. A., Hill, A. S., et al. 2013, ApJ, 770, LL4
- McKee, C. F., & Ostriker, J. P. 1977, ApJ, 218, 148

- Miville-Deschênes, M.-A., Joncas, G., Falgarone, E., & Boulanger, F. 2003, *A&A*, 411, 109
- Munch, G. 1952, *PASP*, 64, 312
- Perley, R. 21 November 2000 Report in AIPS help file for PBCOR, NRAO, www.aips.nrao.edu/cgi-bin/ZXHLP2.PL?PBCOR
- Pidopryhora, Y., Liszt, H., Lockman, F.J., & Rupen, M.P. 2004, *BAAS*, 36, 1583
- Pidopryhora, Y. 2006, PhD Thesis, Ohio University, http://rave.ohiolink.edu/etdc/view?acc_num=ohiou1162881965
- Pidopryhora, Y., Lockman, F.J., & Rupen, M.P. 2012, in *EAS Pub. Ser. 56, The Role of the Disc-Halo Interaction in Galaxy Evolution: Outflows vs. Infall?*, ed. M.A. de Avillez (Les Ulis: EDP Sciences), 171
- Prata, S. W. 1964, *BAN*, 17, 511
- Rathborne, J. M., Jackson, J. M., Chambers, E. T., et al. 2010, *ApJ*, 715, 310
- Redfield, S., & Linsky, J. L. 2008, *ApJ*, 673, 283
- Sault, R. J., & Killeen, N. 26 May 2011, *Miriad Users Guide*, Australia Telescope National Facility, ftp://ftp.atnf.csiro.au/pub/software/miriad/userguide_US.ps.bz2
- Sault, R. J., Teuben, P. J., & Wright, M. C. H., 1995, in *ASP Conf. Ser. 77, Astronomical Data Analysis Software and Systems IV*, ed. R. Shaw, H. E. Payne, & J. J. E. Hayes (San Francisco, CA: ASP), 433
- Saury, E., Miville-Deschênes, M.-A., Hennebelle, P., Audit, E., & Schmidt, W. 2014, *A&A*, 567, A16
- Shane, W. W. 1967, in *IAU Symp. 31, Radio Astronomy and the Galactic System*, ed. H. van Woerden (London: Academic), 177

- Simonson, S. C. 1971, *A&A*, 12, 136
- Stanimirović, S., Staveley-Smith, L., Dickey, J.M., Sault, R.J., & Snowden, S.L. 1999, *MNRAS*, 302, 417
- Stanimirović, S. 1999, PhD Thesis, University of Western Sydney Nepean
- Stanimirović, S., Putman, M., Heiles, C., et al. 2006, *ApJ*, 653, 1210
- Stil, J. M., Lockman, F. J., Taylor, A. R., et al. 2006, *ApJ*, 637, 366
- Strasser, S. T., Dickey, J. M., Taylor, A. R., et al. 2007, *AJ*, 134, 2252
- Su, M., Slatyer, T. R., & Finkbeiner, D. P. 2010, *ApJ*, 724, 1044
- Vázquez-Semadeni, E. 2012, in *EAS Pub. Ser.* 56, *The Role of the Disc-Halo Interaction in Galaxy Evolution: Outflows vs. Infall?*, ed. M.A. de Avillez (Les Ulis: EDP Sciences), 39
- Welsh, B. Y., Lallement, R., Vergely, J.-L., & Raimond, S. 2010, *A&A*, 510, AA54
- Wolfire, M. G., Hollenbach, D., McKee, C. F., Tielens, A. G. G. M., & Bakes, E. L. O. 1995, *ApJ*, 443, 152
- Wolfire, M. G., McKee, C. F., Hollenbach, D., & Tielens, A. G. G. M. 1995, *ApJ*, 453, 673